



INSTITUT NATIONAL DES SCIENCES APPLIQUÉES

---

# ADVANCED SEMICONDUCTOR LASERS

Frédéric Grillot

---



UNIVERSITÉ  
EUROPÉENNE  
DE BRETAGNE

Université Européenne de Bretagne  
Laboratoire CNRS FOTON  
20 avenue des buttes de Coesmes  
35043 Rennes Cedex  
[frederic.grillot@insa-rennes.fr](mailto:frederic.grillot@insa-rennes.fr)

Second Version - Year 2010



# Contents

<b>1</b>	<b>Basics of Semiconductor Lasers</b>	<b>7</b>
1.1	Principle of Operation . . . . .	7
1.1.1	Radiative Transitions in a Semiconductor . . . . .	7
1.1.2	Optical Gain and Laser Cavity . . . . .	9
1.1.3	Output Light-Current Characteristic . . . . .	11
1.1.4	Carrier Confinement . . . . .	13
1.1.5	Optical Field Confinement and Spatial Modes . . . . .	15
1.1.6	Near- and Far-Field Patterns . . . . .	17
1.2	Quantum Well Lasers . . . . .	18
1.3	Quantum Dot Lasers . . . . .	20
1.4	Single-Frequency Lasers . . . . .	23
1.4.1	Short-Cavity Lasers . . . . .	23
1.4.2	Coupled-Cavity Lasers . . . . .	23
1.4.3	Injection-Locked Lasers . . . . .	24
1.4.4	DBR Lasers . . . . .	25
1.4.5	DFB Lasers . . . . .	26
<b>2</b>	<b>Advances in Measurements of Physical Parameters of Semiconductor Lasers</b>	<b>31</b>
2.1	Measurements of the Optical Gain . . . . .	31
2.1.1	Determination of the Optical Gain from the Amplified Spontaneous Emission . . . . .	32
2.1.2	Determination of the Optical Gain from the True Spontaneous Emission	34
2.2	Measurement of the Optical Loss . . . . .	36
2.3	Measurement of the Carrier Leakage in Semiconductor Lasers . . . . .	37
2.3.1	Optical Technique of Studying the Carrier Leakage . . . . .	37
2.3.2	Electrical Technique of Studying Carrier Leakage . . . . .	38
2.4	Electrical and Optical Measurements of RF Modulation Response below Threshold . . . . .	40
2.4.1	Determination of the Carrier Lifetime from the Device Impedance . . . . .	41

2.4.2	Determination of the Carrier Lifetime from the Optical Response Measurements . . . . .	43
2.5	Optical Measurements of RF Modulation Response and RIN above threshold . . . . .	44
2.5.1	Determination of the Resonant Frequency and Differential Gain from the RIN Measurements . . . . .	47
2.6	Measurements of the linewidth enhancement factor . . . . .	49
2.6.1	Definition . . . . .	50
2.6.2	Measurement Techniques of the $\alpha$ -factor . . . . .	52
2.6.3	Measurements of linewidth enhancement factor from ASE and TSE spectra . . . . .	59
2.7	Measurements of the Carrier Temperature and Carrier Heating in Semiconductor Lasers . . . . .	61
<b>3</b>	<b>Ultrafast Diode Lasers in Fiber Optics Communications</b>	<b>65</b>
3.1	High-Speed Modulation of Laser Diodes . . . . .	65
3.1.1	Small-Signal Modulation Response . . . . .	66
3.2	Nonlinear Gain Effects . . . . .	69
3.2.1	Origin and Definition . . . . .	69
3.2.2	Evaluation of the Gain Compression in Quantum Dot/Dash Devices . . . . .	71
3.2.3	Consequences on the Linewidth Enhancement Factor . . . . .	73
3.3	Quantum-Well Lasers and Carrier-Transport Effects . . . . .	77
3.4	Large-Signal Effects . . . . .	81
3.5	Spectral Broadening and Spectral Control Under High-Speed Modulation . . . . .	83
3.5.1	Frequency Chirping . . . . .	83
3.5.2	Low-Chirp Lasers . . . . .	83
3.6	Fundamental Limitations . . . . .	84
3.6.1	Power Limitation . . . . .	85
3.6.2	Dispersion Limitation . . . . .	86
3.6.3	Timing Jitter Limitation . . . . .	86
<b>4</b>	<b>Gain and Q-Switching in Semiconductor Lasers</b>	<b>89</b>
4.1	Gain Switching . . . . .	89
4.1.1	Principle of Operation . . . . .	89
4.1.2	Pulsewidth and Peak Power . . . . .	91
4.1.3	Optical Spectra and Frequency Chirping . . . . .	93
4.2	Q-Switching in Laser Diodes . . . . .	96
4.2.1	Active Q-Switching . . . . .	96
4.2.2	Passive Q-Switching . . . . .	98

---

4.2.3	Optical Spectra . . . . .	99
<b>5</b>	<b>Mode-Locked Semiconductor Lasers</b>	<b>101</b>
5.1	Principle of Operation . . . . .	102
5.2	Active Mode-Locking . . . . .	102
5.3	Passive-Mode Locking . . . . .	104
5.4	Colliding Pulse Mode-Locking . . . . .	109
5.5	Monolithic Quantum Dot Passively Mode-Locked Lasers . . . . .	111
5.6	Colliding Pulse Technique for Higher Order Harmonic Generation . . . . .	114
<b>6</b>	<b>Injection-Locking of Semiconductor Diode Lasers</b>	<b>117</b>
6.1	Introduction . . . . .	117
6.2	Applications of Optically-Injected Lasers . . . . .	119
6.3	Theoretical Description . . . . .	124
6.3.1	Rate Equations . . . . .	125
6.3.2	Steady-State Solutions . . . . .	126
6.3.3	Small-Signal Analysis . . . . .	126
6.3.4	Modulation Response Model . . . . .	127
6.3.5	Identifying the Known Free-Running Operating Parameters . . . . .	129
6.4	Experimental Data and Curve-Fitting Results . . . . .	130
6.4.1	Experimental Setup and Data . . . . .	130
6.4.2	Model Based Analysis . . . . .	131



# Chapter 1

## Basics of Semiconductor Lasers

There exist a number of books devoted to semiconductor lasers in which the reader will find the story of the invention of diode lasers in the early 1960s reporting all the details on stimulated emission, gain, and absorption in semiconductors, waveguide properties, various semiconductor materials for lasers, a description of different laser structures and so on. In this chapter, we shall try to give a brief description of the principle of operation of laser diodes and some physical phenomena that are common to all types of semiconductor lasers. Finally, this chapter is shall pay special attention to some of the present-day laser devices that are most often used for ultra-short optical pulse generation and numerous applications.

### 1.1 Principle of Operation

#### 1.1.1 Radiative Transitions in a Semiconductor

The quantum electronics concepts common to all lasers are combined in the semiconductor laser with the basic pn junction that is typical of many semiconductor devices. Semiconductor laser action relies upon the interband recombination of charge carriers (electrons and holes) and the subsequent liberation of photons. Applying a forward bias on a pn junction by using an external voltage makes possible a diffusion and drift of electrons and holes across the junction. In a narrow depletion region, electron-holes pairs can recombine either radiatively or nonradiatively. Electrons and holes can also absorb the radiation. When the current through the junction exceeds a critical value, a population inversion is achieved and the rate of photon emission due to electron-hole recombination exceeds the rate of absorption due to electron-hole generation.

The electronic radiative transitions that take place between the conduction and valence bands

in a semiconductor laser play roles very similar to those that take place between pairs of states in a simple two-level laser system. However there are several obvious features of a semiconductor active medium. First, for semiconductors the optical transitions are between a continuous band of states within the valence and conduction bands. Then, the interaction between the different excited states in the band of a semiconductor is considerably greater than the interaction between the excited states of different atoms in the two-level system. Thus, collision processes in the electron and hole subsystems occur much faster and that the intraband relaxation times can be much shorter compared to those of the radiation (interband) processes. Intraband processes play crucial roles in line broadening in laser diodes. Another difference is that the higher concentration of electronic states in the bands provides the potential for a higher optical gain. Finally, in the semiconductor the excited electron-hole pairs can be transported through the material by conduction or diffusion leading to a spatial variation of the optical mode through the stimulated emission.

The band structure of a typical III-V semiconductor and radiative transitions are shown in figure 1.1. For laser diodes, the transition from the conduction band to the valence one should

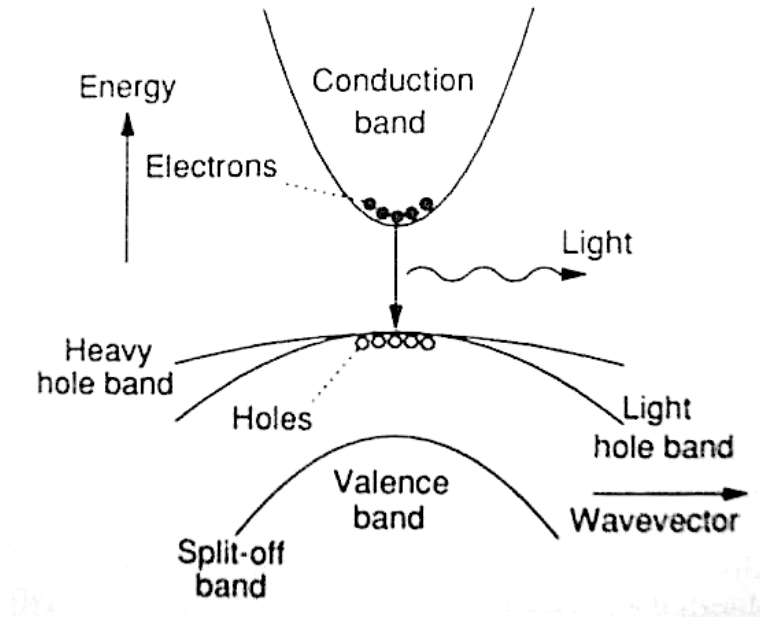


Figure 1.1: A realistic band model for a III-V direct gap semiconductor

be radiative and yield a photon with energy:

$$\hbar\omega = E_2 - E_1 \quad (1.1)$$

where  $\hbar$  is the Planck's constant and  $E_1$ ,  $E_2$  are the electron energy in the valence and conductive bands. As stated by the rules of the quantum mechanics, it can be shown that each process must conserve both the energy and wavevector  $k$ . Due to the fact that the photon

wave number is at least two orders of magnitude lower (for visible and near infrared radiations) compared to the electron and hole wavevectors, the radiation transition is described in figure 1.1 as a vertical line. The  $k$ -conservation rule immediately implies a requirement for direct band-gap semiconductors if we want the radiative recombination to be significant. It can be shown using the Fermi-Dirac statistics of electrons and holes in a semiconductor that for net stimulated emission or optical gain, the separation of quasi-Fermi levels for electrons  $F_c$  and holes  $F_v$  must be:

$$F_c - F_v > \hbar\omega \quad (1.2)$$

Inequality (1.2) was introduced by Bernard and Durrafourg, French researchers from the Centre National des Télécommunications (CNET). This condition is necessary, but not sufficient for laser action in a semiconductor. In order to achieve lasing, the stimulated emission rate must be sufficient to overcome various loss mechanisms. The optical gain is related directly to the rate of stimulated emission. The main factors influencing the gain spectrum are the density of states functions and the transition and occupation probabilities.

### 1.1.2 Optical Gain and Laser Cavity

A simple empirical formula for the optical gain  $g$  is obtained by assuming a linear dependence on carrier concentration  $N$  and a parabolic variation with wavelength  $\lambda$  such as:

$$g = g_0(N - N_t) + b(\lambda - \lambda_p)^2 \quad (1.3)$$

where  $g_0$  is the differential gain coefficient,  $N_t$  is the transparency density for which  $g = 0$  at  $\lambda = \lambda_p$  and  $N = N_t$ ,  $b$  is related to the gain spectral width, and  $\lambda_p$  is the wavelength corresponding to the gain peak. As the carrier concentration is supposed to increase due to the current injection, the photon energy at the gain peak shifts to higher values:

$$\lambda_p = \lambda_0 + (N - N_t) \frac{d\lambda}{dN} \quad (1.4)$$

The values for the above parameters can be obtained from measurements of gain spectra. For instance, for InGaAsP lasers, we will find  $\lambda_0=1550$  nm,  $g_0=2.7 \cdot 10^{-16}$  cm<sup>2</sup>,  $b=0.15$  cm<sup>-1</sup>nm<sup>-2</sup>,  $N_t=1.2 \cdot 10^{18}$ cm<sup>-3</sup> and  $\frac{d\lambda}{dN}=-2.7 \cdot 10^{-17}$  nm cm<sup>3</sup>.

The optical gain alone is not enough to operate a laser. Optical feedback is the other necessary ingredient. In laser diodes, optical feedback is provided in different ways. The simplest way is to form a laser cavity by two cleaved facets of the diode, which actually are partially reflecting mirrors. Figure 1.2 illustrates a semiconductor laser that has two cleaved facets for optical feedback. The laser cavity provides a direction selectivity for the process of stimulated emission because only photons traveling along its axis are reflected back and forth and experience maximum gain. It also provides a frequency selectivity since the feedback is

strongest for frequencies corresponding to the modes of the Fabry-Perot cavity. Although spontaneous and stimulated emission can occur while a current is applied to the junction, the laser does not generate coherent emission until the current exceeds a critical value, which is known as the threshold current. In order to obtain the threshold conditions, it is required that the optical field in the cavity reproduce itself after each round trip (steady-state or continuous-wave conditions). For the Fabry-Perot laser shown in figure 1.2, the threshold conditions can be written as:

$$\Gamma g_{th} = \alpha_i + \frac{1}{2L} \ln \left( \frac{1}{R_1 R_2} \right) \quad (1.5)$$

$$\beta L = m\pi \quad (1.6)$$

where  $m$  is an integer,  $g_{th}$  is the threshold gain,  $\alpha_i$  is the internal loss in the active layer

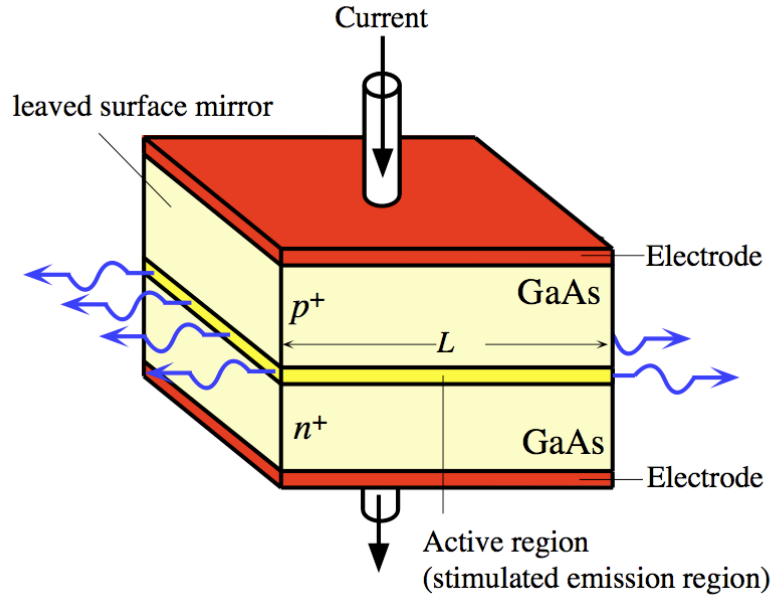


Figure 1.2: Schematic illustration of a Fabry-Perot diode laser. The light is emitted from two partially reflecting cleaved facets of the diode

due to free-carrier absorption and scattering,  $L$  is the cavity length,  $R_1$  and  $R_2$  are the facet reflectivities and  $\beta$  is the propagation constant. The factor  $\Gamma$  is the optical confinement which represents the fraction of the mode energy contained in the active layer. Thus, it accounts for the reduction in gain due to the spreading of the optical mode to the cladding layers surrounding the active layer.

**Note:** Internal loss  $\alpha_i$  can be written as a superposition of terms  $\alpha_i = \Gamma\alpha_a + (1 - \Gamma)\alpha_c + \alpha_s$ .

Coefficient  $\alpha_c$  accounts for loss in the confinement area and equals about  $5 \text{ cm}^{-1}$ . The term  $\alpha_s \approx 15 \text{ cm}^{-1}$  takes into account the scattering loss. Basically it is related to the quality of the growth operation and especially the regrowth which is required for the realization of buried ridge strip (BRS) structure. Coefficient  $\alpha_a$  accounts for the loss in the active zone and depends on the transitions between valence bands. As a consequence, this coefficient is wavelength-dependent and equals  $90 \text{ cm}^{-1}$  at  $1.55 \mu\text{m}$  and  $60 \text{ cm}^{-1}$  at  $1.31 \mu\text{m}$ . At the wavelength of  $1.55 \mu\text{m}$ , it can be shown that  $\alpha_a = KN + \alpha_{a0}$  with  $N$  the injected carrier density,  $\alpha_{a0} \approx 45 \text{ cm}^{-1}$  and  $K = 3.75 \cdot 10^{-17} \text{ cm}^2$  (values from experiments).

Equation (1.6) serves to extract the lasing frequency  $\omega_0$  which is one of the cavity mode  $\omega_m$ :

$$\omega_m = \frac{m\pi c}{nL} \quad (1.7)$$

and which is the nearest to the gain peak as shown in figure 1.3. In (1.7),  $n$  is the refractive index of the active layer and  $c$  the celerity of light in vacuum. In a laser diode, the refractive index  $n$  (phase optical index) varies with the frequency  $\omega$  (material dispersion) and strictly speaking the intermode spacing  $\delta\omega$  is as follows:

$$\delta\omega = \frac{\pi c}{nL} \quad (1.8)$$

The optical group index  $n_g$  which is dependent on frequency can be expressed as,

$$n_g = n + \omega \frac{\partial n}{\partial \omega} \quad (1.9)$$

The round-trip time  $\delta\tau$  of the laser is related to  $\delta\omega$  following the relation:

$$\delta\tau = \frac{2\pi}{\delta\omega} = \frac{2nL}{c} \quad (1.10)$$

Let us consider the case of a  $300 \mu\text{m}$  long InGaAsP laser. In the wavelength range of  $1.5 \mu\text{m}$ , we have  $n=3.5$  and  $n_g=4$ . The longitudinal modes spacing is  $\delta\nu \approx 100\text{-}150 \text{ GHz}$  or  $\delta\lambda = \frac{\lambda^2 \delta\nu}{c} \approx 1 \text{ nm}$ . Using typical values for  $\Gamma$ ,  $\alpha_i$ ,  $R_1$  and  $R_2$  in (1.5), a material gain of about  $100\text{-}150 \text{ cm}^{-1}$  is required to achieve threshold conditions. The gain bandwidth of semiconductor lasers is very broad as compared with  $\delta\nu$  and in practice this generally results in multi-longitudinal mode operation. Normally, there are several modes that meet the phase condition described by equation (1.6) and exhibit gains that are only slightly smaller ( $\approx 10^{-3}\text{-}10^{-4}$ ) than the threshold gain (1.5). Single-mode operation can be achieved if the threshold gain for the oscillating mode significantly smaller than that for the other modes.

### 1.1.3 Output Light-Current Characteristic

Let us now focus on the light-current characteristic (LCC) of semiconductor lasers. The interband radiative recombination leads to either spontaneous or stimulated emission. The

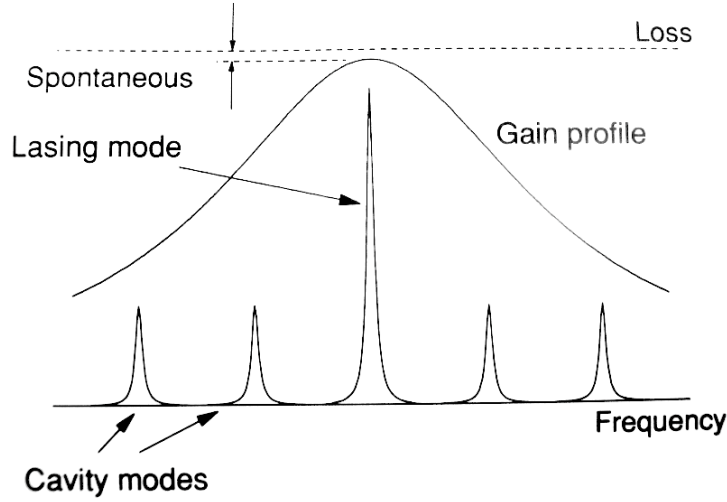


Figure 1.3: Schematic illustration of longitudinal modes and the gain profile of a Fabry-Perot diode laser. The threshold is reached when the spontaneous emission and optical gain equal loss for the mode in the vicinity of the gain peak

electron-hole recombination rate  $R(N)$  can reasonably be written such as:

$$R(N) = AN + BN^2 + CN^3 + R_{st}N_{ph} \quad (1.11)$$

where  $R_{st}$  describes the net rate of stimulated emission,  $N_{ph}$  is the intracavity photon density and A, B, and C are the parameters of spontaneous recombination. The cubic term  $CN^3$  referred to as Auger recombination whose inclusion is of first importance for long-wavelength semiconductor lasers. The bimolecular coefficient  $B$  is known to be dependent on  $N$  and is often approximated by  $B = B_0 - B_1N$ . The stimulated emission term is directly proportional to the optical gain,

$$R_{st} = \frac{c}{n_g} g(N) \quad (1.12)$$

Assuming a linear dependence of the optical gain on the carrier concentration, one obtains for the ideal LCC above the laser threshold the following relationship,

$$P(I) = \frac{\hbar\omega}{2e} \frac{\alpha_m}{\alpha_m + \alpha_i} (I - I_{th}) \quad (1.13)$$

where  $e$  is the electronic charge and  $\alpha_m$  the mirror loss:

$$\alpha_m = \frac{1}{2L} \ln \left( \frac{1}{R_1 R_2} \right) \quad (1.14)$$

Equation (1.13) represents a linear LCC as the one shown in figure 1.4. The slope of the curve is reasonably constant until the power saturation mechanisms settle in (not shown in figure 1.4). The saturation of the power is connected with the thermal heating of the device. The

threshold current  $I_{th}$  is dependent on the temperature  $T$  and its behavior can be empirically described as follows:

$$I_{th} \propto \exp(T/T_0) \quad (1.15)$$

$T_0$  represents the characteristic temperature; typical values of  $T_0$  are in the range of 150-200K for GaAlAs lasers and 40-70K for InGaAsP lasers. Despite the temperature behavior of the threshold current is a little bit more complicated, (1.15) gives a quite reasonable description.

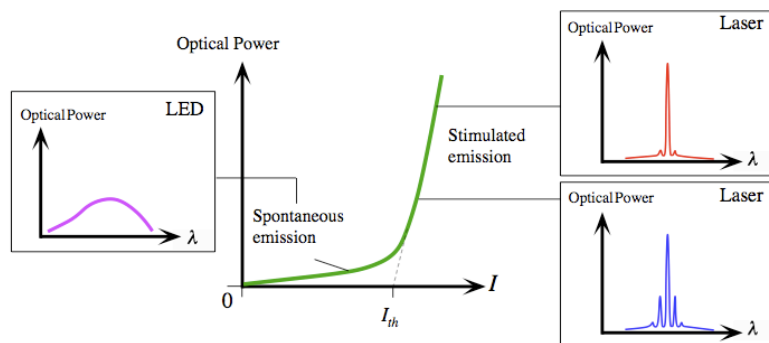


Figure 1.4: The typical light-current characteristic (LCC) of semiconductor laser and the corresponding output spectrum

#### 1.1.4 Carrier Confinement

Although the pn junction can amplify the electromagnetic radiation and exhibits optical gain under forward bias, the thickness of the region in which the gain is sufficiently high is very small (in the range of  $0.01 \mu\text{m}$ ). This is because there is no mechanism to confine carriers; usually homojunctions lasers failed to operate at room temperature. The carrier confinement in the plane perpendicular to the pn junction can be achieved using heterojunctions. A double heterojunction is used to prevent electron-hole spreading from the pn junction where the carriers recombine. Figure 1.5 shows the energy-band diagram of a double heterostructure laser (DH). The active layer is sandwiched by two claddings layers that have wider band gaps. The pn junction is biased in the forward direction. Due to the external voltage, an injection of holes from the p-doped layer and an injection of electron from the n-doped side occur into the active layer. The potential barriers on the boundaries between the layers resulting from the band-gap differences prevent electrons and holes from spreading into the cladding layers. The concentration of minority carriers can easily reach very high values in the active layer. This

leads to lasing under much lower current densities as compared with homojunction lasers. Heterojunction based lasers allow to operate at room temperature and beyond.

Lateral confinement of injected carriers is also very important. As an example, figure 1.6

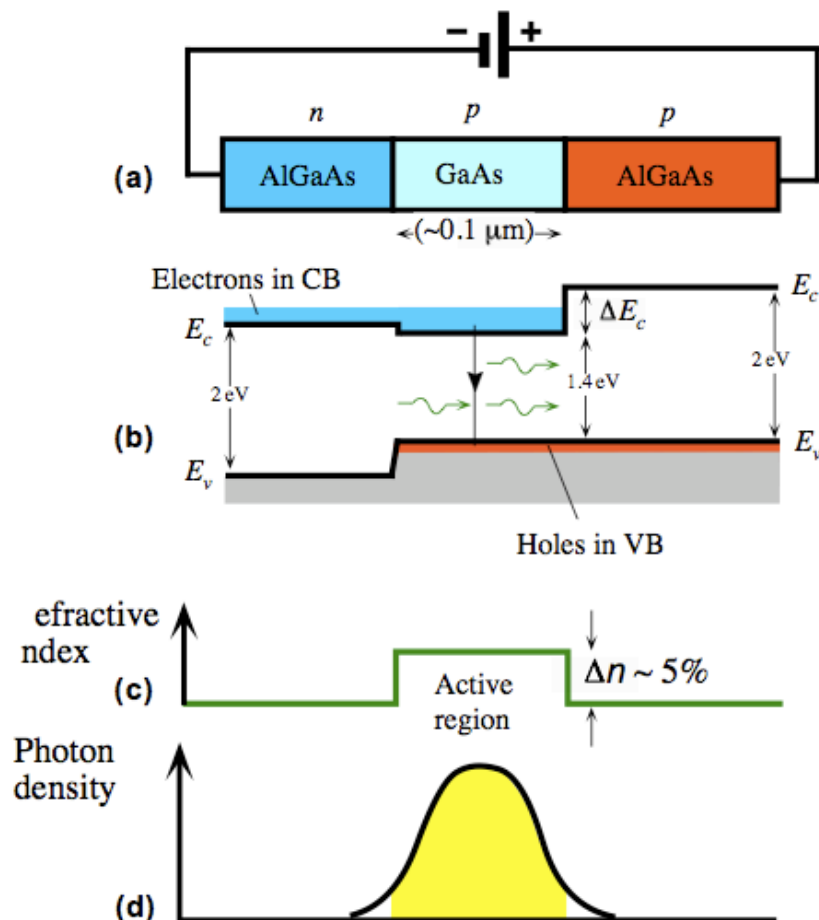


Figure 1.5: (a) A double heterostructure diode has two junctions which are between two different bandgap semiconductors (GaAs and AlGaAs); (b) Simplified energyband diagram under a large forward bias. Lasing recombination takes place in the p-GaAs layer, the active layer; (c) Higher bandgap materials have a lower refractive index; (d) AlGaAs layers provide lateral optical confinement

and figure 1.7 show two types of laser structures that are designed for lateral confinement. Both lasers have a narrow stripe contact typically in the range of  $2\text{-}5 \mu\text{m}$ . The stripe restricts the region where electron and holes injection occurs. Numerous laser structures for lateral confinement have been proposed over the years such as buried heterostructure lasers, rib waveguide laser and ridge waveguide lasers.

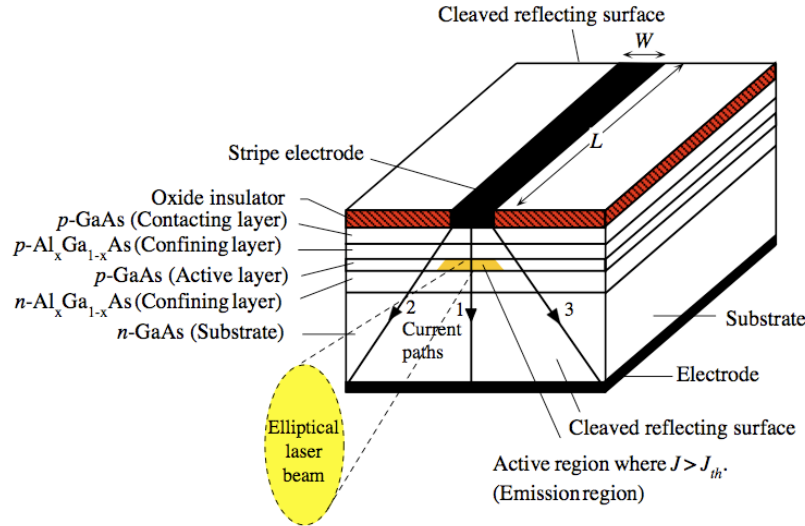


Figure 1.6: Schematic illustration of the the structure of a double heterojunction stripe contact laser diode

### 1.1.5 Optical Field Confinement and Spatial Modes

By laterally confining the injection current and the carriers, the efficiency of the laser can be improved and the beam shape of the light output can be made more suitable for various applications. Optical field confinement may also be achieved by laterally varying the effective refractive index, that is, by either changing the material composition or the shape of the waveguide. In the transverse direction, perpendicular to the junction plane, the refractive index discontinuity between the active and cladding layers is responsible for the optical field confinement through the total internal reflection occurring at the interfaces. In gain-guided lasers (see figure 1.6), the stripe restricts the injection of carriers in the lateral direction. Optical field confinement in this direction is due to both the nonuniform distribution of the refractive index and the nonuniform distribution of the gain/loss. Small variations that occur in the refractive index result in variation of gain/loss and vice versa. In stripe geometry lasers, the refractive index is lower at the center of the stripe, which produces an antiguiding effect that is only overcome by the sharply peaked gain profile. This leads to the generation of light along the axis of the stripe while much light is absorbed in the lossy regions at the edges of the strip. For wide stripe (over 7 to 10  $\mu\text{m}$ ), the self-focusing effect and excitation of higher lateral modes can occur. In index-guided lasers (see figure 1.7), lateral index steps due to additional blocking layers confine the mode. Gain-guided lasers have a number of undesirable characteristics that become worse for long-wavelength lasers. As a consequence of that, index-guided are most preferable due to their improved performances. In order to

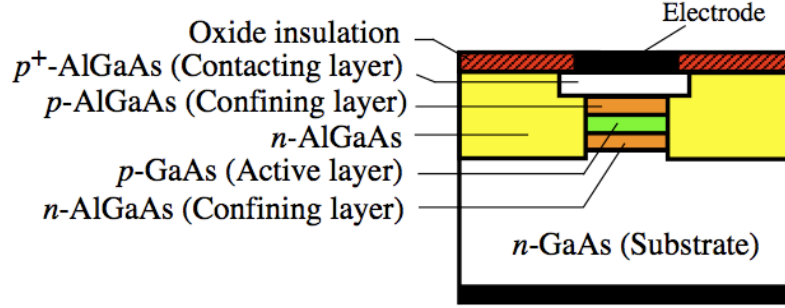


Figure 1.7: Schematic illustration of the cross sectional structure of a buried heterostructure laser diode

calculate the optical field confinement, the confinement factor  $\Gamma$  is normally introduced. In the transverse direction, values of this parameter can be calculated using a normalized active layer thickness  $D$ ,

$$D = \frac{2\pi d}{\lambda} (n^2 - n_c^2)^{1/2} \quad (1.16)$$

where  $d$  is the true active layer thickness and  $n$  and  $n_c$  are the refractive indices of the active and cladding layers, respectively. As the value of  $D$  decreases, the optical wave spreads into the cladding regions whereas at large values, the optical field gets extremely well-confined and  $\Gamma$  approaches the unity. A useful approximation for the transverse confinement factor  $\Gamma_T$  accurate within 1.5% is given by,

$$\Gamma_T = \frac{D^2}{2 + D^2} \quad (1.17)$$

To ensure single transverse-mode behavior,  $D$  must be less than  $\pi$ . Since typically  $d \leq 0.2 \mu\text{m}$ , the single transverse-mode condition is always satisfied in practical devices.

The treatment of spatial modes is really different depending on whether gain guiding or index guiding is used to confine the optical field. In gain-guided based devices, the carrier diffusion plays an important role and the carrier concentration is laterally nonuniform. Let us stress that in general, a numerical approach is required to solve the problem of determining the lateral modes in gain-guided lasers. The number of lateral modes in such devices depends on the strip width  $w$ . When  $w < 10 \mu\text{m}$ , only the fundamental mode can be considered in the structure. In case of strongly index-guided based lasers, it is possible to define the normalized waveguide width  $W$  such as:

$$W = \frac{2\pi w}{\lambda} (n_{eff}^2 - n_{eff,c}^2)^{1/2} \quad (1.18)$$

where  $n_{eff}$  and  $n_{eff,c}$  are the effective indices of the active and cladding layers. In analogy to (1.17), the lateral confinement factor  $\Gamma_L$  is given by,

$$\Gamma_T = \frac{W^2}{2 + W^2} \quad (1.19)$$

The mode confinement factor  $\Gamma$  can be written as  $\Gamma = \Gamma_L \Gamma_T$ . For index-guided lasers, typically  $w \approx 2-3 \mu\text{m}$ ,  $\Gamma_L \approx 1$  and  $\Gamma \approx \Gamma_T$ . To summarize, it is just important to emphasize that the problem of spatial modes in semiconductor laser is the problem of modes of a slab waveguide based upon on the solutions of Maxwell's equations. A slab waveguide can usually support two types of modes named either transverse electric (TE) or transverse magnetic (TM). As regards TE modes, the electric field is polarized along the pn junction plane while it is the magnetic field for TM modes. In heterostructure lasers, the TE modes are usually favored over the TM ones because the threshold gain is lower for TE-polarization due to higher facet reflectivities and a higher optical confinement factor.

### 1.1.6 Near- and Far-Field Patterns

As shown in figure 1.8, semiconductor laser emits in a form of spot that has an elliptical cross section. The spatial distribution of the emitted light near the facet is called as the near field pattern. The angular intensity distribution far from the laser is the far-field pattern. In general, several spatial modes may be excited in the structure and the resulting near- and far-fields can be seen a superposition of them. However, the width and the thickness of the active layer are usually chosen such that only the fundamental transverse and lateral modes are supported by the waveguide. The near-field emission pattern for a fundamental transverse mode of the symmetric slab waveguide has a full width at half maximum (FWHM)  $w_{\perp}$ , which can be approximated by:

$$w_{\perp} \approx d(2 \ln(2))^{1/2} (0.321 + 2.1D^{-3/2} + 4D^{-6}) \quad (1.20)$$

where the normalized thickness  $D$  is determined by (1.16). The previous approximation is usually enough accurate for  $1.8 < D < 6.0$ . For this case, the far-field emission pattern has a beamwidth  $\Theta_{\perp}$  such that,

$$\Theta_{\perp} \approx \frac{0.65D(n^2 - n_c^2)^{1/2}}{1 + 0.15(1 + n - n_c)D^2} \quad (1.21)$$

(1.21) is accurate within 3% for  $D < 2$ , which corresponds to  $d < 0.3 \mu\text{m}$  for  $1.55 \mu\text{m}$  InGaAsP lasers. The near-field parallel to the junction plane depends critically on the lateral guiding mechanism and exhibits different behavior for gain-guided and index-guided lasers. For a strongly index-guided laser, the near-field behavior in the lateral direction is similar to that for the transverse direction. To calculate the FWHM of the near-field  $w_{\parallel}$ , (1.20) can be applied

upon replacing  $D$  by  $W$  given by (1.18). It can be shown that the near field in strongly-index-guided lasers is largely confined within the active layer and  $w_{\parallel}$  is approximately equal to the width of the active layer. For weakly index-guided lasers, the lateral confinement of the optical field can be improved by varying the lateral index step. For instance, an index step from 0.005 to 0.01 is enough to achieve the index-guided regime and hence  $w_{\parallel}$  will be equal to the width of the central region of the active layer where the lateral confinement of carriers and the optical field occurs. As for gain-guided lasers, the problem of finding the exact near- and far-field patterns remains a difficult task because analytically insoluble. As a result a lot of assumptions are required as well as significant numerical solutions. It can be shown that  $w_{\parallel}$  and  $\Theta_{\parallel}$  are dependent upon the driving current amplitude, the stripe of the width, the effective lateral-diffusion length of carriers, the active layer thickness, the resistivities and thicknesses of the various layers below the stripe contact.

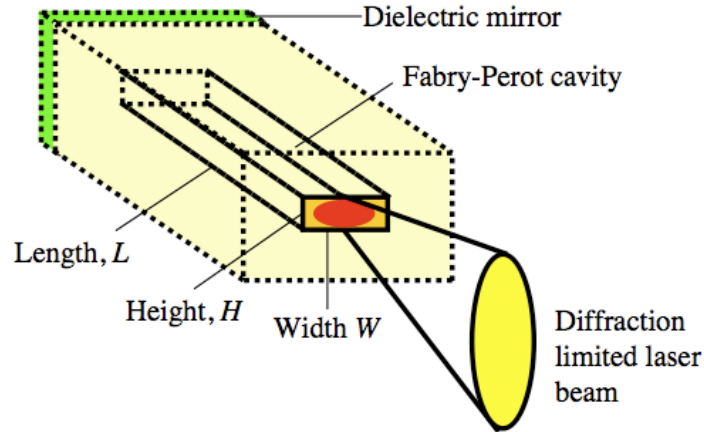


Figure 1.8: The laser cavity definitions and the output laser beam characteristics

## 1.2 Quantum Well Lasers

Thanks to the ability to grow epitaxially thin layers of semiconductor materials, new laser structures have been realized. In quantum well (QW) lasers, the thickness of the active layer is reduced from approximately  $1 \mu\text{m}$  to 2-10 nm. Single QW lasers and multiple QW lasers have been fabricated. The active layer thickness in QW lasers is of the order of the de Broglie wavelength of electrons in a semiconductor, which is  $\lambda_d = h/p$  where  $p$  is the electron momentum and  $h$  the Planck's constant. Quantum size effects arise from the confinement of carriers to the potential wells formed by conduction and valence bands as described in figure 1.9. The motion of electrons and holes in the active layer is quantized for the component perpendicular

to the wells. Thus, the energy of electrons and holes moving in the direction of confinement is quantized into discrete energy levels. The lowest energy radiative transition occurs at a photon energy that is significantly higher than the band gap of the material. The lasing

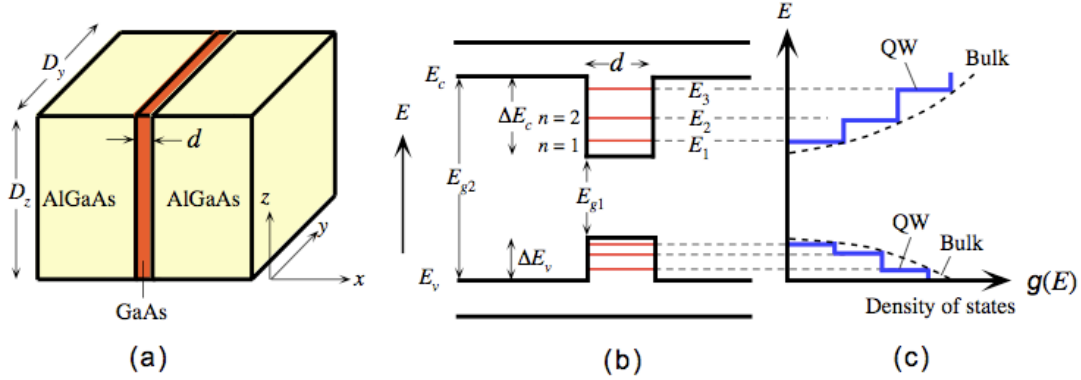


Figure 1.9: A quantum well (QW) device. (a) Schematic illustration of a quantum well (QW) structure in which a thin layer of GaAs is sandwiched between two wider bandgap semiconductors (AlGaAs); (b) The conduction electrons in the GaAs layer are confined in the  $x$ -direction to a small length  $d$  so that their energy is quantized; (c) The density of states (DOS) of a two-dimensional QW. The density of states is constant at each quantized energy level

action usually happens on the transition between the lowest conduction-band subband and the highest heavy hole subband of the valence band. The photon energy depends on the well width and increases to higher values as the width decreases. On the other hand, the carriers are free to move in a direction parallel to the heterojunction. This one-directional confinement means that the density of states (DOS) will be that of a two-dimensional system rather than of a familiar three-dimensional one for bulk semiconductor lasers. Figure 1.9 show such difference: the staircase DOS endows QW lasers with higher differential gain, lower threshold current densities and improved temperature performance. Their enhanced differential gain gives QW lasers the potential to achieve higher modulation bandwidths when compared with bulk devices. Narrower optical gain spectra should be also achieved, leading to fewer lasing modes. However, if more than one energy subbands are excited, the width of the optical gain spectra can significantly exceed that of a bulk device. Fluctuations in the well size can also lead to a considerable broadening of the gain spectra of quantum confined lasers and also a reduction of the gain peak. The gain of QW lasers is also strongly polarization-dependent. For narrow enough wells, the maximum TE gain is greater at lower energy than the gain for TM polarized light. Also, as compared to bulk lasers, QW ones exhibit a much higher differential gain and differential refractive index as well as a reduced linewidth enhancement

factor. Therefore, the high speed characteristics of those devices are of great interest for high speed lightwave system.

**Note:** There has been a considerable interest in strained-layer QWs. The lattice-mismatched QW structure can be used to design a laser with the optimal threshold condition since that strain alters the sub-band structure and optical gain of QW lasers. Basically, the threshold current can increase or decrease with stress depending on whether the laser operates in a TM or TE mode with zero stress. The differential gain and the linewidth enhancement factor can also be improved as compared to conventional QW devices.

### 1.3 Quantum Dot Lasers

Quantum dots (QDs) are nanometer-scale semiconductor inclusions in a host material which exhibit carrier confinement in all three dimensions (cf. figure 1.10). These new quantum objects are the climax of the reduction of the dimensionality that started thirty years ago with the quantum wells (QW). The principal advantage of using size-quantized heterostructures

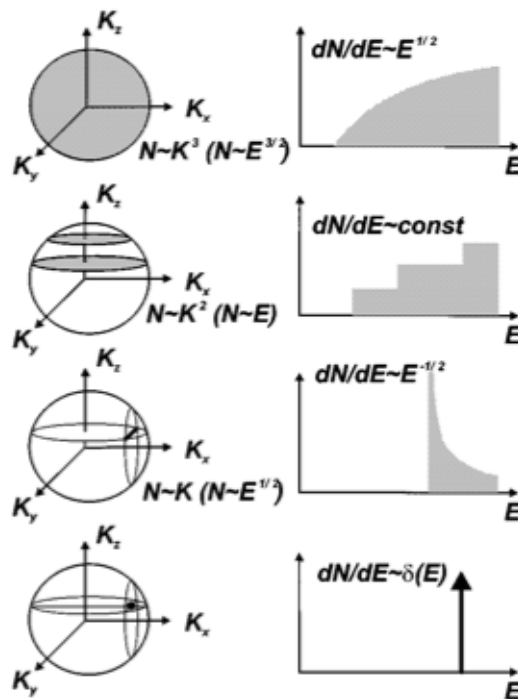


Figure 1.10: Density of states for charge carriers in structures with different dimensionalities

in lasers originates from the increase of the density of states for charge carriers near the

bandedges. Their electronic and optical properties can lead to large improvements of devices such as lasers or detectors. Due to their pseudo atom like energy band structure and to their semiconductor like carrier injection properties they combine the best of the two worlds high optical gain and high injection efficiency due to the absence of energy band dispersion. Tremendous efforts have been carried out towards the improvement of device performances. For the last decade, QD lasers and devices have been the subject of considerable interest owing to expected unique properties that result from the 3D confinement of charge carriers. Higher gain, higher differential gain, lower threshold current, higher characteristic temperature and reduced linewidth enhancement factor were theoretically predicted. These properties should pave the way for uncooled isolator-free operation, high speed directly modulated lasers and penalty-free data transmission on long transmission spans. As illustrated in figure 1.11(a), these atomic-like nanostructures can theoretically offer superior laser performance compared to that of their Quantum Well (QW) based counterparts at a lower cost as shown in figure 1.12 as regards the reduced threshold current density. This would allow to increase equipment density per unit volume or area and significantly reduce capital expenditure for a given data rate and transmission distance.

During the last ten years, a few approaches have been developed worldwide to fabricate InP-lasers based on low dimensional nanostructures and emitting at  $1.55 \mu\text{m}$ . Using the standard InP (100) substrates, the growth of thin InAs layers leads to the formation of elongated dots, called dashes (cf. figure 1.11(b)), due to the relatively low lattice mismatch between InAs and InP (4%). QDash lasers with gain and threshold current density similar to multi quantum-wells (MQWs), up to  $50 \text{ cm}^{-1}$  and less than  $0.8 \text{ kA/cm}^2$ , have been achieved and used to evaluate the potential of this technology for telecom applications.

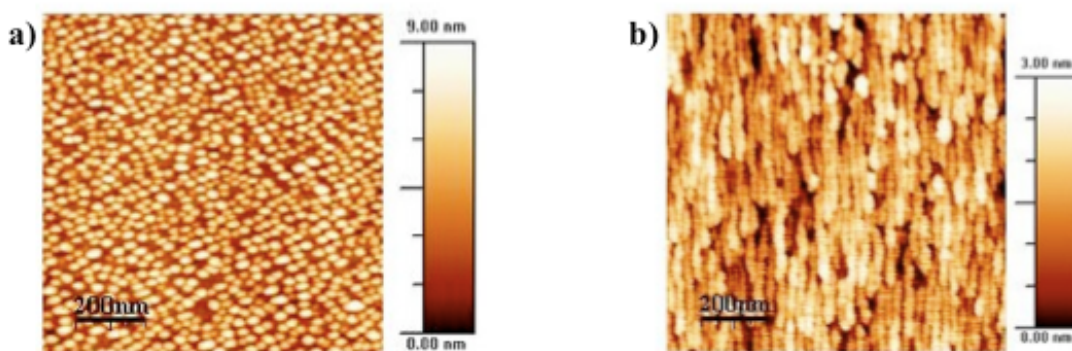


Figure 1.11: (a)  $1 \times 1 \mu\text{m}^2$  Atomic Force Microscopy images of the corresponding InAs QDs and (b) QDashes grown on InP substrate.

In order to enhance the 3D confinement QDs have been grown using different techniques and substrate orientations but the performances of single mode lasers remain similar or infe-

rior to those of QDash lasers. An interesting approach consists in using InP(311)B substrates to grow truly three dimensional QDs (cf. figure 1.11(a)). Relatively low gain but ultra low threshold current density of  $170 \text{ A/cm}^{-2}$  have been achieved in broad-area lasers. Recent advances in the growth optimization of InAs/InP QDash lasers have led to a threshold current of about 10 mA for as cleaved  $600 \mu\text{m}$ -long FP lasers in buried ridge stripe (BRS) and 30 mA in ridge lasers (RWG). Output power up to 25 mW has been demonstrated. In terms of temperature resistance, most of the high temperature performances reported in the literature are measured in pulsed operation around the room temperature (200 K). The highest characteristic temperature  $T_0$  of FP lasers in the  $25\text{-}85^\circ\text{C}$  range is 130 K with a threshold current of about 100 mA due to a high p-type doping level of the active layer. The most promising results, based on the optimization of Dot-in-a-Well (DWELL) design, reports a  $T_0$  of 80 K keeping a threshold current as low as 10 mA. Improvement of the QDash based active layers (modal gain, differential gain) in the last two years allowed the achievement of a -3 dB direct modulation bandwidth of 10 GHz. 10 Gbps large signal transmission up to 25 km over the  $25\text{-}85^\circ\text{C}$  temperature range has been demonstrated, in direct competition with the best Al-based MQWs. Moreover, QDash based 10 Gbps directly modulated lasers fully comply with the 10 Gbps Ethernet standard on isolatorless operation over the  $25\text{-}85^\circ\text{C}$  range. The 3D car-

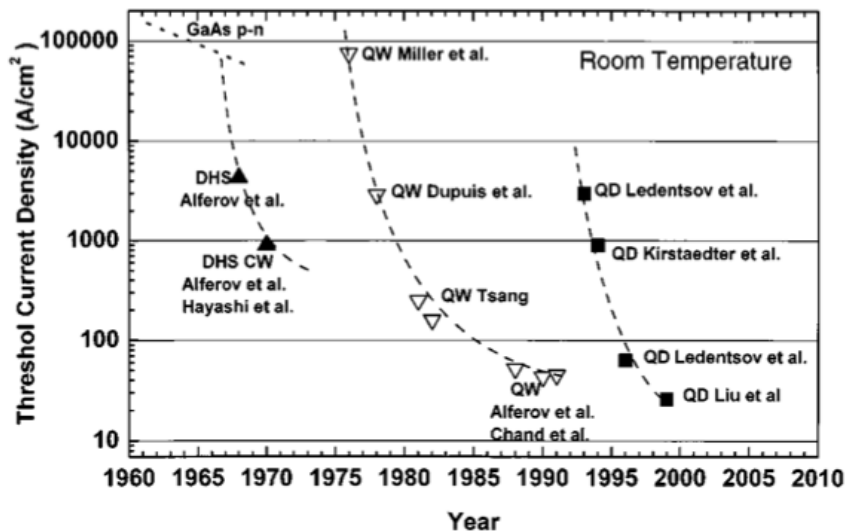


Figure 1.12: Evolution of the threshold current density for Bulk, QW, QD lasers

rier confinement of QDs further leads to remarkable properties such as enhanced non linear effects. Indeed, stable mode-locking has been observed from single section Fabry Perot laser diodes based on QDots/QDashes grown on InP substrates, without resorting to a saturable absorber section. This is attributed to the enhanced four wave mixing efficiency (FWM) in this novel material system. Moreover, analysis of the Radio Frequency (RF) spectrum

showed an ultra narrow beat note linewidth of the order of a few kHz, typically two orders of magnitude lower than that of conventional QW based Mode Locked Lasers (MLLs). This is the signature of a low phase noise of QD lasers, implying low timing jitter. Hence, QD MLLs have been shown to fulfil the International Telecommunication Union (ITU) requirement for all-optical clock recovery at 40 Gb/s and used for low-noise optoelectronic oscillators. Similarly, two-section InAs/GaAs QDs MLLs have demonstrated superior performances in terms of pulse duration and timing jitter compared to QW based MLLs.

## 1.4 Single-Frequency Lasers

Since an important feature of laser emission is its coherency, it is desirable for a vast majority of applications to have as narrow an optical spectrum as possible. A variety of single-mode laser structures have been proposed: short-cavity lasers, coupled-cavity lasers, injection-locked lasers, distributed Bragg reflector (DBR) lasers and distributed feedback (DFB) lasers. All of these structures are briefly reviewed in this section.

### 1.4.1 Short-Cavity Lasers

Short-cavity lasers are the simplest of the single-mode lasers. If a short FP cavity is used, the frequency spacing between longitudinal modes gets large. When the cavity length is chosen so that the mode spacing is comparable to the width of the optical gain spectrum, only one mode is close enough to the gain peak to lase. However, shortening the laser cavity reduces the available optical gain. Therefore, to achieve lasing, the active layer must have a very high gain and the optical feedback must be maximized. Short-cavity lasers with enhanced facet reflectivities ( $>0.85$ ) can operate under CW conditions in a single-mode. The typical cavity length of a short-cavity laser is in the range from 50  $\mu\text{m}$  to 100  $\mu\text{m}$ .

### 1.4.2 Coupled-Cavity Lasers

Single-mode operation can be achieved by coupling light between two cavities. External-cavity lasers consist of one FP cavity providing the optical gain and an external cavity providing additional wavelength-dependent optical feedback. In-phase feedback occurs for only those laser modes whose lasing wavelength coincides with one of the longitudinal modes of the external cavity. The longitudinal mode that is closest to the gain peak and has the lowest cavity loss becomes the dominant mode. A diffraction grating, an external mirror or a FP etalon can be used to provide feedback in external-cavity lasers. Although these devices present a high side-mode suppression ratio (SMSR) and are highly tunable, they remain difficult to integrate and suffer from a lack of mechanical and thermal stability.

$C^3$  lasers offer monolithic construction. A  $C^3$  laser is shown in figure 1.13. It has two FP sections, although driven independently, are optically coupled through their mutual feedback. The coupling element is simply an air gap which is of about  $5 \mu\text{m}$  wide (the gap is nearly an integer multiple of  $\lambda/2$ ).  $C^3$  lasers can also provide a high SMSR provided the gain difference between the mode with the lowest threshold gain and the neighboring mode is in the range of  $4\text{-}5 \text{ cm}^{-1}$ . It has been also observed that the frequency chirp of such devices can be reduced typically by a factor of two, through proper adjustment of the device currents. It has also been observed that the output power of  $C^3$  lasers displays bistability and hysteresis. Optical bistability may be useful for a number of signal-processing functions such as optical logic operations or optical switching.

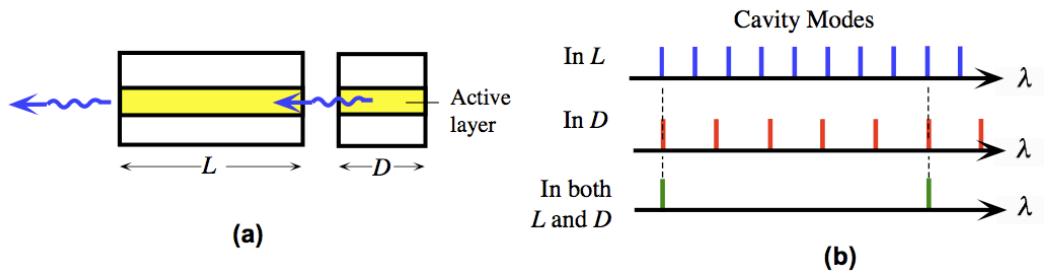


Figure 1.13: Schematic illustration of a cleaved coupled-cavity  $C^3$  laser

### 1.4.3 Injection-Locked Lasers

Single-mode emission may be achieved using the injection-locking technique. The injection-locking technique is based on light injection from a master laser into the cavity of a slave laser as shown in figure 1.14. If the wavelength of the injected light is within a certain detuning

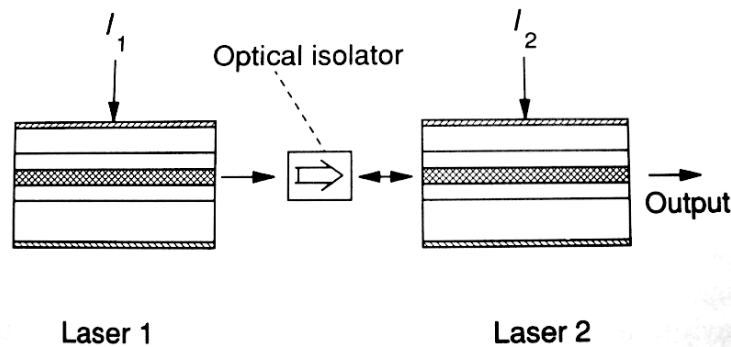


Figure 1.14: Schematic illustration of an injection-locked laser

range, which depends mainly on the injected power, the frequency of the slave laser locks onto

that of the master laser. To prevent light emitted by the slave laser from feeding back into the master, it is necessary to insert an optical isolator in-between. Thus, as shown in figure 1.15, when a Fabry-Perot laser is locked onto a single-mode signal, its operation becomes single-mode. The injection-locked Fabry-Perot laser can be used as a standard component for optical access networks and for tunable photonic oscillators.

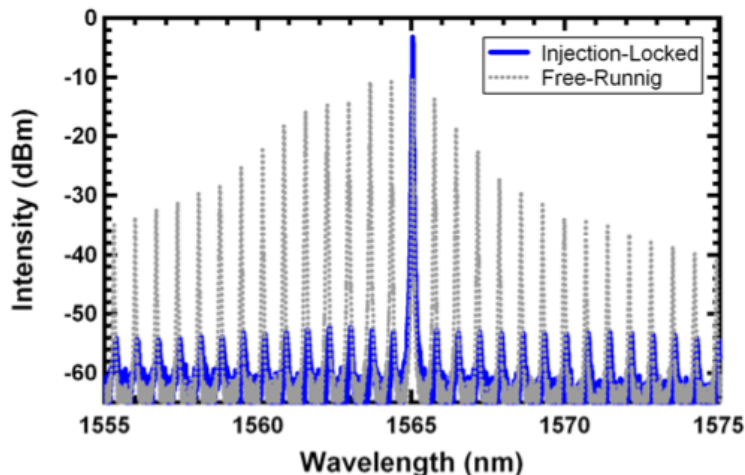


Figure 1.15: Single-mode generation using a Fabry-Perot injection-locked laser

#### 1.4.4 DBR Lasers

DBR lasers employ in-plane periodic structures to provide distributed frequency-selective feedback. The built-in grating leads to a periodic perturbation in the refractive index, and feedback occurs by Bragg diffraction. The first-order gratings are generally formed in the DBR regions with a coupling coefficient of about  $100 \text{ cm}^{-1}$ . The longitudinal mode closest to the Bragg wavelength has the lowest threshold gain. The Bragg wavelength  $\lambda_B$  is related to the pitch of the grating  $\Lambda$ :

$$\Lambda = q \frac{\lambda_B}{2n} \quad (1.22)$$

where  $n$  is the mode effective refractive index and the integer  $q$  represents the order of the Bragg diffraction. For instance, a first order grating has a pitch of  $0.23 \mu\text{m}$  at a wavelength of  $1.5 \mu\text{m}$  and for a typical value of  $n_{eff} \approx 3.4$ . DBR lasers use gratings etched outside the active region as shown in figure 1.16. These unpumped corrugated region act as frequency-selective mirrors. Here optical gain and wavelength tuning are provided by the active region and the Bragg section respectively. The passive phase-control section can be used to ensure single-mode operation. A DBR laser is usually designed such as the dominant mode has a threshold gain of about  $8\text{-}10 \text{ cm}^{-1}$  lower than the neighbor modes. These modes are typically

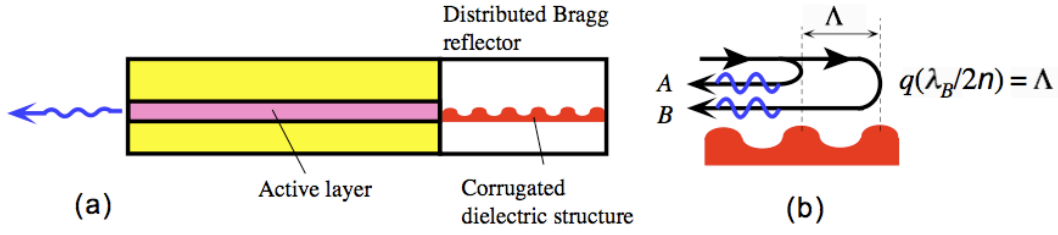


Figure 1.16: (a) Distributed Bragg reflection (DBR) laser principle; (b) Partially reflected waves at the corrugations can only constitute a reflected wave when the wavelength satisfies the Bragg condition. Reflected waves A and B interfere constructive when  $q(\lambda_B/2n) = \Lambda$

suppressed by  $\approx 30$  dB. In contrast to FP lasers, the longitudinal modes of a DBR laser are not equispaced. Because of its spectral purity, DBR lasers are promising for applications in optical fiber communications.

### 1.4.5 DFB Lasers

The feedback in DFB laser is provided by the grating that runs along the active region as shown in figure 1.17. Periodic perturbations in the refractive index along the laser cavity provide frequency-selective feedback. In a DFB device an optical wave traveling in one

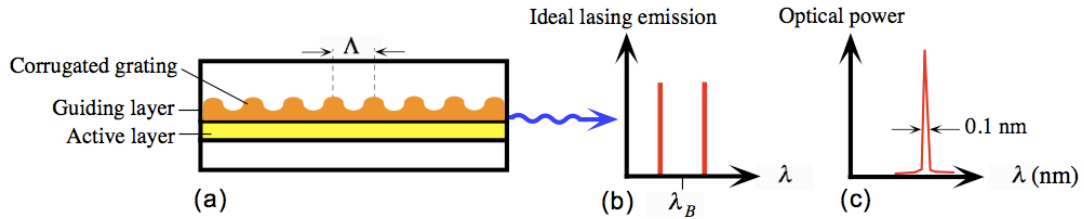


Figure 1.17: (a) Distributed feedback (DFB) laser structure; (b) Ideal lasing emission output; (c) Typical output spectrum from a DFB laser

direction is reflected by the grating into a traveling in the opposite direction and vice-versa. In other words, the optical field within the DFB cavity can be written as a superposition of counter-propagatives waves such as:

$$E(z) = E^+(z)e^{-i\beta_B z} + E^-(z)e^{i\beta_B z} \quad (1.23)$$

where  $E^+(z)$  et  $E^-(z)$  are the electric fields propagative either along the direction  $+z$  or  $-z$  respectively (see figure 1.18). The Bragg wavevector  $\beta_B$  is defined such as  $\beta_B = \frac{2\pi n}{\lambda_B}$ .

Let us stress that the description of the electric field  $E(z)$  through (1.23) comes from the theory of *Linear Combination of Atomic Orbitals* (LCAO). Coherent coupling between the counter-propagating waves occurs only for wavelengths that satisfy the Bragg condition given by (1.22). Then, starting from Maxwell's equations, one can write:

$$\nabla \times \mathbf{E} = -\mu_0 \frac{\partial \mathbf{H}}{\partial t} \quad (1.24)$$

$$\nabla \times \mathbf{H} = \epsilon(z) \frac{\partial \mathbf{E}}{\partial t} \quad (1.25)$$

with  $\nabla$ ,  $\mathbf{E}$ ,  $\mathbf{H}$ ,  $\epsilon(z)$  and  $\mu_0$  the *Nabla* operator, the electric field, the magnetic field, the dielectric permittivity of the material and the magnetic permeability in vacuum. Combining equations (1.24) et (1.25), the Helmholtz's equation describing the mode propagation within the structure can be written such as:

$$\nabla^2 \mathbf{E} + \beta^2(z) \mathbf{E} = 0 \quad (1.26)$$

with  $\beta(z)$  the wavevector associated to the propagation of the mode within the DFB cavity and defined as:  $\beta(z) = \beta_0 \sqrt{\frac{\epsilon(z)}{\epsilon_0}}$  where ( $\beta_0$  is the wavevector in vacuum and  $\epsilon_0$  the dielectric permittivity in vacuum). The periodic variation induced by the index modulation allows to extract through a first-order approximation both the real and imaginary parts  $n(z)$  and  $\alpha(z)$  of the effective index:

$$n(z) = n + \Delta n \cos(2\beta_B z) \quad (1.27)$$

$$\alpha(z) = \alpha + \Delta\alpha \cos(2\beta_B z) \quad (1.28)$$

where  $n$ ,  $\alpha$  the average values of  $n(z)$ ,  $\alpha(z)$  and  $\Delta n$ ,  $\Delta\alpha$  their amplitudes. Thus, based on Kramers-Krönig relations and by injecting equations (1.27) et (1.28) into  $\beta(z)$ , it comes:

$$\beta^2(z) = \beta_0^2 n^2 + 2i\alpha\beta_0 n + 4\kappa\beta_0 n \cos(2\beta_B z) \quad (1.29)$$

where  $\kappa = \frac{\pi\Delta n}{\lambda} + i\frac{\Delta\alpha}{2}$  is the grating coupling coefficient. Basically, this coefficient allows to estimate the strength of the interaction between the optical fields  $E^+(z)$  and  $E^-(z)$ . This parameter is mostly linked to the grating profile, its position from the active region as well as the thickness and composition of the different layers of the waveguide. Also, it should be noted that the coupling coefficient has a strong impact on the laser's external optical feedback sensitivity.

Let us now assume the slowly varying envelope conditions,  $\frac{d^2 E_{+,-}}{dz^2} \ll \frac{dE_{+,-}}{dz}$ . Injecting (1.23) and (1.29) into (1.26), it comes:

$$-\frac{dE^+(z)}{dz} + (\alpha - i\delta)E^+(z) = i\kappa E^-(z) \quad (1.30)$$

$$\frac{dE^-(z)}{dz} + (\alpha - i\delta)E^-(z) = i\kappa E^+(z) \quad (1.31)$$

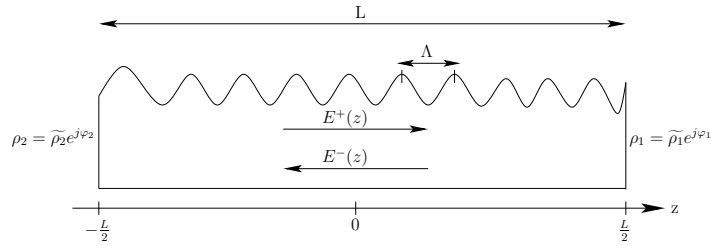


Figure 1.18: Schematic view of the counter-propagating optical fields in the DFB laser cavity

with  $\delta = \beta - \beta_B$  the Bragg deviation. Relationships (1.30) and (1.31) are the Kogelnik and Shank equations. This set of differential equations is also called coupled-waves equations because it takes into account the coupling between the counter-propagating fields through the grating coupling coefficient. The resolution of the Kogelnik and Shank equations allows to determine the transcendental equation of a DFB laser as well as the propagation constant by considering the reflections conditions at the laser's facets. Any finite values found for the propagation constant does correspond to a propagating mode into the DFB laser.

However it is important to point out that DFB lasers with uniform gratings and cavities

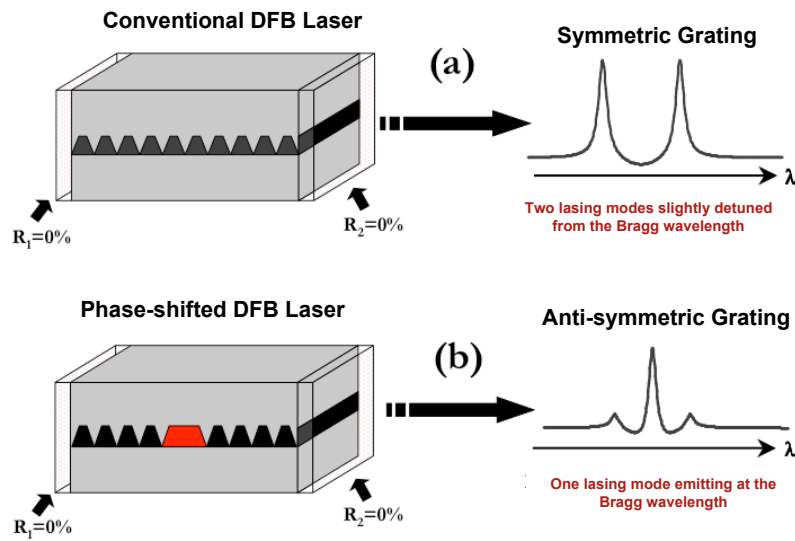


Figure 1.19: Illustration of the competition between the lasing modes in (a) a conventional DFB laser and (b) a phase-shifted DFB laser

do not lase at the Bragg wavelength. Instead, two-mode lasing can occur on either side of the stop-band (see figure 1.19). In order to avoid two-mode emission, an additional phase-shift of  $\pm\pi$  for the round-trip gain can be introduced. This condition implies that both counter-propagating waves should suffer a  $\pi/2$  or  $\lambda/4$  phase-shift. As shown in figure 1.19, phase-shifting the grating by  $\lambda/4$  in the middle of the laser moves the lasing mode to the Bragg wavelength. If antireflection coatings are used in addition to the phase-shift, much higher gain margins can be achieved, ensuring dynamic single-mode operation. However, phase-shift based lasers suffer from longitudinal spatial hole burning (LSHB). Here, lasers with strongly coupled gratings experience increased optical intensity in the region of the phase-shift at the center of the cavity. This leads to a reduced carrier concentration at the center of the laser, compared with at the facets (the spatial hole). DFB lasers still suffer from wavelength chirp during high-speed modulation and during ultrashort light pulse generation because the carrier-induced variation of the refractive index of the laser cavity causes the effective pitch of the grating to change.

**Note:** For a DFB laser it should be noted that both the optical confinement factor and the grating coupling coefficient are different for TE and TM modes. From a practical point of view, the important parameter is the threshold margin between the TE and TM modes. Thus, it can be shown that the threshold margin is considerably smaller for a DFB laser as compared to a FP one. For some values of active layer thickness, the threshold margin is so small that both TE and TM modes may laser almost simultaneously.



## Chapter 2

# Advances in Measurements of Physical Parameters of Semiconductor Lasers

The fast growing use of semiconductor lasers in various fields including fiber telecommunication systems, optical data storage, remote sensing places very stringent requirements on device performance. This requires a detailed understanding of physical processes governing the behavior of laser diodes. In this review, a broad set of electrical and optical techniques is described which gives complimentary information on the operation of the laser diode. Physical processes below threshold are critical in determining the operating point of the laser. Therefore studying the electrical characteristics and optical emission below laser's threshold is often more informative in the process of understanding the device performance. Some other parameters such as leakage current or wavelength chirp can only be deduced from above threshold measurements. Most of the experimental techniques presented in this chapter are in relation to telecommunications lasers. These lasers are usually designed so the output radiation can be coupled into a the single-mode fiber. These measurements provide critical experimental feedback in the process of laser diode optimization.

### 2.1 Measurements of the Optical Gain

One of the most important parameters relating the physical properties of the semiconductor structure to output characteristics of the laser diodes is the optical gain. Optical gain and its dependence on the operating conditions determine not only the basic output characteristics, such as the threshold current, but also the temperature dependence of the output characteristics, as well as high-speed performance of the laser.

The electric wave in the resonator of semiconductor can be written as:

$$\mathbf{E} = \mathbf{E}_0(\mathbf{y}, \mathbf{z})\mathbf{e}^{j(\omega t - \mathbf{k}\mathbf{x})} \quad (2.1)$$

where  $\mathbf{E}_0(\mathbf{y}, \mathbf{z})$  is the magnitude of the field, and the complex propagation  $k$  is:

$$k(\lambda) = k' + jk'' = \frac{2\pi n_{eff}}{\lambda} - \frac{j}{2}g(\lambda) \quad (2.2)$$

with  $n_{eff}$  the effective index of refraction for the optical mode, and  $g$  the modal optical gain. The factor of two comes in because the optical gain is usually defined with respect to optical power, not optical field intensity. Modal optical gain  $g(\lambda)$  is related to the material optical gain  $G(\lambda)$ :

$$g(\lambda) = \Gamma G(\lambda) - \alpha_{tot} \quad (2.3)$$

where  $\Gamma$  is the optical confinement factor (the fraction of the transverse optical mode overlapping the active layer and therefore experiencing optical gain). The total optical loss  $\alpha_{tot}$  consists of mirror loss and internal loss, usually attributed to free-carrier absorption and scattering from waveguide imperfections:

$$\alpha_{tot} = \alpha_m + \alpha_i = \frac{1}{L} \ln \left( \frac{1}{\sqrt{R_1 R_2}} \right) + \alpha_i \quad (2.4)$$

with  $R_1, R_2$  the mirror reflectivities and  $L$  the cavity length. Let us also stress that the optical gain is defined in terms of variations such that:

$$\delta g = -2\delta k'' = -\frac{4\pi}{\lambda} \Gamma \delta n'' \quad (2.5)$$

### 2.1.1 Determination of the Optical Gain from the Amplified Spontaneous Emission

Figure 2.1 shows the spectra of amplified spontaneous emission (ASE) in the TE polarization for an 1.3  $\mu\text{m}$  buried heterostructure semiconductor laser with a bulk active region as well as uncoated mirror facets. The equation describing the dependence of the ASE intensity on the wavelength in the approximation of uniform gain inside the laser cavity is as follows:

$$I(\lambda) = \frac{B(1 + Re^{(\Gamma G - \alpha_i)L})(1 - R)}{(1 + Re^{(\Gamma G - \alpha_i)L})^2 - 4Re^{(\Gamma G - \alpha_i)L} \sin^2(\frac{2\pi L n}{\lambda})} \quad (2.6)$$

with  $R = \sqrt{R_1 R_2}$  and  $B$  the proportionality coefficient equal to the amount of ASE coupled into the lasing mode. B. Hakki and T. Paoli proposed to determine the modal optical gain from the contrast of the ASE spectra. Equation (2.6) is used to obtain:

$$g(\lambda) = \frac{1}{L} \ln \left( \frac{\sqrt{r(\lambda)} - 1}{\sqrt{r(\lambda)} + 1} \right) \quad (2.7)$$

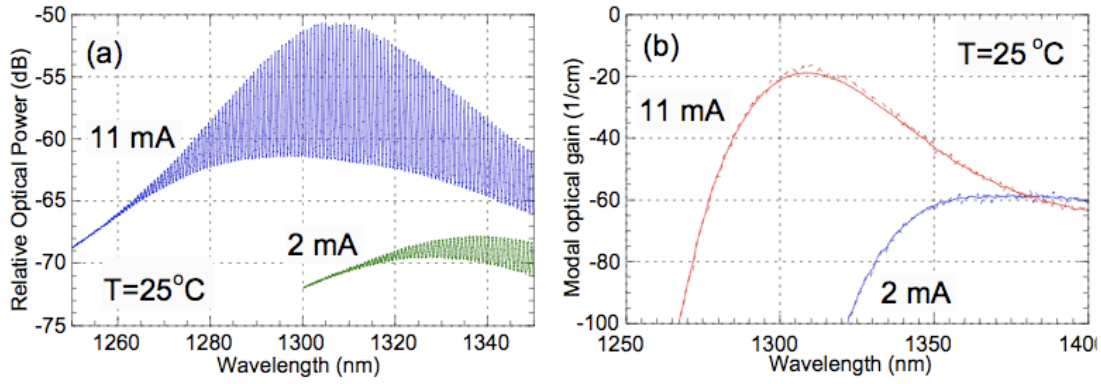


Figure 2.1: (a) The ASE spectra at room temperature for different currents; (b) modal optical gain extracted from these spectra using the Hakki-Paoli technique (solid line) and the Cassidy method (dashed line)

where  $r(\lambda)$  is the peak-to-valley ratio:

$$r(\lambda) = \frac{I_{max}(\lambda)}{I_{min}(\lambda)} \quad (2.8)$$

D. Cassidy proposed another way to analyze ASE in order to determine the material gain values. The optical gain in the oscillator system governed by (2.6) is:

$$g(\lambda) = \frac{1}{L} \ln \left( \frac{p(\lambda) - 1}{p(\lambda) + 1} \right) \quad (2.9)$$

where  $p$  is the ratio of the integral over one mode to the mode minimum:

$$p(\lambda) = \frac{\int_{\lambda_1}^{\lambda_2} I(\lambda') d\lambda'}{I_{min}(\lambda)(\lambda_2 - \lambda_1)} \quad (2.10)$$

It has been shown both theoretically and experimentally that this method also called the mode-sum method is less sensitive to the spectral bandwidth of the measurement system than the Hakki-Paoli technique. The modal optical gain extracted from the ASE spectra shown in figure 2.1(a) using the Hakki-Paoli and Cassidy techniques is shown in figure 2.1(b). Although the two methods give very similar results, there can be noticed some differences. First, in the high gain regime (11 mA around the gain maximum) the Hakki-Paoli technique slightly underestimates (by about  $5 \text{ cm}^{-1}$ ) the value of the modal optical gain. This effect can be attributed to the spectral resolution of the optical spectrum analyzer used in the experiment which is not enough adequate to resolve the ASE spectrum. Secondly, the Cassidy technique has higher noise due to inaccuracy in the detection of the wavelength of the mode minima.

### 2.1.2 Determination of the Optical Gain from the True Spontaneous Emission

This method is based on the general relations between the rates of spontaneous emission, stimulated emission and optical absorption. If carriers have a Fermi-like distribution functions, the material optical gain is related to the absorption coefficient in the following way:

$$G(E, E_F, T) = \alpha(E, E_F) \left( e^{\frac{E_F - E}{kT}} - 1 \right) \quad (2.11)$$

where  $E$  is the photon energy,  $E_F$  the separation between the quasi-Fermi levels of electrons and holes and  $\alpha(E, E_F)$  the absorption coefficient of the material of the active layer. Generally,  $\alpha(E, E_F)$  depends on the band filling and therefore on  $E$ . Another important relation related the intensity of spontaneous emission  $I_{sp}(E)$  to the absorption coefficient:

$$I_{sp} \propto E^2 \alpha(E, E_F) e^{\frac{E_F - E}{kT}} \quad (2.12)$$

where the proportionality sign allows for some constant factors to be omitted. They are of no importance because it is practically impossible to quantify the absolute measurements of the spontaneous. Merging the two previous equations we end-up with:

$$G(E, E_F, T) = \frac{I_{sp}(E)}{E^2} \left( 1 - e^{\frac{E - E_F}{kT}} \right) \quad (2.13)$$

In order to obtain the value of the material optical gain using (2.13), the value of the quasi-Fermi level separation  $E_F$  has to be known. Thus, by using the property of a Fabry-Perot laser to lase at the wavelength for which the material gain is maximum, the first derivative with respect to the wavelength is zero and it gives the value of the quasi-Fermi level separation at threshold. In order to determine such values at lower bias currents, it can be shown that at the high energies, the absorption coefficient is independent of the injection level. This allows the determination of the quasi-Fermi level separation below threshold. It is however important to emphasize that this procedure can lead to serious errors, since the quasi-Fermi level separation has to be determined with a very high accuracy in order for accurate calculation of the optical gain from TSE spectra. Attention has also to be paid to the carrier temperature which occurs in (2.13); this has to be considered since in the case of carrier heating, the carrier temperature is not equal to the lattice temperature.

One more condition is required to extract the gain spectra from the TSE spectra: equation (2.13) gives the value of the material optical gain in arbitrary units and a proper scaling factor need to be determined in order to find the material or modal gain. A way is to consider the situation of Fabry-Perot laser at threshold for which the maximum gain equals the total loss. If the laser has uncoated facets, the mirror loss can be easily calculated. Then, the value of the total loss can be estimated from the  $L - I$  curve slope with an assumption that the

internal efficiency is 100%. This approximation is not accurate in many cases, especially for lasers with coated mirrors or DFB/DBR devices. The last method is to directly use the known-value of the absorption coefficient above the absorption edge. Finally, the value of the total loss and quasi-Fermi level separation can also be determined using the transparency measurements.

The TSE spectra recorded from the side of an uncoated DFB laser at different currents are presented in figure 2.2(a). The TSE spectrum is much broader with no Fabry-Perot ripples and extends much further into high energies than the ASE because the TSE is not affected by reabsorption in the active layer. The modal optical gain spectra are plotted in figure 2.2(b) together with the spectra extracted from the ASE as described in the previous section. The gain spectrum extracted from the TSE is much wider than shown in figure 2.2(b) where the narrow wavelength range is chosen for the sake of comparing it to the gain spectrum extracted from the ASE.

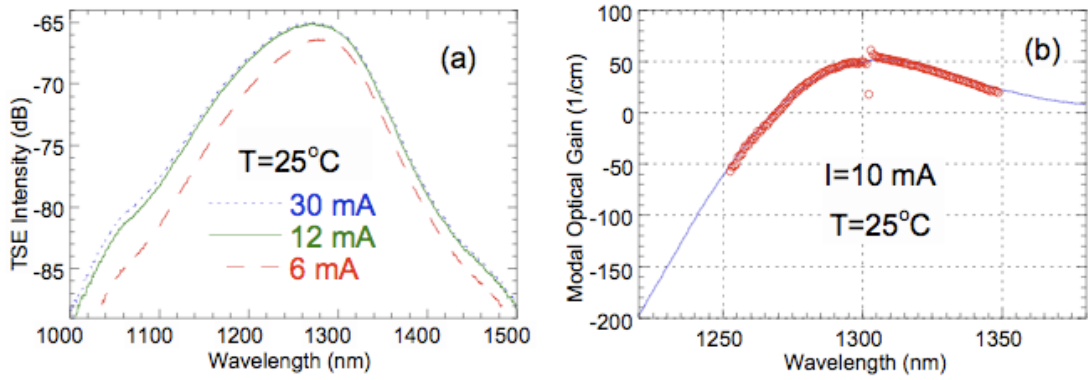


Figure 2.2: The TSE spectra at room temperature for different currents (a) and modal optical gain spectrum (b) extracted from the TSE spectra. The gain spectrum extracted from the ASE spectrum taken at the same conditions is also shown (circles)

It should be noted that the ASE spectrum of a DFB laser is distorted in the vicinity of the DFB wavelength. The modal optical gain curves extracted from the TSE and the ASE lie very close each other outside the vicinity of DFB wavelength. This confirms the validity of both techniques. Some discrepancy may arise partly from the fact that the total loss is a weak function of both energy and carrier concentration but was considered constant.

The advantage of the methods allowing for extraction of the modal optical gain from ASE is that, they give the absolute value of the gain, and, together with the transparency measurements, the total optical loss. The main disadvantage is that the modal optical gain is measured in fairly small intervals of both wavelength and gain. When the modal optical gain becomes too low, the ripple contrast in the ASE spectrum is too small to be measured

and analyzed accurately. Measurements based on the TSE spectra are not affected by the value or the spectral dependence of the mirror loss or grating. Thus, it can provide the true information about the optical gain in case ASE technique is not suitable. Another advantage is the much wider spectral range of measurements.

## 2.2 Measurement of the Optical Loss

Internal optical loss is a fundamental characteristics of a semiconductor laser. The value of internal loss affects threshold current and external slope efficiency. The optical loss has a number of different contributions; the most important among them are the free-carrier absorption (intraband process) and scattering loss on the waveguide nonuniformities. An early and widely technique for measurement of internal optical loss requires a set of lasers, varying in length but otherwise equivalent, in order to estimate the average value of loss as well as the internal quantum efficiency. This method does not take into account the systematic variation of the threshold condition due to variation in length and random variation between lasers. Also injection might not be a constant value across the set of different samples due to incomplete Fermi level pinning resulting from the carrier leakage. As a conclusion, this method could not be used only for rough evaluations of optical loss but for the detailed studies, a more accurate procedure is desirable.

Other techniques based on equations (2.3) and (2.4) have been proposed. They are all related to the modal optical gain, the material optical gain and the total loss in the laser. From (2.3), it is clear that the modal optical gain equals the total loss (with opposite sign) if the material optical gain is zero. This condition holds to good approximation for the energies below the bandgap energy and holds rigorously the transparency energy (at the transition point between absorption and gain). Thus, finding the modal gain at these points provide the value of the total loss, which provides the internal loss if the mirror loss is known.

A technique based on below-bandgap measurements is made difficult by the low intensity of the ASE spectrum in this region. This limits the accuracy of the gain measurements. For the section spectra shown in figure 2.1(b) the accuracy is no better than  $2\text{-}5\text{ cm}^{-1}$ . Below bandgap loss measurements are this adequate for rough estimates of loss but become unacceptable for more demanding purposed.

Another method to measure internal loss is to determine transparency at a given current so as to find the intersection of the gain curves in TE and TM polarizations under the assumption that the optical gain is the same and does not depend on the polarization when the material gain is zero. Figure 2.3 shows the curves of TE- and TM-polarized-gain measured for a typical MQW lasers. There is one intersection point at high energy (short wavelength) as well as an indication that the two curves will converge at below-bandgap energies as the material optical

gain tends towards zero. The possible source of error with this method is the assumption that the total optical loss is equal in the TE and TM polarizations. This may lead to an error which is in this case of about  $2 \text{ cm}^{-1}$ .

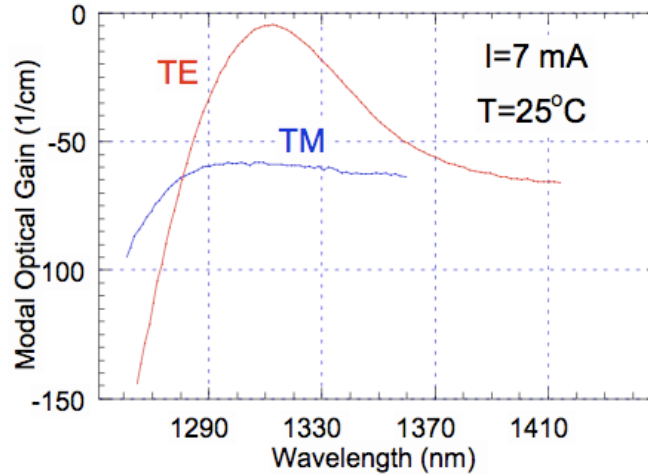


Figure 2.3: Modal optical gain extracted from ASE spectra of a MQW laser in TE and TM polarizations

## 2.3 Measurement of the Carrier Leakage in Semiconductor Lasers

Performance of semiconductor lasers depends on heterostructure injection efficiency namely on the fraction of injected carriers consumed by the active region. One of the mechanisms allowing carriers to recombine outside of the active layer is related to the thermoionic emission of electrons from the active layer to the p-cladding (heterobarrier leakage). Another mechanism of carrier escaping from active region prior their recombination is lateral transport of carriers through the blocking structure or the effect of carrier spreading in broad area lasers. Carrier leakage can affect the laser slope efficiency resulting in its reduction with increase in current and temperature and can also contribute to the temperature dependence of the threshold current.

### 2.3.1 Optical Technique of Studying the Carrier Leakage

The obvious method of studying the efficiency of carrier leakage under different conditions is to register the light resulting from recombination of carriers outside the active region. For instance, electroluminescence image of an InGaAsP/InP laser at 100 mA forward bias is shown

in figure 2.4(a) for a leaky laser and in figure 2.4(b) for a device with low leakage. Boxes approximately define the position of the active layer. The detected radiation is InP band to band recombination  $\lambda=0.97 \mu\text{m}$ . Low and high acceptor levels in their p-InP cladding layers characterize these high and low leakage devices respectively. From a general point of

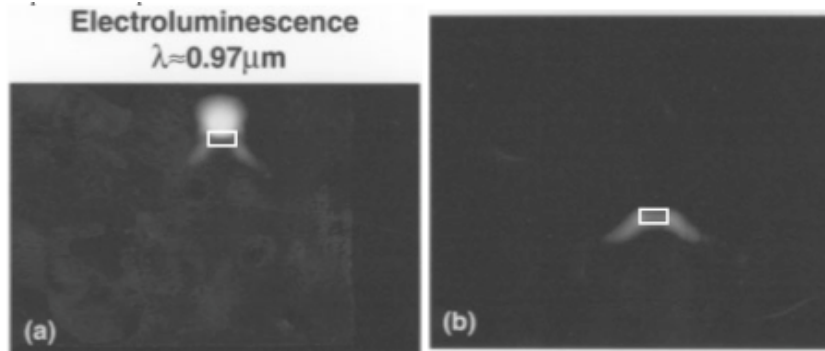


Figure 2.4: Electroluminescence images at 100 mA forward bias: (a) leaky laser and (b) very low leakage laser.

view, experimental results have shown that significant electron leakage can occur in double heterostructures constituting one of the mechanisms of sub-linearity of the light-current characteristics and also of the temperature dependence of the threshold current in laser diodes. Laser structures with low carrier overflow into barriers and SCH (separate confinement area) layer exhibit better high-temperature performance. Experiments show that higher values of compressive strain would have to be applied in order to reduce the carrier overflow into the barriers and into SCH region.

### 2.3.2 Electrical Technique of Studying Carrier Leakage

Figure 2.5 shows the device used to measure the leakage current in a  $1.3 \mu\text{m}$  InGaAsP/InP laser with a bulk active region. The emitter-base junction functions as an ordinary laser diode. The collector-base junction is reverse biased, as in a bipolar transistor, to collect the leakage current. An extra  $\text{N}^+$ -InP layer is added in order to collect the heterobarrier electron leakage current. Under forward bias condition, the emitter-base junction acts as a laser diode. The electrons are injected from the InP emitter into the quaternary region. In this structure, the electrons that overcome the heterobarrier and arrive at the base-collector junction are swept out by the electrical field in the reverse biased junction.

As an example, the typical dependence of the leakage current on injection current for the  $1.3 \mu\text{m}$  InGaAsP/InP broad area laser with moderately doped -p-cladding/SCH interface at different operation temperatures is shown in figure 2.6.

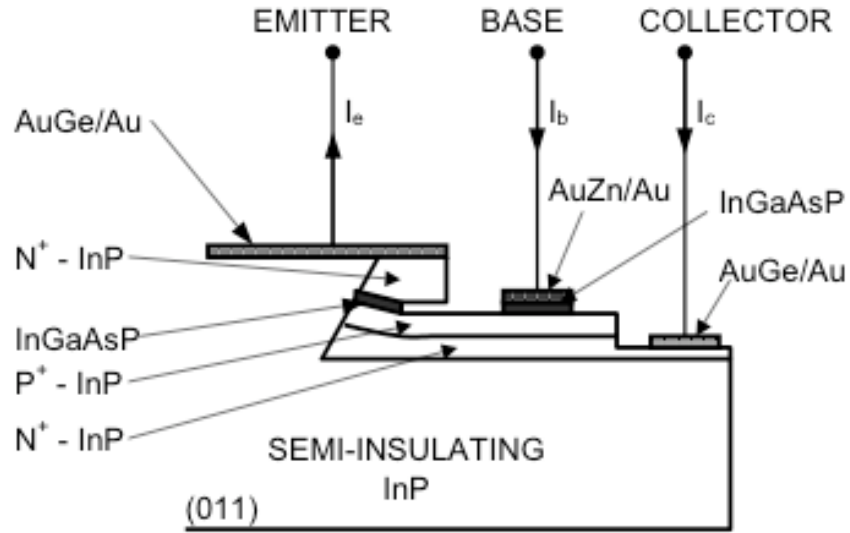


Figure 2.5: Schematic representation of the laser-bipolar transistor structure

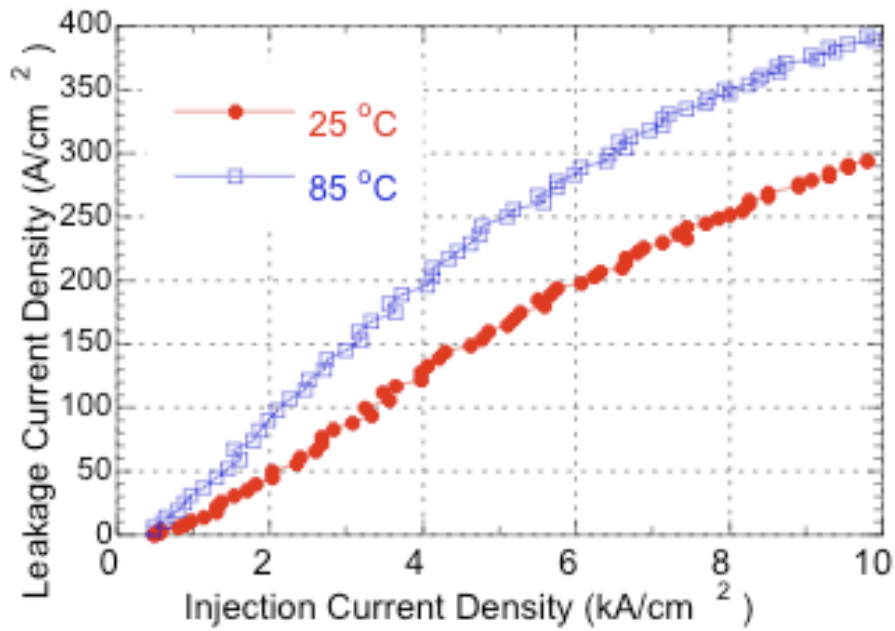


Figure 2.6: Measured heterobarrier leakage current versus injection current for an 1.3  $\mu\text{m}$  InGaAsP/InP broad area laser

## 2.4 Electrical and Optical Measurements of RF Modulation Response below Threshold

Most of the experimental methods aim at determining the carrier concentration which are based on a model using the balance equations of carriers and photons in the laser. These equations also named rate equations can be derived from Maxwell's equations and are as follows:

$$\frac{dN}{dt} = \eta_{int} \frac{I}{eV_{act}} - R - \frac{c}{n_{eff}} \frac{dG}{dN} (N - N_t) S \quad (2.14)$$

$$\frac{dS}{dt} = \frac{c}{n_{eff}} \Gamma \frac{dG}{dN} (N - N_t) S - \frac{S}{\tau_p} - \beta \Gamma R_{sp} \quad (2.15)$$

where  $N$  and  $S$  are the carrier and photon concentrations respectively,  $I$  is the pumping current,  $e$  is the electron charge,  $R$  the total recombination rate (without the stimulated emission),  $R_{sp}$  the spontaneous emission rate,  $c$  the light velocity in vacuum,  $n_{eff}$  the effective refractive index,  $G$  the material optical gain in the active layer,  $\Gamma$  the optical confinement factor and  $\tau_p$  the photon lifetime. Internal efficiency  $\eta_{int}$  accounts for an imperfect current injection efficiency into the active layer. The term  $(1 + \epsilon_S S)$  describes the gain saturation with photon density,  $\epsilon_S$  being the phenomenological gain compression parameter (related to the photon density). It was originally introduced to characterize the spectral hole burning. In general this parameter may be used to describe the reduction of the optical gain (linear approximation) above threshold due to any process, such as spatial hole burning, carrier heating, ... Since the rate equations treat the laser as a medium with single spectral and spatial mode, only the value of the gain at the lasing wavelength is important. Therefore, the wavelength-independent parameter  $\epsilon_S$  can be used. However, the use of this parameter is not valid when considering the effects that involve gain spectra, since different effects distort the gain spectra differently and non-uniformly.

The first equation describes the balance of the carrier plasma. The carriers are injected by the injection current (first term), and then recombine spontaneously or non radiatively (second term), as well as through stimulated emission of radiation (last term). The second equation describes the balance of photons inside the laser cavity. In this set of equations, two important processes are ignored: carrier transport through the SCH and the active layer and carrier capture into quantum wells (in case of QW lasers).

The stimulated emission term in the first equation can be neglected below threshold. Then, expressing the recombination in terms of the carrier concentration and carrier lifetime  $\tau_s$ :

$$\frac{dN}{dt} = \eta_{int} \frac{I}{eV_{act}} - \frac{N}{\tau_s} \quad (2.16)$$

In case of small-signal analysis (small-signal pulse or sinusoidal), the previous equation can be modified such as:

$$\frac{d\delta N}{dt} = \eta_{int} \frac{\delta I}{eV_{act}} - \frac{\delta N}{\tau_s} \quad (2.17)$$

The total number of carriers can be found by integrating the differential carrier lifetime over the bias current:

$$N(I) = \eta_{int} \int_0^I \tau_s(I') dI' \quad (2.18)$$

Various techniques, based on the relations (2.16), (2.17) and (2.18) have been used to measure the carrier concentration and the recombination rates in semiconductor lasers. Especially, the carrier lifetime value and its dependence on the current characterize various recombination mechanisms in the active layer of semiconductor lasers. The major mechanism is the spontaneous radiative recombination, a standard bimolecular recombination. Non-radiative processes such as trap or interface and Auger recombination have also been addressed.

### 2.4.1 Determination of the Carrier Lifetime from the Device Impedance

The equivalent circuit of a semiconductor laser in the small-signal modulation regime below threshold is depicted in figure 2.7. It can be derived from the rate equation. The active layer is represented as a RC circuit with characteristic time equal to the differential carrier lifetime. Taking into account a series resistance  $R_s$ , introduced by the contacts and cladding layers,

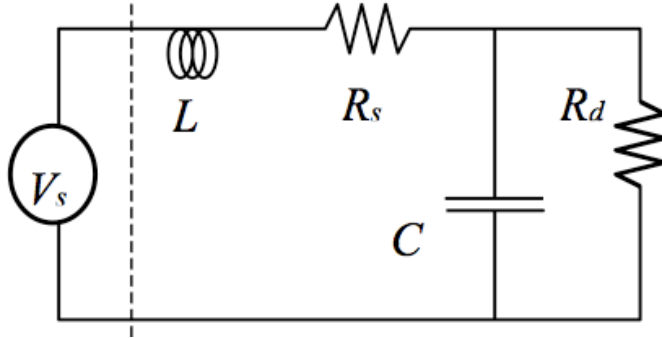


Figure 2.7: Simple equivalent circuit of a laser diode below threshold

and a bonding wire inductance  $L$ , the impedance of the equivalent circuit can be written such as:

$$Z(j\omega) = j\omega L + R_s + \frac{R_d}{1 + j\omega\tau_d} \quad (2.19)$$

where  $\tau_d = R_d C$  and  $R_d$  is the static differential resistance of the pn junction. This model does not take into account the leakage paths and a blocking structure capacitance. It also considers that transport and capture-escape times are much faster than the differential carrier lifetime and may be neglected. Equation (2.19) shows that the laser impedance below threshold is frequency-dependent and that the differential carrier lifetime can be extracted directly

from electrical measurements of the laser impedance. The laser impedance as function of frequency can be measured using a network analyzer. The real and imaginary parts of the laser impedance are described by:

$$\text{Re}(Z(\omega)) = R_s + \frac{R_d}{1 + (\omega\tau_d)^2} \quad (2.20)$$

$$\text{Im}(Z(\omega)) = \omega L + \frac{R_d}{1 + (\omega\tau_d)^2} \quad (2.21)$$

Figure 2.8 shows the real (a) and imaginary (b) parts of the impedance of laser with bulk active layer at room temperature an current of 1 mA. The solid line are fits to equations (2.20) and (2.21) with the parameter shown. Fitting the real and imaginary parts of the laser impedance gives very close values for all model parameters. This measurement technique is

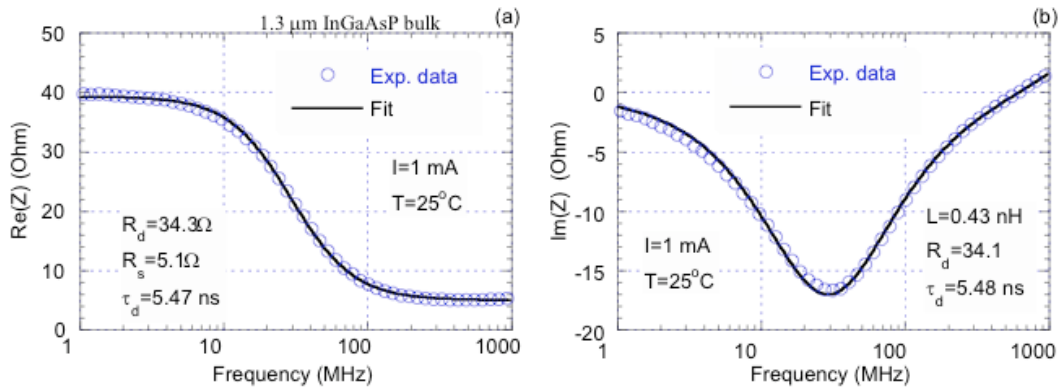


Figure 2.8: Measured real (a) and imaginary (b) parts of the laser diode impedance (circles) and fits to equations (2.20) and (2.21) (solid lines)

based on a simple purely electrical measurement. It is useful when optical detection is difficult which is the case at low currents and in the wavelength ranges where no fast detectors are available. Also, this method is not accurate at high currents, where the value of the differential resistance  $R_d$  gets smaller. This model in general is correct as long as the transport effects including the capture-escape process can be neglected. In the case of highly doped MQW lasers, this model is not accurately correct and a more complicated model is required.

Another point to be stressed is that the laser diode may have a parasitic capacitance formed by the contact pads, blocking layers,... In figure 2.7, such a capacitance is connected in parallel with the laser pn junction capacitance. Despite it is usually small compared to the junction capacitance, the latter one decreasing as the current through the laser decreases, the junction capacitance may become comparable to the parasitic one for certain values of current.

### 2.4.2 Determination of the Carrier Lifetime from the Optical Response Measurements

This technique for determining the differential carrier lifetime proposes to use a small-signal current step excitation. The optical response curve was fitted to an exponential form based on (2.17). This technique has the disadvantage of high noise if the excitation signal is small. A solution is to use a frequency domain analysis of (2.17) which leads to superior signal-to-noise ratio for the same levels of excitation. Under this assumption, (2.17) has a solution in the frequency domain:

$$d\delta N(\omega) = \frac{\delta I(\omega)}{eV_{act}} \frac{\tau_d}{1 + j\omega\tau_d} \quad (2.22)$$

where  $\omega=2\pi f$  is the modulation frequency and  $j$  the complex unit. Under small-signal modulation, the deviation of the photon concentration  $\delta S$  is proportional to the deviation of the carrier concentration  $\delta N$ . Originally, many authors used the previous equation considering that the current amplitude is frequency-independent. However, most of the commercially available signal generators are power sources, which in the experiment are loaded on the laser diode. This connection has an equivalent circuit of a voltage source loaded on an  $r$  resistor plus a laser impedance  $Z(j\omega)$ . The frequency dependence of the impedance results in the frequency dependence of the amplitude of the current modulation, therefore it should be taken into account in order to correctly extract the value of the differential carrier lifetime. As a consequence (2.22) can be re-written as follows:

$$d\delta N(\omega) = \frac{1}{eV_{act}} \frac{\delta V}{r + Z(j\omega)} \frac{\tau_d}{1 + j\omega\tau_d} \quad (2.23)$$

The voltage modulation amplitude  $dV(\omega)$  can be considered constant over the frequency range. Thus, the knowledge of  $Z(j\omega)$  can be used to correct the measured optical modulation in order to use the single-pole fitting procedure. Using (2.23), one can write:

$$F(\omega) = |\delta S(\omega)| |r + Z(\omega)| \propto \frac{1}{\sqrt{1 + (\omega\tau_d)^2}} \quad (2.24)$$

where the corrected function  $F(\omega)$  can be used to extract the differential carrier lifetime. The measured optical response curve are shown in figure 2.9 (circles) and was corrected using (2.24) (squares) and then fit to a single pole roll-off form from which the differential carrier lifetime can be extracted.

**Note:** The simplified model of the laser impedance can be used for correction of the differential lifetime data obtained from optical response measurements suiting the values of  $R_d$  and  $R_s$  obtained from either static or dynamic measurements. By substituting equation (2.19)

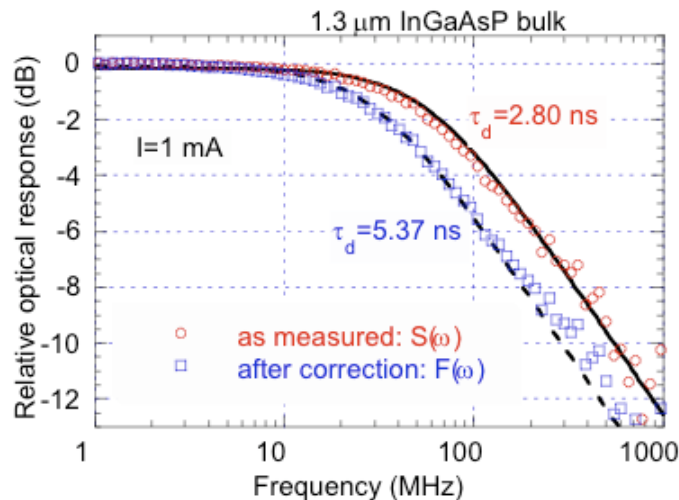


Figure 2.9: Optical response curves as measured (circles) and corrected using (2.24) (squares). Lines are single pole fits.

into equation (2.22), a corrected differential carrier lifetime can be obtained:

$$\tau_{d,corr} = \tau_{d,opt} \left( 1 + \frac{R_d}{R_s + r} \right) \quad (2.25)$$

in which the corrected lifetime is larger than the uncorrected. The use of this simple correction gives the same value of the differential carrier lifetime as the technique based on impedance analysis and impedance corrected optical measurement.

## 2.5 Optical Measurements of RF Modulation Response and RIN above threshold

Small-signal response measurement is a very powerful technique that allows analyzing a number of important device parameters, such as the differential gain and gain suppression coefficient. They are also very useful in estimating the device performance in the real operating conditions, such as digital current modulation. Rate equations given by equations (2.14) and (2.15) can be solved for large signal analysis. Also, simple small-signal analysis allows for determination of some fundamental characteristics of the laser. Under this assumption, small sinusoidal current modulation around the static value results in sinusoidal modulation of the carrier concentration and photon density:

$$I(t) = I_0 + I_1 e^{j\omega t} \quad (2.26)$$

$$N(t) = N_0 + N_1 e^{j\omega t} \quad (2.27)$$

$$S(t) = S_0 + S_1 e^{j\omega t} \quad (2.28)$$

It can be demonstrated that the solution for optical power can be expressed such as:

$$\frac{P(\omega)}{I(\omega)} = \frac{h\nu}{q} \eta H(\omega) \quad (2.29)$$

where the two-parameter modulation transfer function  $H(\omega)$  is defined as follows:

$$H(\omega) = \frac{\omega_R^2}{\omega_R^2 - \omega^2 + j\omega\gamma} \quad (2.30)$$

The two-parameters in (2.30) are the electron-photon resonance frequency  $\omega_R$  and the damping factor  $\gamma$ . Expressions for these values can be expressed as:

$$\omega_R \approx \sqrt{\frac{\frac{c}{n_{eff}} \frac{dG}{dN} S_0}{\tau_p (1 + \epsilon_S S_0)}} \quad (2.31)$$

$$\gamma = \frac{1}{\tau_s} + \frac{c}{n_{eff}} \frac{dG}{dN} \frac{S_0}{1 + \epsilon_S S_0} + \frac{1}{\tau_p} \frac{\epsilon_S S_0}{1 + \epsilon_S S_0} \quad (2.32)$$

where photon lifetime  $\tau_p$  is proportional to the optical loss,

$$\frac{1}{\tau_p} = \frac{c}{n_{eff}} (\alpha_m + \alpha_i) \quad (2.33)$$

Figure 2.10 shows the amplitude (a) and the phase (b) of the laser optical modulation response at different DC biases, measured using a network analyzer with a high-speed pin detector. The response curves show typical resonant behavior described by equation (2.30). Additional drooping of the response curves, seen in figure 2.10(a) has been attributed to carrier transport through the SCH layers and the carrier capture and thermoionic emission processes in QW lasers. As it can be seen from (2.31) and (2.32), the resonance frequency and the damping factor contain important factor on the material parameters: differential gain and the gain compression factor. If these values were known as functions of the injection current (or optical power), the above parameters could be determined. The damping factor  $\gamma$  increases proportionally to the square of the resonance frequency following the relationship:

$$\gamma = K f_R^2 + \gamma_0 \quad (2.34)$$

with  $\gamma_0$  the carrier lifetime and  $K$  the  $K$ -factor which can be expressed as follows:

$$K \approx 4\pi^2 \left( \tau_p + \frac{\epsilon_S}{\frac{c}{n_{eff}} \frac{dG}{dN}} \right) \quad (2.35)$$

The resonant frequency increases with current and so does the small-signal modulation bandwidth (the frequency at which the response amplitude drops down by 3-dB from its DC value),

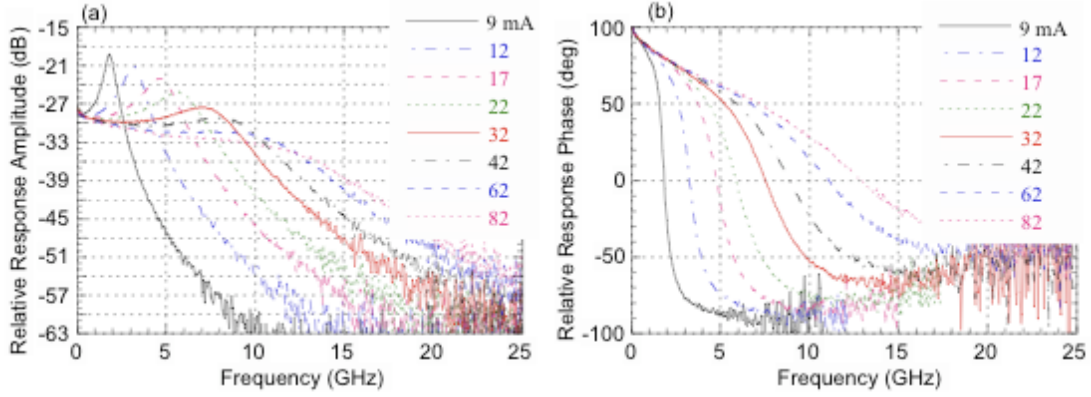


Figure 2.10: Amplitude (a) and Phase (b) of the laser response to small-signal direct current modulation

but only up to a certain level. As the DC injection current increases, the response flattens as depicted in figure 2.10(a). At some point, the damping factor becomes large enough so that the modulation response amplitude drops by 3-dB at the frequency below  $\omega_R$ . It was shown that maximum possible bandwidth is roughly given by,

$$f_{3dBmax} \approx \sqrt{2} \frac{2\pi}{K} \quad (2.36)$$

**Note:** The knowledge of the dependence of the resonant frequency on current allows determining the differential gain in the material of the active layer. Thus, based on (2.30), it comes:

$$\frac{dG}{dN} \approx \frac{4\pi^2 f_R^2 \tau_p}{\frac{c}{n_{eff}} S_0} = \frac{4\pi^2 eV}{\frac{c}{n_{eff}} \Gamma \eta_i} \left( \frac{f_R^2}{I - I_{th}} \right) \quad (2.37)$$

where  $I_{th}$  is the threshold current and the relation between the photon density and the output power is such that,

$$S_0 \approx \frac{\Gamma P_{out}}{V h\nu} \left( \frac{c}{n_{eff}} \alpha_m \right)^{-1} = \frac{\Gamma \eta_i}{V e} \tau_p (I - I_{th}) \quad (2.38)$$

where the mirror loss  $\alpha_m$  is given by the first term of (2.4). In the current treatment the effects of the carrier transport and capture into the QW are ignored. More accurate phenomenological treatment yields another factor  $\chi$  in the right side of (2.37) such that  $\chi = 1 + \frac{\tau_d}{\tau_e}$  with  $\tau_d$  the carrier capture time including diffusion across SCH and  $\tau_e$  the thermoionic emission lifetime. Differential gain was estimated from the data presented in figure (2.11). Ignoring the transport effects ( $\chi = 1$ ) and assuming the internal efficiency  $\eta_i$  we find  $\frac{dG}{dN} \approx 4.1 \cdot 10^{-16} \text{ cm}^2$ .

**Note:** The differential gain and the gain saturation parameters can be determined from the

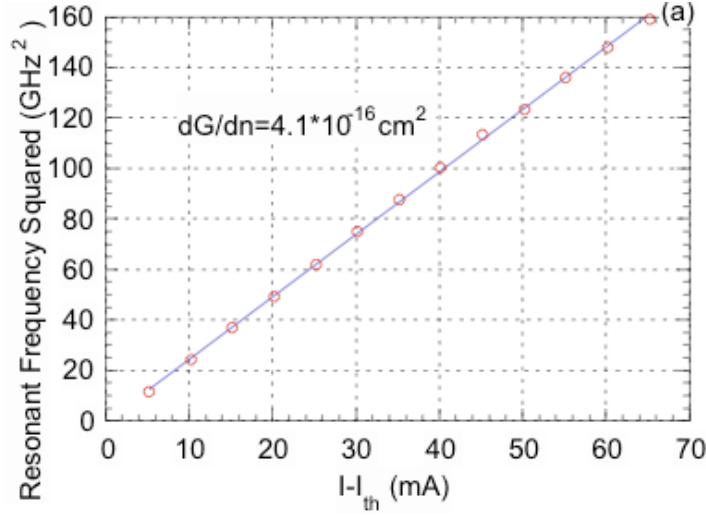


Figure 2.11: The resonant frequency squared as a function of the current deviation above laser's threshold

dependencies of the resonance frequency and damping factor on the optical power (DC drive current) using (2.31) and (2.32). Despite these dependencies can be both extracted from the modulation response, an accurate procedure is not trivial. As shown in figure 2.10(a), the amplitude response curves cannot be directly fit to (2.29) since there is an additional factor to consider in the transfer function. This additional contribution is associated with the carrier transport; also the response characteristics of the laser can be further distorted by RLC parasitic elements in the electrical feed circuit. Thus, the response function in (2.29) should be written as follows:

$$\frac{P(\omega)}{I(\omega)} = \frac{h\nu}{q} \eta H(\omega, \omega_R, \gamma) T(\omega) \quad (2.39)$$

where  $T(\omega)$  is a composite transfer function which cannot be written analytically in the general case.

### 2.5.1 Determination of the Resonant Frequency and Differential Gain from the RIN Measurements

Relative intensity noise (RIN) measurements represent the alternative technique used for studies of high-speed dynamics in QW lasers. Like modulation response technique described previously, this approach allows for determining the differential gain and  $K$ -factor through numerical fitting procedure. However it is important to stress that the signal measured is not the response to the external modulation of the bias current but the noise spectra of the laser itself. This noise power is associated with the fluctuation of the concentrations in photon and

electron systems caused by spontaneous emission light events. Deviation of the electron and photon densities from equilibrium values lead to their damped oscillations with the frequency of electron-photon resonance  $f_R$  and damping factor  $\gamma$ .

RIN is defined as the mean square value of the noise power related to the mean value of the output power squared:

$$RIN = \frac{\langle \delta P(t)^2 \rangle}{P_0^2} \quad (2.40)$$

**Note:** It is more convenient to define the RIN per unit bandwidth because the measurement bandwidth can vary under different experimental conditions.

$$\frac{RIN}{\Delta f} = \frac{2S_{\delta P}(\omega)}{P_0^2} \quad (2.41)$$

where  $S_{\delta P}(\omega)$  is double sided noise power spectral density (if the spectral density is defined as single-sided, the factor 2 should be removed). As defined, the RIN is measured in dB/Hz.

Small signal analysis applied to the rate equations but taking into account internal noise source and transport of carriers leads to the following expression for the spectral dependence of the RIN:

$$RIN = \frac{4}{\pi} \delta f \frac{f^2 + (\gamma^*/2\pi)}{(f_R^2 - f^2)^2 + f^2(\gamma/2\pi)^2} \quad (2.42)$$

where  $\delta f$  is the Schawlow-Townes linewidth and  $\gamma^*$  differs from  $\gamma$  in the denominator due to carrier transport through the active region. Figure 2.12 shows the RIN spectra for a 1.3  $\mu\text{m}$

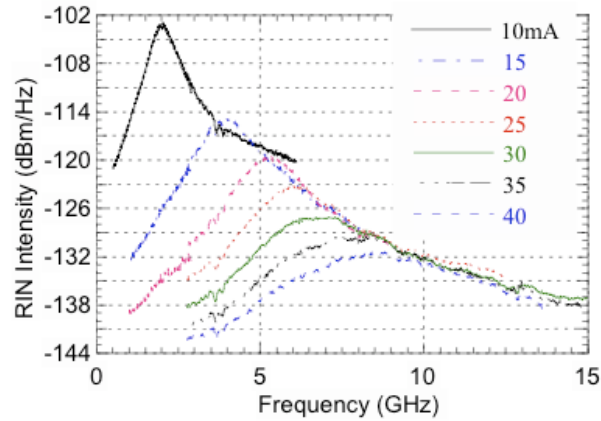


Figure 2.12: The RIN spectra for a 1.3  $\mu\text{m}$  InGaAsP/InP MQW laser at the different bias condition

InGaAsP/InP MQW laser at the different bias condition. The resonance frequency, damping factor and Shawlow-Townes linewidth can be determined from fitting the experimental spectra with (2.42). Taking into account the carrier transport properties of the structure, the dependence of the resonance frequency on current can be determined. Figure 2.13 shows the experimental results for the same laser as in figure 2.11. The values of the differential gain  $\frac{dG}{dN}$  and of the  $K$ -factor are also mentioned. The main advantage of the RIN technique by comparison with the modulation response one is the elimination of the problem with high frequency modulation experimental equipment. Also to be noted is the absence of low-frequency roll-off in the RIN spectra, which is related to the carrier capture and diffusion across SCH.

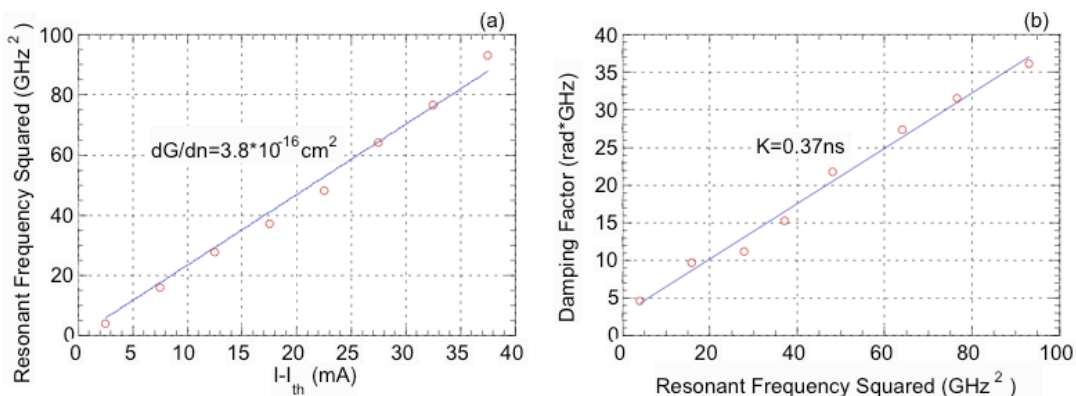


Figure 2.13: Determination of the differential gain (a) and  $K$ -factor (b) from the slopes of the theoretically predicted linear dependencies

## 2.6 Measurements of the linewidth enhancement factor

The linewidth enhancement factor (LEF), also known as  $\alpha_H$ -factor, has a great importance for semiconductor lasers, as it is one of the main features that distinguishes the behavior of laser diodes with respect to other types of lasers. The  $\alpha_H$ -factor influences several fundamental aspects of laser diodes, such as the linewidth, the chirp under current modulation, the mode stability, the occurrence of filamentation in broad-area devices. In synthesis, the dynamics of laser diodes is greatly influenced by the  $\alpha_H$ -factor, which is of particular interest for the study of injection phenomena, optical feedback effects, and mode coupling as occurring in VCSELs. The birth of the  $\alpha_H$ -factor traces back to the early 80s, when first measurements revealed that the semiconductor laser linewidth was much broader than what predicted by the Shawlow-Townes theory. A theoretical explanation soon came from Henry, who developed a theory that ascribes the excess linewidth to the joint action of spontaneous emission events and population inversion (i.e. carrier) relaxation, through the mechanism of

index-gain coupling. The latter represents the fact that in a semiconductor medium both the optical gain and the refractive index depend on the actual carrier density. Since then, a number of theoretical and experimental works were carried out, with the aim of calculating the dependence of the  $\alpha_H$ -factor on laser diode material parameters, and measuring its value in practical devices.

### 2.6.1 Definition

The  $\alpha_H$ -factor is defined as the ratio of the partial derivatives of the real and complex parts of the complex susceptibility  $\chi = \chi_r + j\chi_i$  with respect to carrier density  $N$ :

$$\alpha_{H,T} = -\frac{\partial\chi_r/\partial N}{\partial\chi_i/\partial N} = \frac{\left(\frac{\partial n'}{\partial N}\right)_T}{\left(\frac{\partial n''}{\partial N}\right)_T} = -\frac{4\pi}{\lambda} \frac{dn/dN}{dg/dN} \quad (2.43)$$

where  $dn$  and  $dg$  are the small index and optical gain variations that occur for a carrier density variation  $dN$ . According to the definition, theoretical models describing the optical properties of the semiconductor medium were used to numerically evaluate the  $\alpha_H$ -factor by calculating the differential gain and differential refractive index. More accurate models also take into account the effect of free carriers. In a linear approximation, only one among the spectral dependence of the differential gain and differential refractive index shall be calculated, as the other can be obtained through Kramers-Kronig transformations. Estimated/measured values for  $\alpha_H$ -factor lie in the range 0.5-8.0, with more common values in the range 2.0-6.0. Typically,  $\alpha_H$ -factor increases for decreasing photon energy and for increasing carrier density. The analysis of different material reveals that, generally, the  $\alpha_H$ -factor is smaller in MQW than in bulk, and it is even further reduced in strained materials, Quantum Wires and Quantum Dots. Also, novel materials such as InGaNAs/GaAs are very promising for having  $\alpha_H$ -factor values around unity. Some authors suggested that non-linear gain and/or carrier heating should have a non negligible effect on  $\alpha_H$ -factor which in turn should be considered as an optical power dependent parameter (the effective  $\alpha_H$ -factor should increase with increasing power). Some authors also attribute the effect of high power linewidth floor/rebroadening to the power dependence of  $\alpha_H$ -factor, while others suggested different mechanisms. As a matter of fact, at present no clear experimental and systematic evidence of the power dependence of the  $\alpha_H$ -factor has been reported.

**Note:** Besides the instantaneous phase change caused by spontaneous emission, there will be a delayed phase change resulting from the instantaneous change in the field intensity. To restore the steady-state field intensity, the laser will undergo relaxation oscillations. During

this time, the net gain changes  $\Delta g(t) = -(2\omega/c)\Delta n''(t)$  where  $\Delta n''$  is the deviation of the imaginary part of the refractive index from its steady-state value. The change in  $n''$  is caused by the modification of the carrier density which also alters the real part  $n'$  of the refractive index. The ratio of this change does correspond to the definition of the linewidth enhancement factor  $\alpha_H = \Delta n'/\Delta n''$ . A change in  $\Delta n'$  during a limited period of time results in an additional phase-shift of the laser's field and in an additional linewidth broadening. Let us consider a monochromatic wave propagating towards the  $z$  direction:

$$E(\omega, z) = E_0 e^{j(\omega t - kz)} \quad (2.44)$$

with  $k = \omega n/c = \omega/c(n' + jn'') = k_0(n' + jn'')$  the propagation constant. Then injecting into (4.44) it comes,

$$E(\omega, z) = E_0 e^{j(\omega t - k_0 n' z)} e^{k_0 n'' z} \quad (2.45)$$

This relation demonstrates that the real part of the refractive index acts on the electric field's phase while the real part influences the amplitude. The loss coefficient defined in intensity can be written such as:

$$\alpha = -2k_0 n'' \quad (2.46)$$

The power is  $z$ -dependent and decays exponentially following the well-known relationship  $P(z) = P(0)e^{-\alpha z}$ . In case of a laser diode the net gain  $g - \alpha$  should be used instead:

$$g - \alpha = -2k_0 n'' \quad (2.47)$$

If  $g = \alpha$ , the relative dielectric permittivity is purely real such as  $\epsilon_r = n^2$ . If  $g > \alpha$ , situation gets different because of the coupling between the refractive index and the carrier density. Thus, considering that the contribution of the imaginary part remains small one can write:

$$\epsilon_r = (n' + jn'')^2 = n'^2 - n''^2 + 2jn'n'' \approx n'^2 + 2jn'n'' \quad (2.48)$$

The changes in carrier density will cause  $n'$  and  $n''$  to deviate from their threshold values such as  $n' = n'_0 + \Delta n'$  and  $n'' = n''_0 + \Delta n''$ . Neglecting the crossing terms and still considering that the contribution of the imaginary part is negligible, one obtains:

$$\epsilon_r = n_0'^2 + 2n_0'(\Delta n' + j\Delta n'') = n_0'^2 + 2jn_0'\Delta n'' \left(1 - j\frac{\Delta n'}{\Delta n''}\right) = n_0'^2 + 2jn_0'\Delta n''(1 + j\alpha_H) \quad (2.49)$$

This last equation points out how occurs the linewidth enhancement factor  $\alpha_H = \Delta n'/\Delta n''$  in the relative dielectric permittivity when considering the laser's situation above the threshold.

## 2.6.2 Measurement Techniques of the $\alpha$ -factor

According to the above definition, measurements techniques can broadly be classified as:

- 1) techniques capable to measure the **material linewidth enhancement factor**;
- 2) methods capable to measure the **device linewidth enhancement factor**.

Methods of class 1 are based on sub-threshold gain/refractive index measurements, and their results might not be closely matched to the behavior of lasers in operating conditions. Conversely, class 2 methods perform the measurement above threshold, and can account for more complex effects. Throughout the scientific literature about linewidth enhancement factor, no systematic comparison of measurement results obtained from different methods on the same devices has been carried out. Only a few works report the comparison between two methods. It should be pointed out that not all methods are applicable to all types of laser diode devices. For example, the common Hakki-Paoli method cannot be applied to VCSELs for the absence of multiple longitudinal modes, and to date no method has been applied to measure the  $\alpha_H$ -factor in Quantum Cascade semiconductor lasers, and only a few reports are available about the  $\alpha_H$ -factor of external cavity semiconductor lasers. It follows here a brief review of different measurement methods for the linewidth enhancement factor proposed and demonstrated in the scientific literature. For each method advantages and drawbacks are listed, from the point of view of simplicity of the experimental arrangement and accuracy.

### ASE-gain spectrum + Fabry-Perot frequency shift (Hakki-Paoli)

This technique relies on direct measurement of  $dg$  and  $dn$  as the carrier density is varied by an unknown amount  $dN$  by slightly changing the current of a semiconductor laser in sub-threshold operation. The measurement is performed using a monochromator-based optical spectrum analyzer. The quantity  $dn$  is measured through detection of the frequency shift of longitudinal Fabry-Perot mode resonances, while  $dg$  is obtained via the Hakki-Paoli method by measuring the fringe contrast (Peak to valley ratio) of the amplified spontaneous emission filtered by the Fabry-Perot cavity. This method is the most common in investigations about  $\alpha_H$ -factor, it is of straightforward implementation, and it can be easily automated via computer-controlled procedure. Critical points concern the resolution of the spectrum analyzer for the case of closely spaced longitudinal modes, and the fact that the thermal peakshift drift occurring in CW measurements shall be subtracted to reveal the net carrier effect. This is a sub-threshold technique, and it only measures the material linewidth enhancement factor as a function of injected current and photon energy (while the exact carrier density must be

evaluated by other techniques). Hence, there is no chance to measure the possible dependence of  $\alpha_H$ -factor on optical power. It should be noted that this technique and the following one are the only that allow to measure  $\alpha_H$ -factor at different photon energies, because methods in which the laser is operated above threshold only give information about  $\alpha_H$ -factor at the lasing wavelength. This technique cannot be applied to VCSELs, because these devices have one single longitudinal mode beneath the useful gain bandwidth. It is also difficult to be applied to edge-emitting devices with AR-coated facets (such as some DFBs) due to reduced fringe contrast, and to complex-coupled DFBs. The accuracy of the method is generally good (see next paragraph).

### Gain spectrum + Kramers-Kronig

Another (typically sub-threshold) technique that measures the material linewidth enhancement factor as a function of photon energy and injected current is based on accurate gain spectral measurements as a function of the injected carrier density, from which the spectral differential gain can be obtained. Subsequently, Kramers-Kronig relations allow to retrieve the differential refractive index and the calculation of  $\alpha_H$ -factor. The gain spectrum is typically measured from sub-threshold pure spontaneous emission spectra, that must be collected without the effect of cavity amplified spontaneous emission. Hence, light cannot be collected from the output facet of edge-emitting devices, and windows opening must be purposely fabricated on the top or the side of devices. Otherwise, direct measurement of the differential gain can be obtained by ultrafast pump-probe techniques. This method is generally complex, as it involves some experimental difficulties and relevant post-processing of collected data. Its accuracy is moderate (see next paragraph).

### Linewidth

According to Henry theory, the  $\alpha_H$ -factor directly influences the linewidth of a semiconductor laser, and hence linewidth measurements could give information about  $\alpha_H$ -factor. The theoretical linewidth formula reads:

$$\Delta\nu = \frac{h\nu v_g g_{th} n_{sp} \alpha_m}{8\pi P} (1 + \alpha_H^2) + \Delta\nu_0 \quad (2.50)$$

where  $v_g$  is the group velocity,  $g_{th}$  is the threshold gain,  $n_{sp}$  is the spontaneous emission factor,  $\alpha_m$  is mirror loss,  $P$  is the output power per facet, and  $\Delta\nu_0$  is a power-independent linewidth term. In linewidth methods the semiconductor laser linewidth is typically measured as function of emitted power, and the slope of  $\Delta\nu$  versus inverse power is used to compute the linewidth enhancement factor using (2.50). Obviously, the accuracy of this method is greatly influenced by the degree of accuracy that affects the knowledge of other device parameter that appears in (2.50). In particular, difficult parameters are the spontaneous emission rate

and the internal loss. Knowledge of the above parameters usually requires a thorough characterization of the specific device under test, together with the knowledge of some fabrication parameters (such as facets reflectivities). Hence, this method is hardly applicable to commercial semiconductor lasers, or to "black box" devices. This technique has been often used to measure the  $\alpha_H$ -factor of VCSELs. The method is of general straightforward implementation, but its accuracy has to be regarded as poor, due to the above mentioned complex dependence of  $\Delta\nu$  on several parameters.

**FM/AM modulation** This method relies on high-frequency semiconductor laser current modulation which, according to theory, generates both amplitude (AM) and optical frequency (FM) modulation. The ratio of the FM over AM components gives a direct measurement of the linewidth enhancement factor. The AM term can be measured by direct detection via a high speed photodiode, while the FM term is related to sidebands intensity that can be measured using a high resolution Fabry-Perot filter. This technique allows the measurement of the device  $\alpha_H$ -factor, it can be applied to all types of semiconductor lasers, and it has been often deployed to characterize VCSELs. The modulation frequency  $f_m$  must be larger than the laser relaxation frequency  $f_r$ , because for  $f_m < f_r$  the FM/AM ratio is frequency-dependent. This fact poses some experimental difficulties for devices with high  $f_r$ , requiring very high-speed RF generators and instrumentation. This method is reliable in the hypothesis that the susceptibility is linear and the carrier density is longitudinally uniform, and apart from the above mentioned frequency dependence, has a good accuracy. A modified method is based on the measurement of the chirp of light pulses emitted under large signal modulation. This technique is useful for assessing the real performance of a semiconductor laser when application to practical telecommunication system is of importance. However, its accuracy for the determination of the  $\alpha_H$ -factor is only moderate.

A typical experimental setup used for the FM/AM measurement is depicted in figure 2.14. As stated above, the goal is to determine the characteristics of the frequency modulation (FM) induced by the current modulation in the laser cavity. The signal at the output is analyzed through a tunable Mach-Zhender (MZ) interferometer made with two fibered couplers. This interferometer has a free-spectral range (FSR) which is the inverse of the differential delay  $|T_2 - T_1|$  between the two arms,  $T_1$  and  $T_2$  being the propagation time (time delay) in the two arms respectively. A polarization controller is used to make sure that the two signals located at the input of the second coupler have parallel states. Figure 2.14 shows the power at the output of the interferometer as a function of the propagation time difference or of the optical frequency. In order to finely control the optical path difference, a cylindrical piezoelectric transducer is used. The transducer located onto of the MZ's arms is fiber interdependent and

directly controlled by an external locking circuit. The system allows to adjust the interferometer on all points of the characteristics. Measurements are done at two different points A

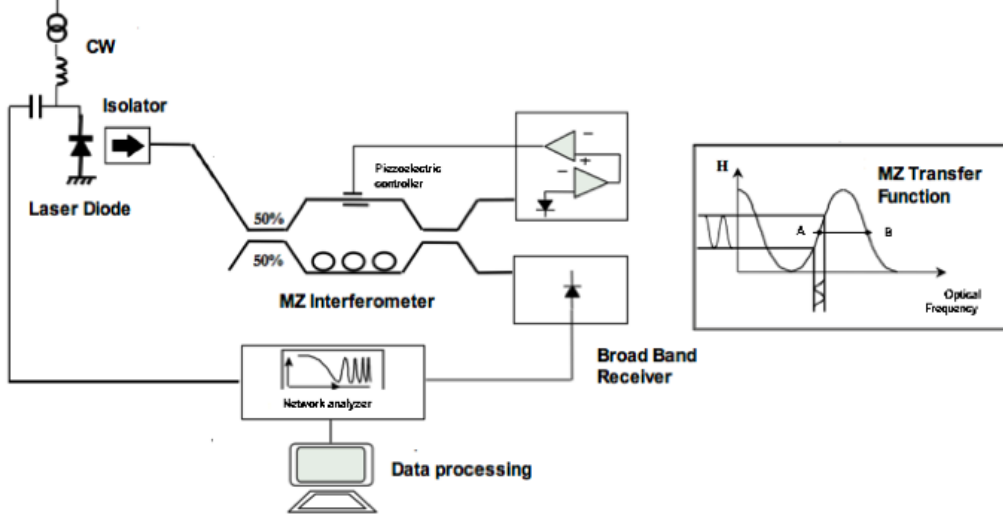


Figure 2.14: The experimental setup used for the determination of AM, FM responses and of the  $\alpha_H$ -factor

and B, which are in quadrature with each other as shown in the inset of the figure 2.14. Because of the linearity of the MZ interferometer in this region, the FM (or phase modulation (PM)) related to the signal to be analyzed generates an additional amplitude modulation (AM) proportional to the frequency deviation  $\Delta F$  across the carrier wave. The change of sign when switching from A to B allows to separate the AM and FM responses as a function of the modulation frequency  $f_m$  in the 10KHz to 20GHz range.

The signal from a laser under direct modulation can be expressed as follows:

$$e(t) = \sqrt{P_0} [1 + m \cos(2\pi f_m t)]^{1/2} \exp j [2\pi f_0 t + \beta \sin(2\pi f_m t + \phi)] \quad (2.51)$$

with  $P_0$  the average power,  $m$  the modulation rate in power ( $m = \Delta P/P_0$ ),  $f_m$  the frequency of the electrical signal provided by the network analyzer,  $f_0$  the central optical frequency,  $\beta$  the modulation rate in frequency such as  $\beta = \Delta F/f_m$  ( $\Delta F$  being the amplitude of the frequency modulation across the optical carrier  $f_0$ ) and  $\phi$  the phase difference between the modulation frequency and the amplitude frequency. As shown in figure 2.14, the network analyzer giving two results associated to the A and B operating points respectively, the normalized measured signals can be expressed as follows,

$$M_{\pm} = \frac{P_0}{2} m \cos\left(\frac{\pi f_m}{FSR}\right) \exp(-j2\pi f_m \tau) \pm P_0 \beta \sin\left(\frac{\pi f_m}{FSR}\right) \exp(-j2\pi f_m \tau + j\phi) \quad (2.52)$$

where  $M_+$  is the result in A and  $M_-$  in B respectively while  $\tau$  is the transit time within the interferometer. On one hand, the first term in (2.52) only depends on the amplitude modulation (i.e  $\beta$ -independent) while the term  $\cos\left(\frac{\pi f_m}{FSR}\right)$  corresponds to the AM transfer function of the interferometer. On the other hand, the second term in (2.52) is purely related to the modulation frequency ( $m$ -independent) and can be expressed as a function of the interferometer FM transfer function. From equation (2.52), following expressions can be deduced:

$$\frac{2\beta}{m} = \frac{1}{\tan\left(\frac{\pi f_m}{FSR}\right)} \left| \frac{M_+ - M_-}{M_+ + M_-} \right| \quad (2.53)$$

$$\phi = \arg\left(\frac{M_+ - M_-}{M_+ + M_-}\right) \quad (2.54)$$

Using the definitions of parameters  $m$  and  $\beta$ , equation (2.53) allows extracting the chirp power ratio (CPR) such as:

$$\frac{\Delta F}{\Delta P} = \frac{f_m}{2P_0} \frac{1}{\tan\left(\frac{\pi f_m}{FSR}\right)} \left| \frac{M_+ - M_-}{M_+ + M_-} \right| \quad (2.55)$$

The value of the  $\alpha_H$ -factor is then determined through the so-called relationship,

$$\frac{2\beta}{m} = \alpha_H \sqrt{1 + \left(\frac{f_c}{f_m}\right)^2} \quad (2.56)$$

In equation (2.54),  $f_c$  is defined as the corner frequency,

$$f_c = \frac{1}{2\pi} v_g \frac{\partial g}{\partial P} P \quad (2.57)$$

with  $v_g$  the group velocity,  $P$  the output power and is a nonzero parameter because of the phenomenon of nonlinear gain related to nonzero intraband relaxation times as well as carrier heating. Parameter  $\partial g/\partial P$  can be expanded as a function of the gain compression factor following the relationship,

$$\frac{\partial g}{\partial P} = \frac{\epsilon_P g}{1 + \epsilon_P P} \quad (2.58)$$

For typical numbers the corner frequency can be in the hundreds of MHz to few GHz range depending on the output power level. On one hand, for modulation frequencies such as  $f_m \gg f_c$  which is the case in the experiment since the maximum modulation frequency  $f_m$  is about 20 GHz range, the factor  $2\beta/m$  directly equals to the laser's linewidth enhancement factor. On the other hand, for lower modulation frequencies, the ratio  $2\beta/m$  becomes inversely proportional to the modulation frequency. Let us note that the measurement of  $2\beta/m$  with frequency and at different output power levels could serve for the determination of the corner frequency and consequently the gain compression factor. Figure 2.15 shows the ratio FM/AM in amplitude (red) and in phase (blue) as a function of the frequency

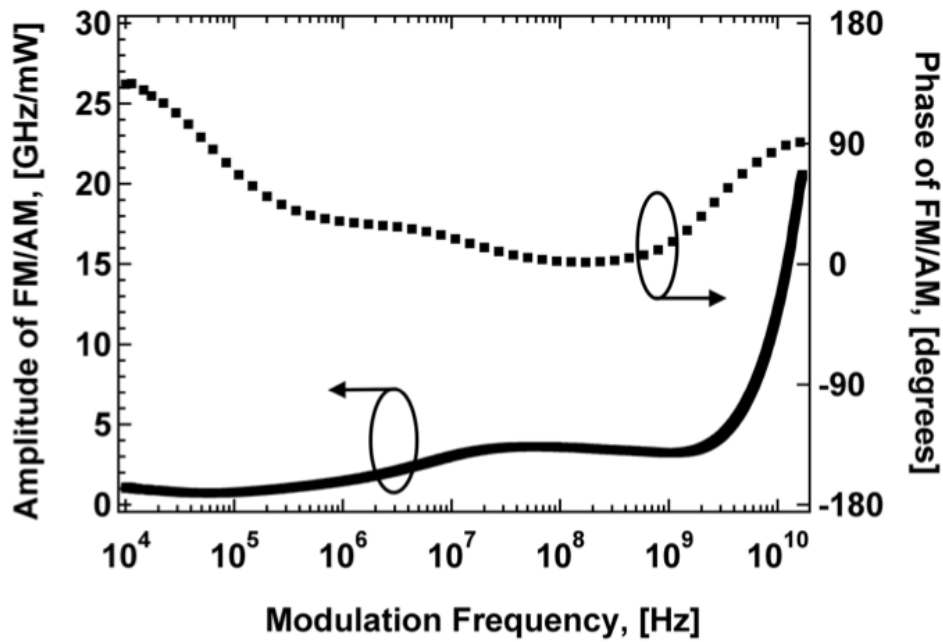


Figure 2.15: Amplitude and Phase of the FM/AM ratio as a function of the modulation frequency for the QW DFB laser

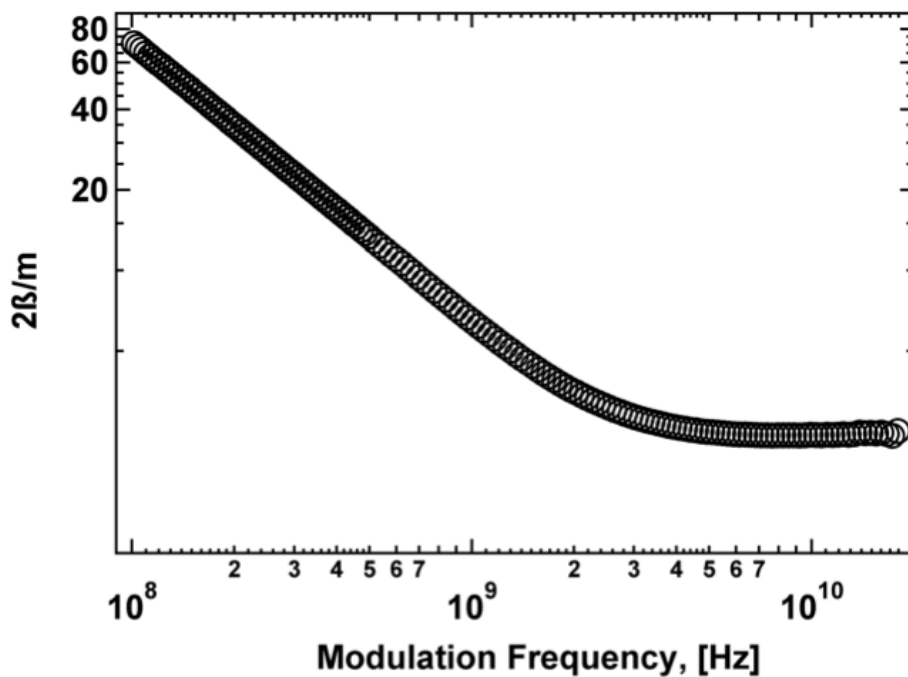


Figure 2.16: Ratio  $2\beta/m$  as a function of the modulation frequency for the QW DFB laser

modulation for a quantum well DFB laser emitting at 1550 nm. At low frequencies ( $f_m < 10$  MHz), thermal effects are predominant. The phase between FM and AM reaches  $180^\circ$  when the modulation frequency keeps decreasing below 10kHz. When  $10 \text{ MHz} < f_m < 1 \text{ GHz}$ , AM and FM modulations are in-phase (adiabatic regime) and thermal effects are no longer significant. Then, when  $f_m > 1\text{GHz}$ , relaxation oscillation between the carrier and photon numbers occur leading to a phase difference of  $90^\circ$ . From the calculations the ratio  $2\beta/m$  (with  $\beta$  the frequency modulation rate defined as  $\Delta F/f_m$  and  $m$  the amplitude modulation rate) can be plotted as a function of the frequency modulation. As shown in figure 2.16 the function  $2\beta/m$  asymptotically tends to the  $\alpha_H$  - factor. In the figure 2.16, considering  $f_m > 10\text{GHz}$ , the phase of the ratio FM/AM being close to  $90^\circ$ , the sign of the  $\alpha_H$ -factor is positive (a negative phase of  $-90^\circ$  would mean a negative value of the  $\alpha_H$ -factor).

### Injection Locking

Injection of light from a master semiconductor laser into a slave semiconductor laser causes locking of the slave optical oscillation frequency to that of the master. Typically, the locking region is characterized in terms of the injection level and frequency detuning, showing an asymmetry in frequency due to the non-zero  $\alpha_H$ -factor. Several methods have been presented for the measurement of the  $\alpha_H$ -factor based on injection locking experiments. These methods are capable of giving the effective value for  $\alpha_H$ -factor in operating conditions, and are based on the complex theory of injection locking dynamics, that can however be simplified to give the analytic dependence of measurable quantities (such as asymmetric detuning range) on  $\alpha_H$ -factor. These methods can be divided into two classes:

- 1) methods requiring the measurement of the injection level,
- 2) methods that do not require the knowledge of injection level.

An accurate measurement of the effective injection level is generally difficult, because there always exists a mode profile mismatch between the master beam projected onto the slave laser facet and the slave guided mode. Such mismatch can reduce the effective injection to a value that is 10% to 50% of the total facet power. As a consequence, the accuracy of methods requiring the measurement of the injection level is poor, while class 1 methods can have a good or moderate accuracy. These techniques are of complicated experimental realization, and have mainly been tested with DFB laser.

### Optical Feedback

Similarly to injection phenomena, the behavior of semiconductor laser subjected to optical feedback exhibits some dependence on the actual value of the linewidth enhancement factor, and hence the value can be determined from such experiments. Most of the theoretical analysis of the dynamics and properties of semiconductor laser in presence of feedback are

based on the Lang-Kobayashi (LK) equations. In early works, experimental observations on semiconductor laser with optical feedback have been compared to theoretical results, and the linewidth enhancement factor was used as fitting parameter to achieve agreement between experiment and theory. The determination of the value of the  $\alpha_H$ -factor was often an additional outcome, as these works were not mainly focussed on this point. Similarly to injection methods, the measurement of  $\alpha_H$ -factor is less accurate where the knowledge of the effective feedback level is required. An optical feedback method purposely devoted to the measurement of the  $\alpha_H$ -factor was presented recently based on the self-mixing interferometry. According to the LK theory, the  $\alpha_H$ -factor is determined from the measurement of specific parameters of the resulting interferometric waveform, without the need for the measurement of feedback level. Optical feedback methods offer different experimental complexities, depending on the specific feature of the semiconductor laser subjected to feedback that is measured to determine  $\alpha_H$ -factor. The measured value for  $\alpha_H$ -factor is the effective value in operating conditions, and non-linear effects could be revealed at high power. However, this point shall be carefully checked because non-linearities should possibly be included also in the LK model. As a rule of thumb, methods requiring the knowledge of the feedback level have a poor accuracy, while methods that are independent from this parameter are more accurate.

### SOA devices

Semiconductor Optical Amplifiers (SOAs) represent another type of active semiconductor devices that are affected by the non-zero value of the linewidth enhancement factor. Measurements of  $\alpha_H$ -factor in SOAs have been carried out with methods that are similar in principle to the Hakki-Paoli technique. SOAs allow for higher injected carrier densities, and hence the  $\alpha_H$ -factor can be characterized over an extended range of this parameter. The more accurate technique relies on the measurement of  $dn$  via an interferometer that includes the SOA in one arm, and on  $dg$  evaluation via chip gain measurement. The accuracy of this method is good, and the results are related to the material  $\alpha_H$ -factor.

### 2.6.3 Measurements of linewidth enhancement factor from ASE and TSE spectra

For measuring the linewidth enhancement factor (2.43) can be used with other equations relating the change of the real and imaginary parts of the refractive index to the values, which can be measured experimentally. Rewriting (2.5):

$$\delta n'' = -\frac{1}{\Gamma} \frac{\delta g}{4\pi} \lambda \quad (2.59)$$

and

$$\Gamma \frac{dn'}{n'} \approx \frac{dn_{eff}}{n_{eff}} = \frac{d\lambda}{\lambda} \quad (2.60)$$

where  $n_{eff}$  is the effective group index. Substituting (2.59) and (2.60) into (2.43) we get:

$$\alpha_{HT} = -\frac{4\pi n_{eff}}{\lambda^2} \left( \frac{\partial \lambda}{\partial g} \right)_T \quad (2.61)$$

By recording the ASE at different currents below threshold and measuring the change of the gain and the wavelength shift of Fabry-Perot peaks with current one can determine the linewidth enhancement factor  $\alpha_{HT}$  and its dependence on the wavelength and current. Shown in figure 2.17(a) is a set of  $\alpha_{HT}$  factor curves measured using the above procedure. This method is now commonly used for measuring the linewidth enhancement factor. Also

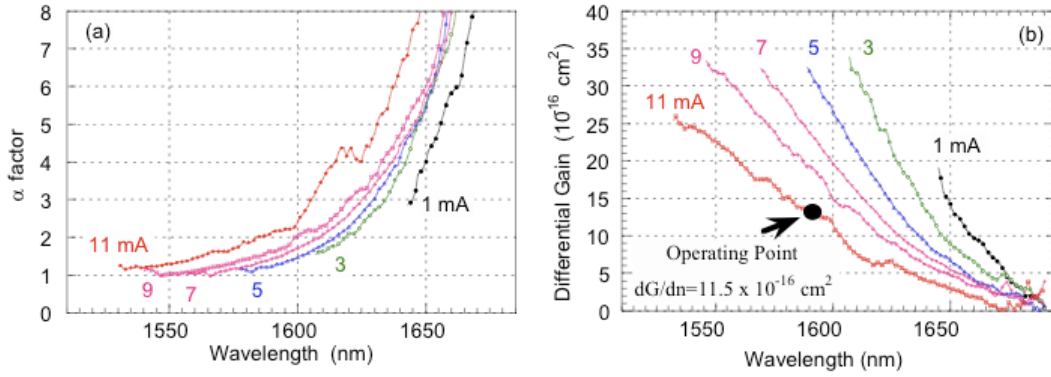


Figure 2.17: The linewidth enhancement factor (a) and differential gain (b) versus wavelength at various bias currents

presented in figure 2.17 are the measured dependencies of linewidth enhancement factor and differential gain on the wavelength for various currents. Optimizing the DFB wavelength from the data shown in figure 2.17 allowed achieving the small-signal direct modulation bandwidth of 26 GHz and linewidth enhancement factor of near 1. Shown in figure 2.17(b) is the set of the differential gain spectra determined using the below threshold gain spectra combined with the carrier lifetime measurements discussed in previous sections. It should be pointed out that the value of the differential gain obtained using this method (indicated by solid circle in figure 2.17(b) is in very good agreement with the value of the differential gain obtained in the same device from the response measurements described previously.

An alternative measurement technique for determination of  $\alpha_{HT}$  utilizes the optical gain spectra determined from TSE. Kramers-Krönig relation for small changes of refractive index is as follows:

$$\delta n' = \frac{2}{\pi} P \int_0^{+\infty} \delta n'' \frac{\epsilon'}{\epsilon'^2 - \epsilon^2} d\epsilon' \quad (2.62)$$

where  $P$  indicates taking the principal part integral. Equation (2.59) can be used to relate  $\delta G$  and  $\delta n''$  :

$$\delta n' = \frac{hc}{2\pi^2} P \int_0^{+\infty} \frac{\delta G}{\epsilon'^2 - \epsilon^2} d\epsilon' \quad (2.63)$$

The coefficient  $\alpha_T$  can be determined by substituting (2.63) into (2.43). After some simple algebra it comes:

$$\alpha_T(\epsilon) = \frac{\left(\frac{\partial n'}{\partial \mu}\right)_T}{\left(\frac{\partial n''}{\partial \mu}\right)_T} = \frac{2}{\pi} \frac{\epsilon' P \int_0^{+\infty} \delta G(\epsilon') \frac{d\epsilon'}{\epsilon'^2 - \epsilon^2}}{\delta G(\epsilon)_T} \quad (2.64)$$

Equation (2.64) allows for determination of  $\alpha_{HT}$  from the gain spectrum. In order to perform this procedure, the gain spectra should be obtained in a very broad energy range. However, the commonly used Hakki-Paoli technique for extraction of the gain spectra from amplified spontaneous emission (ASE) from the laser facet does not allow for that. Equation (2.64) requires some caution in treating the singularity at  $\epsilon' = \epsilon$ . It should also be noticed, that the TSE intensity can be measured in arbitrary units because only the ratio of the integral of the spontaneous emission to its value at certain energy enters (2.64). The ASE measurements are usually easier to perform and more accurate, but sometimes the TSE type of the measurements are the only available solution. Both methods described are based on the below threshold measurements, and therefore can give only asymptotic value of the parameters close to threshold. However they have an advantage, since they can be used to study the dependence of the linewidth enhancement factor on carrier concentration and other parameters that cannot be varied in the real operating conditions above threshold. On the other hand the results of the above threshold measurements remain definitely more accurate since they can be obtained in the exact operating conditions of the device.

## 2.7 Measurements of the Carrier Temperature and Carrier Heating in Semiconductor Lasers

Typical semiconductor lasers operate at the injection current densities of an order of 10 kA/cm<sup>2</sup> or higher. Under these conditions one can expect a significant difference between the lattice temperature  $T_L$  and the temperature of the electron-hole-plasma in the active region  $T_{e-h}$ . This difference is determined by the power acquired by carriers in the active layer and their energy relaxation time. Since the modal optical gain, wavelength chirp and carrier leakage over the heterobarrier are sensitive to the carrier temperature  $T_{e-h}$ , the study of carrier heating is important for understanding the laser physics and improving device design. Experimental studies of the heating in heterostructures using optical excitation and time resolved spectroscopy were carried out. In semiconductor lasers and light-emitting diodes, the carrier temperature is often estimated from the high-energy tail of the spontaneous emission

spectra. The problem with the estimation of carrier temperature from the high energy tail of the spontaneous emission arises from the fact that the density of states as well as matrix element of the optical transition are not well known functions of energy. This makes it difficult to analyze the spontaneous emission. Study of the thermionic emission is also nontrivial since it requires special sample geometry and is generally unsuitable for real laser structures. An interesting experimental technique allows to measure the rate of change of the carrier plasma temperature with pumping current above threshold. This method is based on the relationship between the rate of carrier heating and the wavelength chirp. Wavelength chirp results from the dependence of the real part of refractive index on current. The real and imaginary parts of refractive index are related through the Kramers-Krönig relation. Under lasing condition the distortion of spectral profile of the optical gain (and therefore the imaginary part of refractive index) is caused by spectral hole burning and carrier heating. However, the experimental studies of fast dynamics of the optical gain in semiconductor laser structures have shown that the electron-hole plasma thermalization time is much shorter than the time needed for thermal equilibrium between the plasma and crystal lattice. Therefore the carrier heating was considered to be dominant and the spectral hole burning effect was neglected. In this case the energy distribution of electrons and holes is described by Fermi functions with the same temperature. This temperature differs from the lattice temperature; also electrons and holes have different quasi Fermi level energies when voltage is applied to a laser diode. Sources of carrier heating above threshold are injection of energetic carriers from heterobarriers into active layer and free-carrier absorption. The first effect depends on the injection current and the second on the optical field. Therefore to first order approximation both effects are proportional to the difference between operating and threshold currents. In a static case above threshold the optical gain is equal to the optical loss. At the lasing wavelength, the reduction of the optical gain due to carrier heating is compensated by of the increase of the carrier concentration. Expressing this in terms of variations of the imaginary part of the refractive index yields:

$$\left(\frac{\partial n''}{\partial \mu}\right)_T d\mu + \left(\frac{\partial n''}{\partial \mu}\right)_\mu dT = 0 \quad (2.65)$$

where  $\mu$  is the quasi Fermi level separation. However, pinning of the optical gain does not occur at all wavelengths. The real part of the refractive index is related to the imaginary part (and optical gain) via the Kramers-Krönig relation. This results in the dependence of the refractive index on current above threshold and in the wavelength chirp. The full change of the real part of the index due to the same small variations  $d\mu$  and  $dT$ , can be expressed in the same terms as in

$$\left(\frac{\partial n'}{\partial \mu}\right)_T d\mu + \left(\frac{\partial n'}{\partial \mu}\right)_\mu dT = dn' \quad (2.66)$$

The linewidth enhancement factor as defined in (2.43) can also be defined as a derivative with respect to the quasi Fermi level separation because only two variables out of three ( $n$ ,  $\mu$  and  $T$ ) are independent for Fermi-distributed carriers:

$$\alpha_{HT} = \frac{\left(\frac{\partial n'}{\partial \mu}\right)_T}{\left(\frac{\partial n''}{\partial \mu}\right)_T} \quad (2.67)$$

This definition allows for easier measurement, because quasi Fermi level separation  $\mu$  is easier to determine than the carrier concentration. The Kramers-Krönig relation suggests that there is an analogous parameter relating small variations of the real and imaginary parts of the refractive index due to the change of the carrier temperature at a fixed value of the quasi Fermi level separation:

$$\alpha_{H\mu} = \frac{\left(\frac{\partial n'}{\partial T}\right)_\mu}{\left(\frac{\partial n''}{\partial T}\right)_\mu} \quad (2.68)$$

It should be noted that unlike  $\alpha_{HT}$ , the parameter  $\alpha_{H\mu}$  could be determined only from TSE measurements using a formula similar to (2.64). Determination of this parameter from ASE measurements is impossible because the shift of Fabry-Perot peaks with ambient temperature is determined mainly by the change of the effective index due to the change of the crystal lattice temperature, and not the carrier plasma temperature. Combining (2.65) and (2.68) one can relate the change of the real part of the refractive index and change of the carrier temperature:

$$dn' = -(\alpha_{HT} - \alpha_{H\mu}) \left(\frac{\partial n''}{\partial T}\right)_\mu dT \quad (2.69)$$

Equation (2.69) may be rewritten in terms of laser parameters that can be measured experimentally. Equations (2.59) and (2.60) can be used to express the change of the lasing wavelength due to the change of the carrier temperature in the active layer:

$$d\lambda = \frac{\lambda^2}{4\pi n_{eff}} (\alpha_{HT} - \alpha_{H\mu}) \left(\frac{\partial g}{\partial T}\right)_\mu dT \quad (2.70)$$

Carrier heating lifts the pinned carrier concentration (and quasi Fermi level separation) above threshold and results in wavelength chirp. The carrier heating affects the lasing wavelength in two ways, described by the two terms in brackets ( $\alpha_{HT} - \alpha_{H\mu}$ ) in (2.70). The first term corresponds to the change of the real part of the refractive index due to change of the quasi Fermi level separation. The second term describes the change in real part of the refractive index due to the change of the gain profile produced by the carrier heating. To determine accurately the change of wavelength with current in a small-signal approach, one can use a Fabry-Perot etalon method. Rewriting (2.70) for frequency chirp due to current modulation:

$$\frac{dT}{dI} = \frac{4\pi n_{eff}}{(\alpha_{HT} - \alpha_{H\mu})c} \frac{\beta}{\left(\frac{\partial g}{\partial T}\right)_\mu} \quad (2.71)$$

where  $\beta = d\nu/dI$  is the chirp parameter. Equation (2.71) establishes the relation between the rate of carrier heating above threshold and wavelength chirp. Coefficients  $\left(\frac{\partial g}{\partial T}\right)_\mu$ ,  $\alpha_{HT}$  and  $\alpha_{H\mu}$  can be determined from the gain measurements described in previous sections. Their values were:  $\left(\frac{\partial g}{\partial T_{e-h}}\right)_\mu \approx -0.45 \pm 0.05 \text{ cm}^{-1}\text{K}^{-1}$ ,  $\alpha_{HT} \approx 2.1 \pm 0.2$  and  $\alpha_{H\mu} \approx -1.4 \pm 0.3$  and  $\beta = 156 \text{ MHz/mA}$ . Using these values, the rate of change of the carrier temperature with current was estimated to be approximately  $0.13 \text{ K/mA}$ . The accuracy of the estimation is about 25%. This allows for an estimation of the carrier temperature difference between a threshold of 15 mA and a typical operating current of 50 mA to be 4.7 K. This is considerably less than estimated by other studies where the energy relaxation time of the electron-hole plasma was considered to be few picoseconds.

# Chapter 3

## Ultrafast Diode Lasers in Fiber Optics Communications

The most important application of ultrafast laser diodes is the field of optical fiber communications. Optical fiber communication systems transmit information through an optical fiber in the form of coded sequences of optical pulses. One of the principal parameters in those systems is the bit rate-distance product which is the product of the number of bits transmitted per second by the repeater spacing. The performance of optical fiber communication systems depends on the parameters of the optical fiber (dispersion and loss) and of the laser diode. In particular, the modulation bandwidth of the laser and the spectral purity of the laser emission play a crucial role and affect considerably the bit rate-distance product. Since the minimum loss in conventional silica fibers occurs around  $1.55 \mu\text{m}$  wavelength and the zero-dispersion wavelength is near  $1.3 \mu\text{m}$ , the realization of InGaAsP lasers have attracted attention as the most promising candidates for application in this field.

### 3.1 High-Speed Modulation of Laser Diodes

The main advantage of semiconductor lasers over lasers of all other types is that they can be directly modulated by the device current. Thus, direct current modulation results in the simultaneous amplitude (AM) and frequency (FM) modulations of the laser emission. This comes from the refractive index variations in the laser at the same time when the optical gain changes as a result of the carrier density variations. The interdependence between AM and FM modulations are governed by the so-called linewidth enhancement factor. In this section, we will concentrate on concepts of increasing modulation bandwidth as well as on device-dependent limitations associated to high-speed operations.

### 3.1.1 Small-Signal Modulation Response

Let us consider the dynamic response of the intrinsic semiconductor laser. A considerable amount of information can be obtained by a small-signal analysis of the rate equations that describe the interplay between the carrier density  $N(t)$  in the active layer and the photon density  $S(t)$  in the cavity. The laser single-mode rate equations can be written as follows:

$$\frac{dN}{dt} = \frac{I(t)}{eV} - \frac{N(t)}{\tau_e} - g_0(N - N_t)S \quad (3.1)$$

$$\frac{dS}{dt} = \Gamma g_0(N - N_t)S - \frac{S}{\tau_p} + \frac{\beta\Gamma N}{\tau_e} \quad (3.2)$$

The small-signal response of the intrinsic laser is obtained by linearizing the rate equations using,

$$N(t) = N_0 + \delta N(t) \quad (3.3)$$

$$S(t) = S_0 + \delta S(t) \quad (3.4)$$

$$P(t) = P_0 + \delta P(t) \quad (3.5)$$

$$I(t) = I_0 + \delta I(t) \quad (3.6)$$

with  $N_0$ ,  $S_0$ ,  $P_0$  et  $I_0$  are the steady-state (average) values of carrier, photon densities, power and current respectively. Small-signal variations are such that  $\delta I(t) \ll I_0$ ,  $\delta S(t) \ll S_0$ ,  $\delta P(t) \ll P_0$  and  $\delta I(t) \ll I_0$ . The transfer function for intensity modulation in the frequency domain is given by:

$$M(j\omega) = \frac{\delta \widetilde{S}(\omega)}{\delta \widetilde{I}(\omega)} \quad (3.7)$$

The small-signal solution of the rate equations (3.1) and (3.2) give the intrinsic frequency response  $R_{int} = \left| \frac{M(j\omega)}{M(0)} \right|$  as,

$$R_{int} = \frac{\omega_r^4}{(\omega^2 - \omega_r^2)^2 + \omega^2\gamma^2} \quad (3.8)$$

where  $\gamma$  is the damping rate and the undamped resonant frequency  $\omega_r$  is given by the relation,

$$\omega_r^2 = \frac{g_0 S_0}{\tau_p} \quad (3.9)$$

Figure 3.1 illustrates the general form of the response  $R_{int}(\omega)$  for different values of  $S_0$ . A resonance in the modulation response at  $\omega_r$  is called the relaxation oscillation and its strength depends on the spontaneous emission factor, carrier diffusion and carrier transport effects. Above the resonance peak, the magnitude of the intrinsic response approaches asymptotically a slope of -40 dB/decade. The parameter  $f_{3dB} = \frac{\omega_{3dB}}{2\pi}$  is widely referred to as the modulation bandwidth of the laser. There is a universal relationship between the resonant frequency and the damping rate. It has been demonstrated both experimentally and theoretically the  $\gamma$

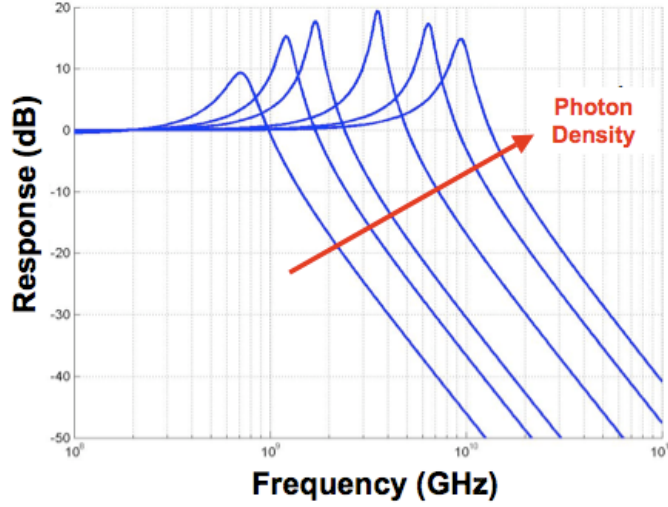


Figure 3.1: Modulation response of a laser diode for different values of the photon density

varies linearly with  $f_r^2 = (\frac{\omega_r}{2\pi})^2$ . The proportionality constant is the  $K$ -factor of the laser. The  $K$ -factor was originally defined as  $\gamma = K f_r^2$ . However a dc offset is always observed and a better definition is given by,

$$\gamma = K f_r^2 + \gamma_0 \quad (3.10)$$

From this definition and using the small-signal solution of (3.1) and (3.2), the  $K$ -factor is as follows:

$$K = 4\pi^2 \tau_p \quad (3.11)$$

The  $K$ -factor is a figure of merit for high-speed laser diodes since the maximum possible intrinsic modulation bandwidth  $f_{max}$  (3-dB bandwidth) is determined solely by this factor:

$$f_{max} = \sqrt{2} \frac{2\pi}{K} = \frac{8.88}{K} \quad (3.12)$$

This equation clearly shows that the smaller  $K$ -factor the better for high-speed operations. The  $K$ -factor depends not only on the photon lifetime as described by (3.11) but is significantly affected by nonlinear gain effects and carrier transport effects as it will be discussed later. Typical values of  $K$ -factor range from 0.2 to 0.4 ns leading to modulation bandwidths as wide as 20-40 GHz. However, this bandwidth is usually limited by RC parasitics, device heating and maximum power-handling capability of the laser facets.

### How to increase the relaxation frequency and the modulation bandwidth?

- Increasing the photon density  $S_0$  via a better confinement of the optical field in the active layer or by biasing the laser at a higher pump current. The relaxation frequency increases

with an increasing output power until the power levels when heating and catastrophic mirror damage can occur.

- Increasing the differential gain coefficient  $g_0$  by cooling the device, doping active areas or by using quantum well, quantum dot structures. An additional enhancement can be obtained with the inclusion of strain in the active layer.
- Reducing the photon lifetime by decreasing the laser-cavity length. Short-cavity devices have been experimentally demonstrated to have enhanced bandwidths.

The dynamic response of the intrinsic laser is reduced by the parasitics. Chip parasitics vary widely among different laser structures. The effect of chip parasitics can be represented by writing the electrical response  $R_e$  of the laser as follows:

$$R_e = \eta^2 \frac{1}{1 + \left(\frac{\omega}{\omega_{RC}}\right)^2} \frac{1}{1 + \left(\frac{\omega}{\omega_{pn}}\right)^2} \quad (3.13)$$

where  $\eta$  represents the low-frequency modulation efficiency caused by the sublinearity of the power-current curve and  $\omega_{RC}$  and  $\omega_{pn}$  describe the high-frequency roll-off caused by the series resistance and the diffusion capacitance of the pn junction respectively. A detailed analysis of any particular laser structure will produce a more complicated expression of (3.13). Thus, the overall laser frequency response is  $R = R_{int} \cdot R_e$ . As an example, figure 3.2 shows a two-port model of a high-speed laser diode. The laser is divided into three sections: (1) the package parasitics, (2) the parasitics associated with the laser chip and (3) the intrinsic laser that is the active region and the cavity. Input variables are the drive current and the drive voltage. The output variables are the optical power and the frequency chirp. Parasitics that are associated with the package include a bond-wire inductance and a capacitance between the input terminals. These parasitics can be decreased by the monolithic integration of the laser. The chip parasitics include resistance that is associated with the semiconductor material surrounding the active region and stray capacitance. The package parasitics are considered to be linear circuit elements while the chip parasitics are nonlinear with values depending on the input current. The dynamic responses of the parasitics and the intrinsic laser are schematically shown in the lower part of figure 3.2. In the frequency domain, the parasitics cause a high-frequency roll-off in the small-signal response. In time domain, the parasitics result in slowing-down of fast transients of the drive current waveform. The dynamic response of the overall laser is a combination of the responses of the parasitics and intrinsic laser.

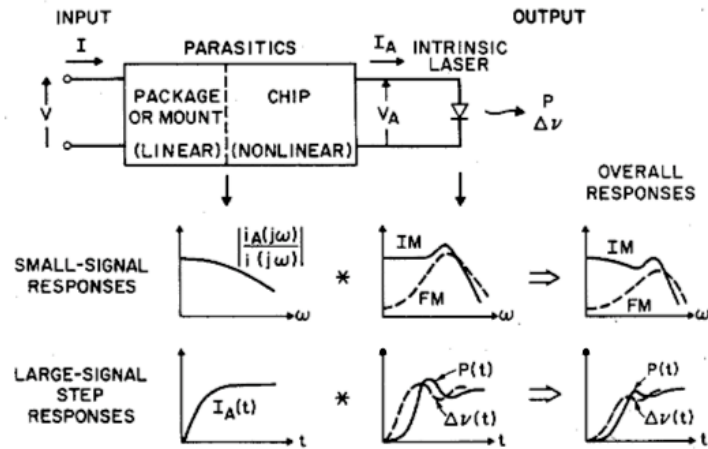


Figure 3.2: A two-port model of a laser diode and schematic of the dynamic response of the parasitics, the intrinsic laser and the overall response of the device

## 3.2 Nonlinear Gain Effects

### 3.2.1 Origin and Definition

The dependence of optical gain on the carrier concentration is a relevant approximation of the actual gain. However in practice, an additional nonlinear dependence of the gain with the photon density in the cavity is observed. At high photon densities, the gain is seen to be reduced or suppressed in comparison to the threshold gain or the gain at low photon densities. A number of physical processes such as the spectral hole burning, spatial hole burning and carrier heating are generally thought to be responsible for gain nonlinearity in laser diodes. A spectral refers to a slight reduction in gain around the spectral region at the lasing wavelength due to the finite intraband relaxation time of carriers. At the lasing wavelength, intense stimulated emission depletes electrons and holes faster than the rate at which carriers can fill the "hole". The magnitude of the gain compression produced by this effect depends critically on the intraband relaxation times. Since these times are typically less than 0.1 ps, spectral-hole burning can affect the generation and amplification of picosecond and subpicosecond optical pulses. Recent experiments have also shown that carrier heating may also be responsible for nonlinear gain. The fast carrier thermalization maintains electrons and holes in thermal equilibrium with each other at temperatures that are higher than that of the lattice. The carrier heating is brought about by stimulated emission and free-carrier absorption. The heated electron-hole plasma loses its energy to the lattice by a combination of relaxation processes. The higher carrier temperature results in an optical gain suppression because the gain is a sensitive function of carrier temperature. Due to the fact that the

electron-hole thermalization is a fast process, the dynamic characteristics of laser diodes on picosecond and subpicosecond time scales must be affected by dynamic carrier heating. An analytical expression of gain, accounting for the effects of photon density is usually written such as:

$$g(N, S) = \frac{g_0(N - N_t)}{(1 + \epsilon_S S)^m} \quad (3.14)$$

with  $\epsilon_S$  the nonlinear gain coefficient (or gain compression coefficient),  $S$  the photon density and  $m$  a fitting constant that is often considered as close to the unity or a half. Three forms of the above general expression are often used in the literature. The first one is  $g \propto 1 - \epsilon_S S$  for low photon densities and  $m = 1$ . It is directly related to the third-order nonlinear susceptibility of a semiconductor. The second form which is  $g \propto (1 - \epsilon_S S)^{-1}$  with  $m = 1$ , results from a two-level-atom treatment for laser diodes. And finally, the third one given by  $g \propto (1 - \epsilon_S S)^{-1/2}$  with  $m = 1/2$  is derived from a more rigorous solution using an approximation for the density of states function.

**Note:** Because of the quantum confinement of electrons, it can be shown that the nonlinear effects are enhanced in quantum well lasers. QW lasers with thinner quantum-well thickness have larger nonlinear gain coefficient at the constant linear bulk gain. By designing the number of quantum wells in the laser, it is possible to control the gain nonlinearity. At the lasing condition, the modal gain equals the total loss. The modal gain is defined by the bulk gain multiplied by the optical confinement factor. Since the latter is proportional to the number of quantum wells, one can control the carrier concentration (the bulk gain) through optimization of the number of quantum wells. Therefore it can be shown that the nonlinear gain coefficient becomes larger when decreasing the bulk gain. As a consequence the gain nonlinearity is stronger in multiple quantum well lasers than that in a single quantum well lasers. Thus, the gain nonlinearity is expected to be enhanced in quantum wire and quantum dot based devices.

When nonlinear gain effects are included the relaxation frequency as well as the K-factor of the laser are modified. Using the standard rate equations including the gain compression coefficient with small-signal analysis, it comes:

$$\omega_r^2 = \frac{g_0 S_0}{\tau_p (1 + \epsilon_S S_0)} \quad (3.15)$$

and,

$$K = 4\pi^2 \left( \tau_p + \frac{\epsilon_S}{g_0} \right) \quad (3.16)$$

Using the nonlinear gain form with  $m = 1/2$ , the relaxation frequency and  $K$ -Factor are given by different expressions: for instance for the resonant frequency, we get:

$$\omega_r^2 = \frac{g_0 S_0}{\tau_p (1 + \epsilon_S S_0)^{1/2}} \quad (3.17)$$

The effect of nonlinear gain on the maximum possible modulation 3-dB bandwidth  $f_{max}$  of the laser is illustrated in figure 3.3. For comparison, the dependence of  $f_{max}$  on  $\epsilon_S$  is calculated for two values of differential gain coefficient  $g_0$  and two values of  $\tau_p$ . Frequency  $f_{max}$  is strongly dependent on the gain compression coefficient. Nonlinear gain must be considered when ultrafast laser diodes are designed. A characteristic feature of the curves shown in figure 3.3 is that when  $\epsilon \rightarrow 0$  the maximum modulation bandwidth is primarily determined by  $\tau_p$  whereas for large values of  $\epsilon_S$ , frequency  $f_{max}$  is affected by  $g_0$  only.

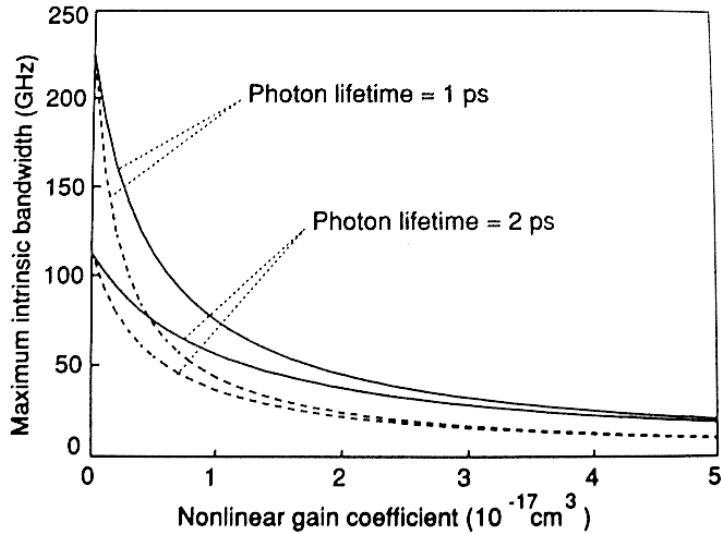


Figure 3.3: The calculated maximum possible intrinsic modulation bandwidth versus the nonlinear gain coefficient for two values of  $\tau_p$  and  $g_0$  of  $2.4 \cdot 10^{-6} \text{ cm}^3 \text{ s}^{-1}$  (dashed lines) and  $5 \cdot 10^{-6} \text{ cm}^3 \text{ s}^{-1}$  (solid lines)

### 3.2.2 Evaluation of the Gain Compression in Quantum Dot/Dash Devices

Measuring the frequency response as a function of the output power is a common method to evaluate gain compression in semiconductor lasers. In the case of the QD laser, effects of gain compression are more important than those measured on quantum well devices. In order to explain this phenomenon, a modified nonlinear gain coefficient can be introduced leading to

a new expression for the relaxation frequency under strong gain saturation such as:

$$f_r^2 = \frac{v_g g S}{4\pi^2 \tau_p (1 + \epsilon_S S)} \approx \frac{v_g g_0 S}{4\pi^2 \tau_p (1 + \epsilon_{S,eff} S)} \quad (3.18)$$

with  $v_g$  being the group velocity,  $g$  the differential gain,  $g_0$  the differential gain at threshold (unsaturated value),  $S$  the photon density,  $\tau_p$  the photon lifetime,  $\epsilon_S$  the gain compression factor related to the photon density and  $\epsilon_{S,eff}$  the effective gain compression factor defined as follows:

$$\epsilon_{S,eff} = \frac{\epsilon_S}{1 - \frac{g_{th}}{g_{max}}} \quad (3.19)$$

where  $g_{th}$  is the gain at threshold and  $g_{max}$  is the maximum gain for GS-lasing. Equation (3.19) indicates that the gain compression is enhanced due to gain saturation by a factor of  $g_{max}/(g_{max} - g_{th})$ . In Fig. 3.4 the evolution of the normalized gain compression  $\epsilon_{S,eff}/\epsilon_S$  is plotted as a function of the ratio  $g_{max}/g_{th}$ . This shows that the higher the ratio  $g_{max}/g_{th}$  the lower the effects of gain compression. If  $g_{max} \gg g_{th}$  the graph tends to an asymptote such that  $\epsilon_{S,eff}/\epsilon_S \rightarrow 1$ . On the other hand if  $g_{max} \ll g_{th}$ , gain compression effects are strengthened: the ratio increases drastically and can even be extremely large if not enough gain is provided within the structure ( $g_{max} \approx g_{th}$ ). In Fig. 3.5, the square of the measured

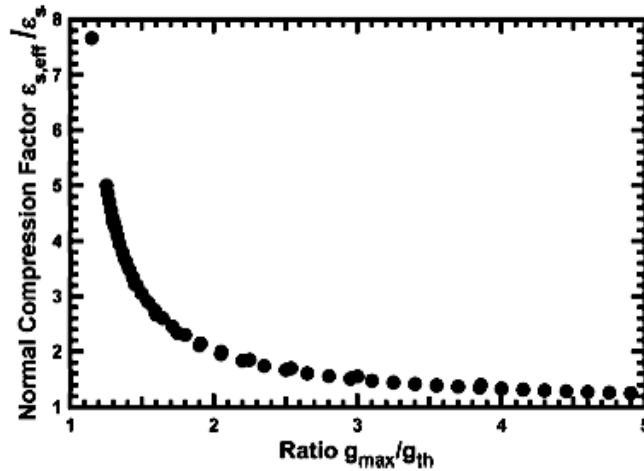


Figure 3.4: Normalized compression factor as a function of  $g_{max}/g_{th}$

resonance frequency is plotted as function of the output power which is linked to the photon density through the relation with  $h\nu$  the energy per photon,  $V$  the cavity volume and  $\alpha_m v_g$  the energy loss through the mirrors,  $\alpha_m$  being the mirror loss. The experimental dependence of the relaxation oscillation frequency shows a deviation from the expected proportionality given by expression (3.18) (case with  $\epsilon_S = 0$ ) on the square root of the optical output power. As shown in the inset, a curve-fit based on equation (3.18) is used to express the gain compression

in terms of a saturation power,  $P_{sat} \approx 3.3$  mW, where  $\epsilon_S S = \epsilon_P P = P/P_{sat}$  with  $\epsilon_P$  the gain compression coefficient related to the output power  $P$ . This value means that at this level of output power, non-linear effects start to be significant. Owing to the value of the saturated power  $P_{sat}$ , the gain compression coefficient related to the output power is estimated to be  $\epsilon_P = 1/P_{sat} = 0.3$  mW<sup>-1</sup>. The maximum of the resonance frequency can be directly deduced from the curve-fitting as  $f_r = (AP_{sat})^{1/2}$  and is expected to be  $\approx 5$  GHz (not shown in fig. 3.5). Taking into account the facet reflectivity as well as the modal volume of the laser, the

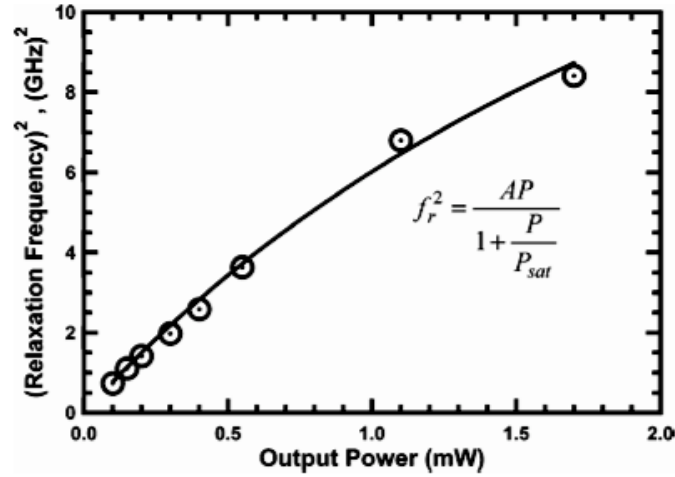


Figure 3.5: The square of the resonance frequency versus the output power. The curve-fitting equation is shown in the inset and leads to  $A=7.5 \pm 0.2$  (GHz)<sup>2</sup> mW<sup>-1</sup> and  $P_{sat}=3.3 \pm 0.3$  mW.

order of magnitude for the gain compression factor  $\epsilon_S$  is in the range from  $5 \cdot 10^{-15}$  cm<sup>3</sup> to  $10^{-16}$  cm<sup>3</sup>. This value remains much larger than those measured on QW lasers (typically around  $10^{-17}$  cm<sup>3</sup>).

### 3.2.3 Consequences on the Linewidth Enhancement Factor

In QW lasers, which are made from a homogeneously broadened gain medium, the carrier density and distribution are clamped at threshold. As a result, the change of the  $\alpha_H$ -factor is due to the decrease of the differential gain from gain compression and can be written according to the relation:

$$\alpha_H(P) = \alpha_{H0}(1 + \epsilon_P P) \quad (3.20)$$

where  $\alpha_{H0}$  is the linewidth enhancement factor at threshold. Since the carrier distribution is clamped,  $\alpha_{H0}$  itself does not change as the output power increases. As an example, figure 3.6

shows the measured linewidth enhancement factor versus the output power for a QW DFB laser. Black squares correspond to experimental data. As described by equation (3.20), the effective  $\alpha_H$ -factor linearly increases with the output power. By curved-fitting those data, the  $\alpha_H$ -factor at threshold is found to be around 4 while the gain compression coefficient equals  $3 \cdot 10^{-2} \text{ mW}^{-1}$ . Compare to QD lasers, such a value of the gain compression coefficient is much lower since the enhancement of the effective  $\alpha_H$ -factor is not significant over the range of power. It is worthwhile noting that modifying the laser's rate equations and including the

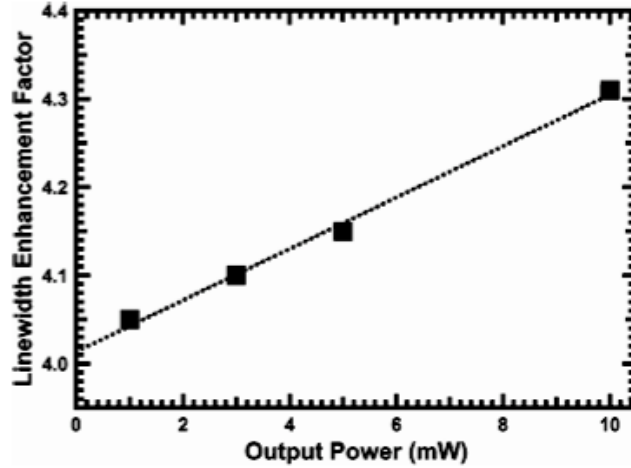


Figure 3.6: The effective linewidth enhancement factor as a function of the output power for the QW DFB laser.

effects of intraband relaxation, the  $\alpha_H$ -factor can be re-expressed as follows:

$$\alpha_H(P) = \alpha_{H0}(1 + \epsilon_P P) + \beta \epsilon_P P \frac{\epsilon_P P + 1}{\epsilon_P P + 2} \quad (3.21)$$

with  $\beta$  the parameter related to the slope of the linear gain which controls the nonlinear phase change. The situation for which  $\beta=0$  corresponds to an oscillation purely located at the gain peak. However, second part of (3.21) usually remains small enough to be neglected.

In QD lasers, the carrier density and distribution are not clearly clamped at threshold because the inhomogeneous broadening gain is more predominant. Indeed, the lasing wavelength, can switch from GS to ES as the current injection increases meaning that a carrier accumulation occurs in the ES even though lasing in the GS is still occurring. The filling of the ES inevitably increases the  $\alpha_H$ -factor of the GS introducing an additional dependence with the injected current. Thus taking into account the gain variation at the GS and at the ES, the

index change at the GS wavelength can be written as follows:

$$\delta n = \sum_{GS,ES} \alpha_k \delta g_k \quad (3.22)$$

with  $k = GS, ES$  the indexes of summation for GS and ES respectively. Equation (3.22) leads to:

$$\delta n = \left( \alpha_{GS} + \alpha_{ES} \frac{a_{ES}}{a_{GS}} \right) \equiv \alpha_H \delta g \quad (3.23)$$

In (3.23),  $\delta g$  and  $\delta n$  are the changes of the gain and refractive index at the GS, respectively,  $\alpha_H$  is the GS-linewidth enhancement factor actually measured in the device,  $a_{ES}$  and  $a_{GS}$  are the differential gains at the ES and at the GS, respectively,  $\alpha_{ES}$  describes the change of the GS index caused by the ES gain and  $\alpha_{GS}$  is related to the GS index change caused by the GS gain variation. When the laser operates above threshold,  $\alpha_{GS}$  keeps increasing with  $\alpha_{GS}(1 + \epsilon_P P)$  as previously shown for the case of QW devices. Let us note that the differential gain at GS,  $a_{GS}$ , can also be simply expressed as a function of the gain compression coefficient as well as  $g_{max}$  and  $g_{th}$ . Indeed, it has been shown that the gain saturation in a QD media can be described by the following equation:

$$g_{GS} = g_{max} \left( 1 - e^{-\ln(2)(N/N_t-1)} \right) \quad (3.24)$$

with  $N$  the carrier density and  $N_{tr}$  the transparency carrier density. When the laser operates above threshold, the differential gain for the GS lasing is defined as follows:

$$a_{GS} = \frac{dg_{GS}}{dN} = \frac{\ln(2)}{N_t} (g_{max} - g_{GS}) \quad (3.25)$$

with  $g_{GS} = g_{th}(1 + \epsilon_P P)$  the uncompressed material gain increasing with the output power. Equation (3.25) leads to:

$$a_{GS} = a_0 \left( 1 - \frac{g_{th}}{g_{max} - g_{th}} \epsilon_P P \right) = a_0 \left( 1 - \frac{g_{th}}{g_{max} - g_{th}} \epsilon_S S \right) \quad (3.26)$$

with  $a_0$  the differential gain at threshold. Then using equations (3.20), (3.23) and (3.26), the linewidth enhancement factor can be written as:

$$\alpha_H(P) = \alpha_{GS}(1 + \epsilon_P P) + \frac{\alpha_1}{1 - \frac{g_{th}}{g_{max} - g_{th}} \epsilon_P P} \quad (3.27)$$

with  $\alpha_1 = \alpha_{ES}(a_{ES}/a_0)$ . The first term in equation (3.27) denotes the gain compression effect at the GS (similar to QWs) while the second is the contribution from the carrier filling in the ES that is related to the gain saturation in the GS. For the case of strong gain saturation, (3.27) can be reduced to:

$$\alpha_H(P) \approx \frac{\alpha_1}{1 - \frac{g_{th}}{g_{max} - g_{th}} \epsilon_P P} \quad (3.28)$$

In figure 3.7, the normalized linewidth enhancement factor  $\alpha_H/\alpha_0$  is calculated through (3.28) and reported in the (X,Y) plane with  $X = P/P_{sat}$  and  $Y = g_{max}/g_{th}$ . This picture acts as a stability map that simply shows that a larger maximum gain is absolutely required for a lower and stable  $\alpha_H/\alpha_0$  ratio. For instance let us consider the situation for which  $g_{max} = 3g_{th}$ : at low output powers i.e,  $P < P_{sat}$ , the normalized  $\alpha_H$ -factor remains constant ( $\alpha_H/\alpha_0 \approx 3$ ) since gain compression is negligible. On the other hand, as soon as the output power approaches  $P_{sat}$ , and goes beyond, the ratio  $\alpha_H/\alpha_0$  is increased. Gain compression effects lead to an enhancement of the normalized  $\alpha_H$ -factor, which can go up to 10 for  $P \approx 2P_{sat}$  level of injection for which the ES occurs. On the other hand, assuming  $g_{max} = 5g_{th}$ ,

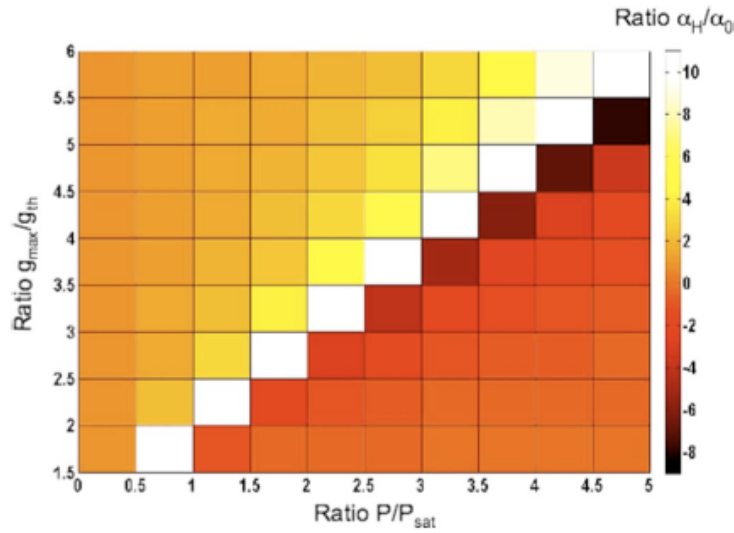


Figure 3.7: Stability map based for the normalized linewidth enhancement factor  $\alpha_H/\alpha_0$  in the  $(P/P_{sat}, g_{max}/g_{th})$  plane

figure 3.7 shows that the effects of gain compression are significantly attenuated since the ratio  $\alpha_H/\alpha_0$  remains almost constant over a wider range of output power. The level at which gain compression starts being critical is now shifted to  $P \approx 3P_{sat}$  instead of  $P \approx P_{sat}$ . Let us also stress that at a certain level of injection, the normalized GS  $\alpha_H$ -factor can even become negative. This effect has already been experimentally may occur when the GS gain collapses, e.g when ES lasing wavelength occurs. In figure 3.8, the calculated GS  $\alpha_H$ -factor (black dots) of the QD-laser under study is depicted as a function of the bias current. Grey stars superimposed correspond to data measurements which have been obtained via the AM/FM technique. This method consists of an interferometric method: the output optical signal from the laser operated under small-signal direct modulation is filtered in a 0.2 nm resolution monochromator and sent in a tunable Mach-Zehnder interferometer. From separate measurements on opposite slopes of the interferometer transfer function, phase and amplitude

deviations are extracted against the modulating frequency, in the 50 MHz to 20 GHz range. The  $\alpha_H$ -factor is given by the phase to amplitude responses ratio at the highest frequencies, in the limits of the device modulation bandwidth. Thus, a qualitative agreement between

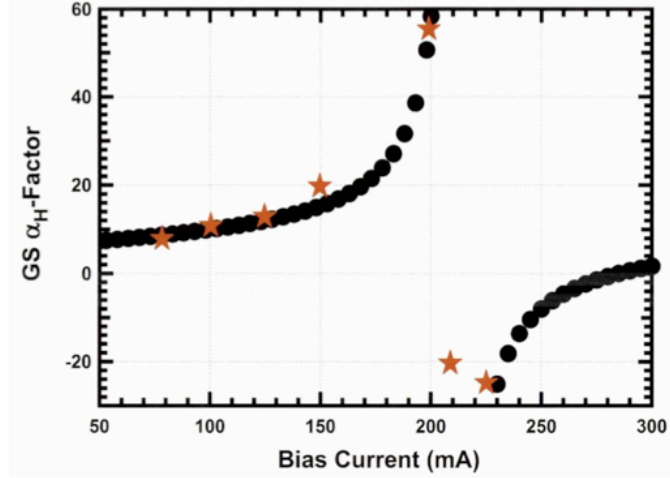


Figure 3.8: Calculated GS  $\alpha_H$ -factor versus the bias current (black dots). Superimposed stars correspond to experimental data

simulations and measurements is obtained. As expected, the GS  $\alpha_H$ -factor increases with the injected current due to the filling of the excited states as well as carrier filling of the non-lasing states (higher lying energy levels such as the wetting layer), which results in a differential gain reduction above threshold. Although the  $\alpha_H$ -factor is enhanced at lower output powers, this increase stays relatively limited until the bias current remains lower than 150 mA e.g such that as  $P < P_{sat}$ . Beyond that, compression effects starts being significant and the  $\alpha_H$ -factor reaches a maximum of 57 at 200 mA before collapsing to negative values. As previously mentioned, the collapse in the  $\alpha_H$ -factor is attributed to the occurrence of the ES as well as to the complete filling of the available GS states. In other words, as the ES stimulated emission requires more carriers, it affects the carrier density in the GS, which is significantly reduced. As a result, the GS  $\alpha_H$ -factor variations from 57 down to -30 may be explained through a modification of the carrier dynamics such as the carrier transport time including the capture into the GS. This last parameter affects the modulation properties of high-speed lasers via a modification of the differential gain.

### 3.3 Quantum-Well Lasers and Carrier-Transport Effects

The use of quantum wells can lead to considerable improvement in the modulation response of laser diodes mainly due to the enhanced differential gain. Therefore, the higher the differ-

ential gain, the larger the bandwidth. In contrast to bulk lasers, the differential gain in QW lasers is a structure-dependent parameter; it is determined not only by the material parameters of the active layer but also influenced by the dimensions of the QW and barrier layers, the optical confinement factor, and the carrier injection and confinement processes. An accurate design of the active layer and cladding layers plays a crucial role in the high-speed performance of QW devices. P-doping of the active layer has been also predicted to enhance the differential gain and decrease the  $K$ -factor of high-speed QW devices. For instance a maximum possible intrinsic bandwidth of 63 GHz ( $K$ -factor of 0.14ns) has been reported in strained p-doped InGaAs/GaAs MQW lasers. However, the  $K$ -factor and consequently the maximum modulation frequency are affected by nonlinear gain effects that reduce the modulation bandwidth. Because of the inclusion of strain as well as of the quantum confinement, it has been proposed that the gain compression coefficient is enhanced in QW lasers. Despite the enhanced differential gain, the smallest value of the  $K$ -factor observed in these lasers is not significantly below the best values reported for bulk lasers. Also, there has been a large variation in the  $K$ -factors reported for QW lasers (from 0.13 to 2.4 ns) but for bulk lasers this parameter has been measured within the relatively narrow range of 0.2 to 0.4ns. The concept of a well barrier hole burning has been proposed as a possible explanation of this variation. Basically, it consists of an additional contribution to the intrinsic gain compression coefficient which is structure-dependent. Another explanation is that carrier transport effects can have a significant impact on the modulation properties via a reduction of the effective differential gain and not through an enhancement of gain-compression coefficient. This implies that the enhancement of the compression coefficient in QW lasers may not be the primary reason for additional increase of the  $K$ -factor.

Unlike the bulk lasers, QW ones have a very small active areas and carrier-transport effects has to be considered. This implies that a separate confinement heterostructure (SCH) is necessary to optimize the transverse optical confinement factor. A SCH layer is inserted between the normally doped cladding regions and the quantum-well active region. A single QW laser with a SCH is illustrated in figure 3.9. Electron and hole transport from the cladding layers to the quantum-well active area. Sub-picosecond time-resolved measurements of the luminescence decay in QW structures have shown that the carrier capture time into the QW is roughly 1 ps. Another significant physical mechanism is the thermally activated carrier escape from the QW. This mechanism often called thermoionic emission (associated effective time  $\tau_e$ ) is a strong function of the barrier height. In MQW lasers tunneling effects between the quantum wells may also occur.

Rate equations used below describe the dynamics of the carrier densities in the quantum well  $N_W$  and the SCH layer  $N_{SCH}$  as well as the photon density dynamics in the laser cavity. The

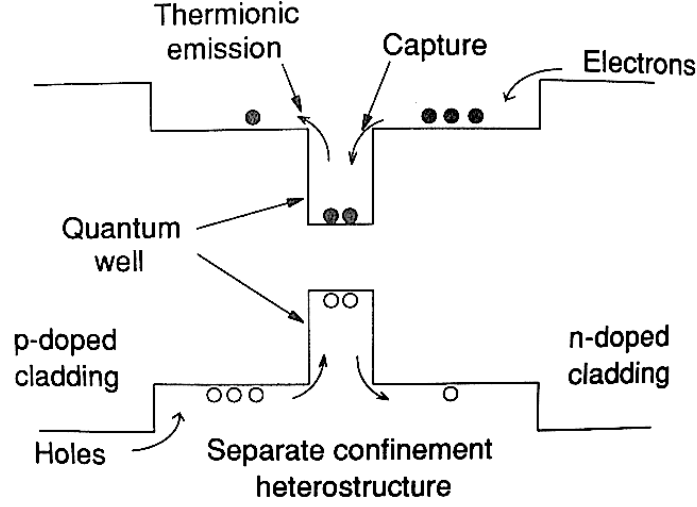


Figure 3.9: Carrier transport in a single separate confinement heterostructure (SCH)

basic equations can be written as follows:

$$\frac{dN_{SCH}}{dt} = \frac{I(t)}{eV_{SCH}} - \frac{N_{SCH}}{\tau_{tr}} - \frac{N_{SCH}}{\tau_{n1}} + \frac{N_W}{\tau_e} \frac{V_W}{V_{SCH}} \quad (3.29)$$

$$\frac{dN_W}{dt} = -\frac{G(N_W)S}{1 + \epsilon_S S} - \frac{N_W}{\tau_e} - \frac{N_W}{\tau_{n2}} + \frac{N_{SCH}}{\tau_{tr}} \frac{V_{SCH}}{V_W} \quad (3.30)$$

$$\frac{dS}{dt} = \frac{\Gamma G(N_W)S}{1 + \epsilon_S S} - \frac{S}{\tau_p} + \frac{\beta \Gamma N_W}{\tau_{n2}} \quad (3.31)$$

where  $V_{SCH}$  is the volume of the SCH,  $V_W$  is the volume of the QW,  $\tau_{n1}$  and  $\tau_{n2}$  are the carrier recombination lifetimes in the SCH and active regions, respectively and  $G(N_W)$  is the carrier density-dependent gain. From the small-signal analysis, (3.29), (3.30) and (3.31) and for negligible  $\tau_{n1}$  and  $\tau_n \equiv \tau_{n2}$  one obtains the following analytical approximations for the relaxation frequency and damping rate:

$$\omega_r^2 = \frac{(g_0/\chi)S_0}{\tau_p(1 + \epsilon_S S_0)} \left( 1 + \frac{\epsilon_S}{g_0 \tau_n} \right) \quad (3.32)$$

$$\gamma = \frac{(g_0/\chi)S_0}{(1 + \epsilon_S S_0)} + \frac{\epsilon_S S_0}{\tau_p(1 + \epsilon_S S_0)} + \frac{1}{\chi \tau_n} \quad (3.33)$$

where the transport factor  $\chi$  is given by,

$$\chi = 1 + \frac{\tau_{tr}}{\tau_e} \quad (3.34)$$

Using (3.32) and (3.33) a relationship for the  $K$ -factor can be derived:

$$K = 4\pi^2 \left( \tau_p + \frac{\epsilon_S}{g_0/\chi} \right) \quad (3.35)$$

For  $\chi = 1$  (3.32) and (3.35) transform into (3.15) and (3.16) for the case without carrier transport effect. The first effect of the carrier transport consists of a parasitic-like roll-off in the modulation response that would significantly limit the 3-dB bandwidth for large  $\tau_{tr}$ . This limitation which originates from the finite transport time across the SCH is distinguishable from the parasitics. The second effect is the reduction of the effective differential gain by a factor of  $\chi$ . This leads to a reduction of the relaxation frequency for the same power levels. The third effect is that the gain compression factor remains unmodified. Figure 3.10 illustrates the carrier-transport effects on the maximum possible modulation bandwidth of a 300- $\mu\text{m}$  QW laser. The dashed line shows the calculated  $K$ -factor limit (no carrier transport) of the maximum modulation bandwidth as a function of the SCH width. The limit determined by the carrier transport model is shown by the solid line. The difference in the maximum possible modulation bandwidth is negligible for the SCH width below 50 nm. However the frequency roll-off due to carrier transport becomes severe for a SCH width larger than 80 nm.

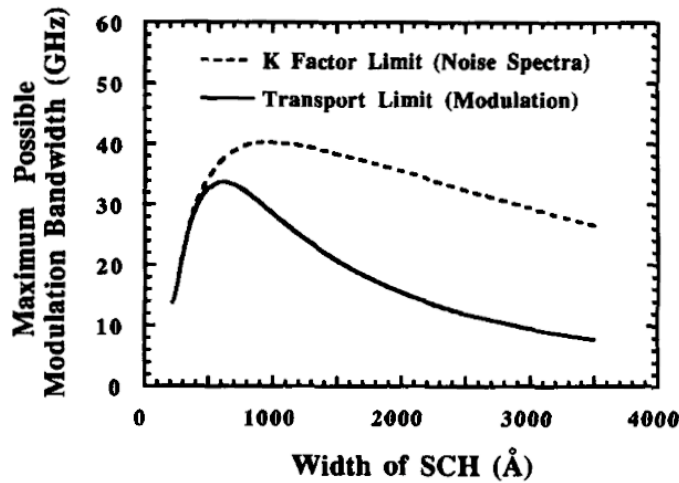


Figure 3.10: Maximum modulation bandwidth against the SCH width. The dashed line shows the maximum possible bandwidth without taking into consideration carrier transport effects

**Note:** In order to optimize the high-speed performance of QW lasers, the transport time across the SCH must be minimized. A narrower SCH should result in a shorter  $\tau_{tr}$ . However decreasing the SCH width below an optimum value will also lead to a drop in the optical-confinement factor and in an increase of the internal loss. This will result in a higher threshold carrier density and consequently a lower differential gain originating from rapid gain saturation in QW lasers. Also from (3.34) and (3.35), the thermo-ionic emission lifetime  $\tau_e$  should be maximized. This can be done with deeper and wider quantum wells. However

in MQW lasers, increasing the depth of the quantum wells or the barrier width can result in poor carrier transport between the wells due to carrier trapping in the quantum wells.

### 3.4 Large-Signal Effects

The analysis presented in the previous sections is concerned with the small-signal modulation response of laser diodes. The term small-signal implied that the modulation depths of the drive current and optical output are less than 1. However, in high-bit-rate digital optical fiber communication systems, the on-to-off ratio in the laser output should be as large as possible to avoid excessive power penalty. Large signal modulation can be realized by biasing the laser close to the threshold and modulation with current pulsed of large amplitude. The large-signal modulation response is generally worse compared to the small-signal one. Due to the highly nonlinear properties of laser diodes, the large-signal dynamic response can be quite complex. For instance, figure 3.11 shows the idealized rectangular input current drive waveform and the resulting large-signal response of the laser. The dc current  $I_0$  can either be slightly below or above the threshold. The turn-on-time of the laser  $t_{on}$  is an important parameter that affects the maximum achievable bit rate in digital systems. The turn-on-time is a function of  $I_0$  that increases while the current increases too. The turn-on behavior is

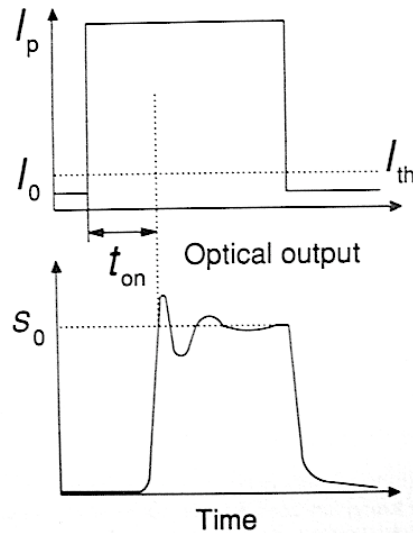


Figure 3.11: Large-signal laser response to a rectangular current pulse

improved provided the laser is bias above threshold. The rate-equations analysis shows that  $t_{on}$  can drop by an order of magnitude from several hundreds of picoseconds to 30 to 60 ps when  $I_0$  is varied from below the threshold to 30 to 40% above the threshold. The overshoot in the optical power is decreased as  $I_p/I_{th}$  is increased. The frequency of damped relaxations

oscillations is roughly equal to the relaxation frequency. The damping is strongly affected by spontaneous emission that contributed to the laser mode, carrier diffusion and nonlinear gain effects.

Figure 3.12 shows the simulated optical pulse shapes using the rate-equations for a 1.5- $\mu\text{m}$  laser diode biased at threshold ( $I_0 = I_{th}$ ) and modulated at 5 Gbps rate with  $I_p = I_{th}$  for three different values of the saturation parameter  $p = \epsilon_S S_0$  related to the gain compression coefficient,  $S_0$  being the steady-state photon density corresponding to an output power of 12 mW. For moderate values of  $\epsilon_S$  (dashed line), the main effect of nonlinear gain is to suppress relaxation oscillations. For large  $\epsilon_S$  (dotted line), the fall time of the pulse increases considerably. In a communication system, the long trailing edge would even affect the system performance through the inter-symbol interference. Gain nonlinearities are thought to set a limit on the on-state power well-below the saturation power level to avoid the detrimental effects of long trailing edge of optical pulses. As the modulation index of the current modulation is increased, novel effects in laser dynamics can be observed. The simplest one is the generation of optical pulses similar to those observed in mode-locked lasers. Directly modulated lasers

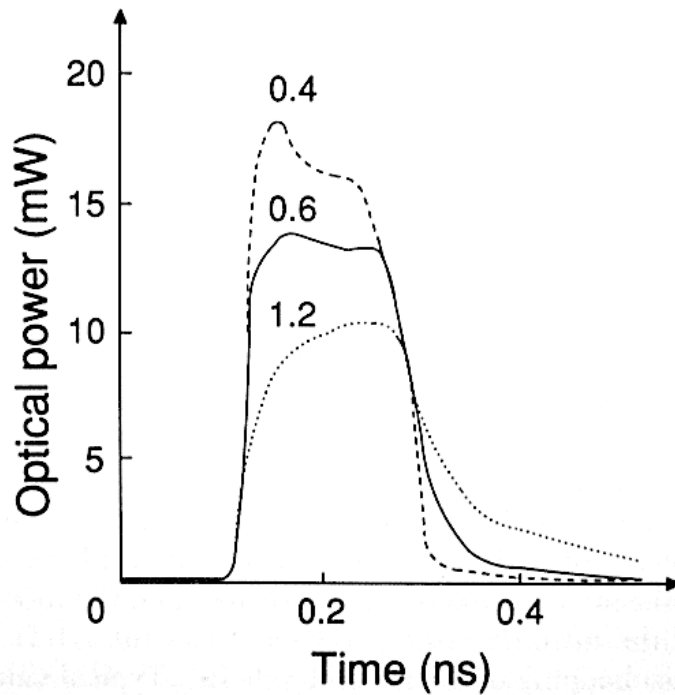


Figure 3.12: Effect of nonlinear gain on the large-signal laser response. Optical waveforms are calculated for different values of parameter  $p = \epsilon_S S_0$

can also exhibit a variety of nonlinear dynamic effects including resonance frequency shift, period doubling, period quadrupling and chaos. Some studies have demonstrated that deterministic chaos can occur at large modulation index (2 to 4) via period doubling. It has also

been shown that nonlinear gain effects can considerably suppress higher order bifurcations and the chaotic behavior in directly modulated lasers. In conclusion, these types of irregular behavior are drastically damaging to applications in optical fiber communication system and has to be avoided.

## 3.5 Spectral Broadening and Spectral Control Under High-Speed Modulation

### 3.5.1 Frequency Chirping

The enhanced linewidth and frequency chirp under the direct current modulation originate from variations in the carrier density and from the finite difference in carrier density between the laser on and off states. The chirping response of a diode laser is determined by means of the rate equations of the forms (3.1), (3.2) and (3.14) with an additional differential equation that describes the evolution of the optical phase  $\phi(t)$  such as:

$$\frac{d\phi}{dt} = \frac{1}{2}\alpha_H \left( \frac{\Gamma g_0(N - N_t)S}{1 + \epsilon_S S} - \frac{1}{\tau_p} \right) \quad (3.36)$$

The frequency chirp or chirp is defined as  $\Delta(t) = (1/2\pi)d\phi/dt$ . Based on (3.36), the chirp can be directly expressed as a function of the output power:

$$\Delta\nu(t) = \frac{\alpha_H}{4\pi} \left( \frac{d \ln P(t)}{dt} + \frac{2\Gamma\epsilon_S n P(t)}{V\eta\hbar\omega} \right) \quad (3.37)$$

where  $\eta$  is the laser differential quantum efficiency. From (3.37) it is clear that the linewidth enhancement factor  $\alpha_H$  plays a major role in obtaining low-chirp emission from high-speed directly modulated lasers. Typical values of  $\alpha_H$  in most lasers lie in the range from 3 to 5. The magnitude of the chirp represented by the first term of (3.37) may be large during high-speed turn-on and turn-off transients but may also be relatively small at the on and off levels. The second term results in frequency off-set between the on and off levels owing to the difference in steady-state values of the carrier density. Under digital modulation, when zeros of the pulse sequence are close to threshold, shoulder can be apparent on both the long-wavelength and short-wavelength sides of the optical spectrum. The former is attributed to the relaxation oscillations and light present in the trailing edges and nominal zeros of the pulse stream while the latter results from the relaxation oscillations at turn on.

### 3.5.2 Low-Chirp Lasers

The development of laser structures with  $\alpha_H < 2$  has attracted considerable attention. According to equation (2.43), this parameter is inversely proportional to the differential gain

of the laser medium. Since the differential is supposed to be enhanced in QW lasers, the  $\alpha_H$ -factor has been observed to be reduced in this type of devices. However, the  $\alpha_H$ -factor is structure dependent parameter and the effective linewidth enhancement factor  $\alpha_{eff}$  should be used in (3.37) for the chirp evaluation.  $\alpha_{eff}$  normally exceeds  $\alpha_H$ . In the case of QW lasers, carrier transport and especially carrier-density variation in the SCH region has a significant impact on  $\alpha_H$ -factor and frequency chirping and leads to enhanced values of  $\alpha_{eff}$ .

Some achievements to maintain the  $\alpha_H$ -factor values have been obtained through:

- Strained QW lasers usually exhibit reduced  $\alpha_{eff}$ -factor. For instance, the  $\alpha_{eff}$ -factor of an unstrained MQW DFB lasers was estimated to be 3.1 at 1.55  $\mu\text{m}$  while a similar structure with a compressive strain had one as low as 1.1.
- P-type modulation of QWs has also been demonstrated in order to reduce the  $\alpha_H$ -factor. A reduction by a factor of two due to modulation doping in both 1.3- and 1.55  $\mu\text{m}$  InGaAsP/InP strained MQW lasers was observed.
- Since the  $\alpha_H$ -factor depends on the wavelength, the frequency chirp of a laser can be controlled by detuning the lasing wavelength with respect to the gain peak. Fabry-Perot lasers normally lase at the gain peak. However DBR and DFB devices can be tuned to any wavelength as long as the gain peak is positive. This effect is usually to increase the differential gain in such structures. Figure 3.13 shows the calculated wavelength of the material gain, differential gain and  $\alpha_H$ -factor of a typical QW laser. As the wavelength is tuned to shorter wavelengths from the material gain peak, the differential gain increases while the  $\alpha_H$ -factor decreases. The latter becomes even equal to zero in the vicinity of the differential gain peak. Something interesting to stress is that the condition to get  $\alpha_H \approx 0$  lies in the absorption region which is the location where the material gain is negative. This means that the wavelength detuning solely cannot result in decreasing  $\alpha_H$  to zero. The differential gain peak has to be shifted toward the longer wavelengths in a region where the material gain gets positive. The differential gain spectrum is sensitive to any changes in the valence band structure. Therefore band-structure engineering can offer a number of ways to solve the problem.

## 3.6 Fundamental Limitations

In this section, some fundamental limitations of multi-gpbs fiber optic digital transmission systems exploiting ultra-fast laser diodes are presented. The performance of such systems appear to be limited by optical power, loss of the fiber, nonlinear effects in both the laser and in the fiber, the spectral bandwidth of the laser emission, the fiber dispersion as well as the timing jitter.

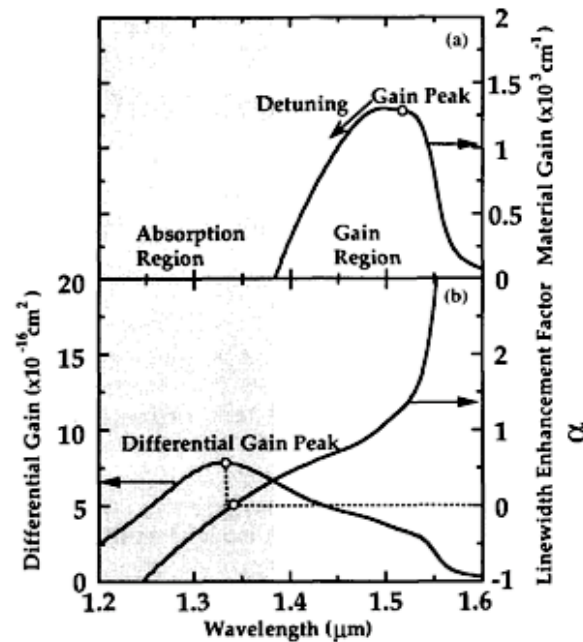


Figure 3.13: Calculated dependencies of material gain, differential gain and  $\alpha_H$ -factor on wavelength in a typical QW laser

### 3.6.1 Power Limitation

The power available is expressed as the ration of the power launched into the fiber  $P_L$  and the minimum power required by the receiver  $P_R$  to maintain a certain bit-error ration (BER). An optical fiber communication system will be limited by the power to a length such as:

$$L_{max} = \frac{P_L - P_R - M}{\alpha} \quad (3.38)$$

where  $M$  is the margin to accommodate, for example, component variations with time and temperature,  $\alpha$  is the fiber loss (in dB/km) and  $P_L$ ,  $P_R$  are expressed in dBm. The power limit can be improved by increasing the power of optical pulses emitted by the laser, by improving the receiver sensitivity, by improving the laser and fiber coupling efficiencies and by reducing the fiber loss.

However increasing the laser power can result in a higher nonlinear gain effects in the laser (limitation of the maximum propagation distance, of the bit error rate,) and in enhanced nonlinear propagation of laser pulsed through the fiber. When the power gets higher into the fiber, it cannot be assumed to behave as a linear transmission medium. The nonlinear refractive index in the fiber results in self-phase modulation of laser pulsed which in turn leads to the distortion of their temporal profile and optical spectrum. At higher peak powers, transmitted can even break up sub-pulses due to modulational instability in the optical fibers.

### 3.6.2 Dispersion Limitation

The dispersion limitation will occur when the pulse spreading causes adjacent pulses to overlap so that errors result (inter-symbol interference). It is well-known that the pulsewidth increases with distance due to dispersion. For a system operating at rate  $B$ , the dispersion limited length would be:

$$L_{max}^D = \frac{1}{2BD\Delta\lambda} \quad (3.39)$$

where  $D$  is the dispersion parameter of the fiber (in ps/km/nm) and  $\Delta\lambda$  is the spectral bandwidth of the laser pulses. The dispersion limit can be improved by reducing the laser chirp by operating at zero-dispersion wavelength of the fiber. The importance of the chirping-induced performance degradation increases with the increase of the transmission bit rate  $B$  and can ultimately limit achievable system performance. Penalties in the system due to laser chirping and GVD (Group Velocity Dispersion) effects in the fiber arise because the power in the initial part of the pulse moves into the previous bit period after a long length of fiber; similarly the power at turn off moves into the following bit interval. The power penalty in a communication system can be analyzed by considering the migration of optical power out of bit interval or by using the eye diagram closure. The power penalty due to laser chirping can be expressed as follows:

$$P_{dB} = 10 \log \left( \frac{1}{1 - 4LBD\Delta\lambda} \right) \quad (3.40)$$

In order to obtain a low penalty, the laser chirp  $\Delta\lambda$  must be minimized. The influence of linear fiber dispersion may be minimized by operating at the zero dispersion wavelength. However dispersion is not eliminated completely since higher order dispersion terms in fibers are not zero. The second-order GVD results in the asymmetric spreading of an optical pulse generating a tail at the trailing edge of the pulse. It was demonstrated that the second-order GVD may limit the transmission distance at data rates approaching 50 Gbps. At these data rates, the modulation bandwidth is so large that even for ideal transform-limited pulses fiber dispersion significantly broadens the pulses and limits the transmission distance.

### 3.6.3 Timing Jitter Limitation

The performance of high-speed transmissions are also limited by the pulse timing jitter. This jitter may result in power penalties or enhanced BER floors. If the timing jitter is large enough, additional errors originate from the uncertainty in a pulse position over a significant fraction of the bit period. The origin of the power penalty due to jitter can be explained through the turn-on and turn-off fluctuations of optical pulses. Thus, different portions of the received waveform are sampled from bit to bit. Resulting signal fluctuations generate additional noise and lead to the degradation of the signal-to-noise ratio. To maintain the same level of the signal-to-noise ratio, the average received power should be increased. It

has been shown that the exact amount of jitter-induced power penalty depends on the fiber length and on the increase of the bit rate  $B$ . Calculations have shown that the power penalty remains small ( $<0.5$ dB at the  $10^{-9}$  BER level) as long as the bit-rate-jitter product  $B\delta T$  is less than 0.06 to 0.15. However for  $B\delta T > 0.15$ , the jitter-induced power penalty increases dramatically up to 10-dB level. A power penalty of 0.7 and 3.2 dB at the  $10^{-9}$  BER level has been measured for a pseudo-random modulation at a 1.2 Gbps and an rms timing jitter of 41 to 60 ps. In addition, the BER performance at the  $10^{-11}$  level cannot be reached for laser pulses with a rms jitter over 50 ps at the same encoding data. For bit rates greater than 2 Gbps, a laser source must have  $\delta T$  below 30 ps to avoid large power penalty.



# Chapter 4

## Gain and Q-Switching in Semiconductor Lasers

Gain and Q-switching of laser diodes by fast switching the optical gain or the intra-cavity loss is a simple technique for producing optical pulses with high repetition rates and high peak power. Gain switching relies upon the switching of the optical gain through the modulation of the driving current while Q-switching variations of optical loss through passive or active means are required. An advantage of gain and Q-switching over mode locking is that the repetition rate of output pulses in GHz range can be varied by changing the driving conditions. Also, Q-switching allows the generation of picosecond pulses with peak power that exceeds by a few orders of magnitude that of gain-switched and mode-locked pulses.

### 4.1 Gain Switching

#### 4.1.1 Principle of Operation

In contrast to mode-locking and Q-switching techniques, gain switching has the advantage that no external cavity and no sophisticated fabrication technology are required. The idea of gain switching originated from observations of relaxation oscillations when turning on a laser diode from below threshold using electrical pulses with a fast leading edge. It was noticed that the optical pulsewidth was considerably shorter than the electrical pulse. Basically, gain switching consists of exciting the first spike of relaxation oscillation and terminating the electrical pulse before the onset of the next spikes. It means that the electrical pulsewidth should be shorter and should lie in the picosecond and nanosecond time range. The generation of ultrashort light pulses by a gain switched diode is illustrated in figure 4.1. The dc bias

and pulsed current are assumed to be applied on the laser (a).  $I_0$  can be below or above threshold. Below the threshold, lasing does not occur until the electric pulse increases the injected current above the threshold density (b). Above the threshold the carrier density reaches  $N_i$ . Then lasing occurs and represses the increase in carrier density and consequently  $n(t)$  is pulled down to  $N_f$ .

The simplest analysis of basic phenomena in a semiconductor laser of the generation of gain-switched pulses can be carried out by the rate equations that connect the photon density  $S$  in the cavity with the carrier density  $N$ . They can be written for example as follows:

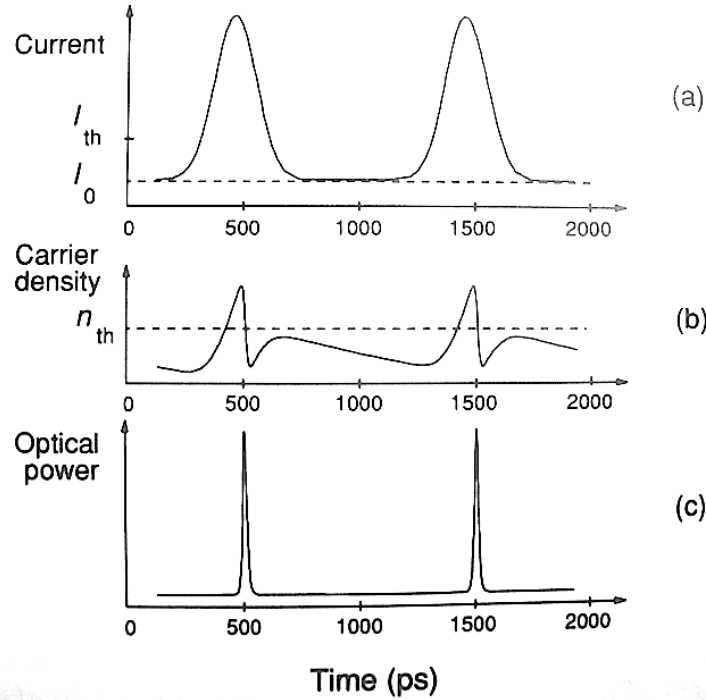


Figure 4.1: Illustration of Gain-switching: (a) the applied current, (b) the carrier density, and (c) output pulses

$$\frac{dN}{dt} = \frac{I(t)}{eV} - \frac{N(t)}{\tau_e} - g_0(N - N_t)S \quad (4.1)$$

$$\frac{dS}{dt} = \Gamma g_0(N - N_t)S - \frac{S}{\tau_p} + \frac{\beta \Gamma N}{\tau_e} \quad (4.2)$$

where  $N_t$  is the transparency density,  $g_0$  is the differential gain,  $\beta$  is the spontaneous coupling factor,  $e$  is the electron charge,  $d$  is the active layer thickness,  $I(t)$  is the current,  $\Gamma$  is the confinement factor and  $\tau_e$ ,  $\tau_p$  are the carriers and photon lifetimes. In (4.1) and (4.2), the gain is assumed to be proportional to the carrier concentration. These simple equations are single-mode that is they do not take into account the distribution of  $S$  between cavity

modes. However, they can be easily written for the multimode case. The rate equations are suitable for the simple treatment of all techniques of generating ultra-short light pulses, including gain and Q-switching as well as mode-locking of laser diodes. For gain-switching the current is taken as a train of short electric pulses. For the generation of ultra-short pulses, the differential gain  $g_0$  and the photon lifetime  $\tau_p = \frac{1}{v_g(\alpha_i + \alpha_m)}$  (with  $v_g$  the group velocity,  $\alpha_m$  and  $\alpha_i$  the mirror and internal loss) play a significant role.

### 4.1.2 Pulsewidth and Peak Power

The gain-switched pulse can be described as a combination of two exponential curves with time constant  $\tau_r$  on the rising edge of  $S(t)$  and  $\tau_f$  on the trailing edge. According to (4.2), for a small enough value of  $S$ , gain compression can be neglected and  $S(t)$  will increase exponentially as a result of stimulated emission:

$$\frac{1}{S} \frac{dS}{dt} = \Gamma g_0 (N - N_{th}) = \frac{1}{\tau_r} \quad (4.3)$$

The trailing edge of the optical pulse also exhibits an exponential decay constant and normally we have  $\tau_f \approx \tau_r$ . The FWHM of the pulse can be roughly estimated by the sum  $\tau_r + \tau_f$ . The pulse duration is limited by the rate of energy transfer between electron and photon populations. Using (4.3) one can deduce that  $\tau_r \approx \frac{eV}{Qg_0\Gamma}$  which means that the risetime of the pulse is inversely proportional to the net charge  $Q$  transferred to the active volume by the electrical pulse. The decay time  $\tau_f$  depends on how far down below threshold the carrier density is pulled during the optical pulse. One can deduce from (4.3) a corresponding improvement in the temporal response of gain-switched pulses if the differential gain  $g_0$  gets larger. In case of short driving pulses such as  $I(t) = N_i \delta(t)$  with  $\delta(t)$  the Dirac's function and for  $N_i \gg N_{th}$ , the pulsewidth of a gain-switched pulse is approximately given by:

$$\Delta\tau = \tau_p + \frac{1}{g_0 N_i} \quad (4.4)$$

Figure 4.2 illustrates the computer simulation of a typical optical response for a gain-switched laser. The main parameter that affects the pulsewidth and the peak power is the initial inversion  $N_i$ . It can be shown that  $N_i$  depends on the bias current  $I_0$  and increases with the increase of the ratio  $I_1/I_{th}$  (with  $I(t) = I_0 + I_1 \sin \omega t$ ). The maximum achievable initial inversion is limited by the fundamental parameters of the laser such as the differential gain, the spontaneous emission factor and the cavity loss. It should be noted that when the laser is driven well above the threshold  $I_1/I_{th} \gg 1$  or if electrical pulses are long, multiple optical pulses are generated within a period of the modulation current. Figure 4.3 shows the calculated peak power and pulsewidth versus the amplitude of electrical pulses. The CW threshold current is 20 mA. The maximum value of the ratio  $I_1/I_{th}$  is less than 8. Above

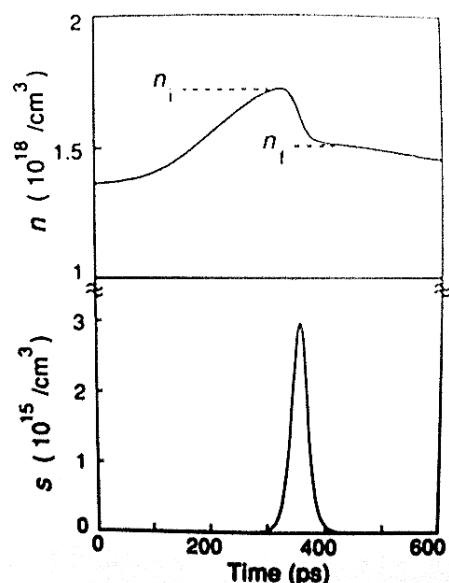


Figure 4.2: Calculated carrier density and photon density against time in a gain-switched laser

this value the double-pulse generation occurs. The pulse repetition rate is 1 GHz. It is seen that the peak power increases while the pulsewidth decreases for higher current amplitudes. A typical pulsewidth lies in the range of 20 to 30 ps.

Figure 4.4 shows the parameter of gain-switched pulses a function of the dc bias  $I_0$ . The

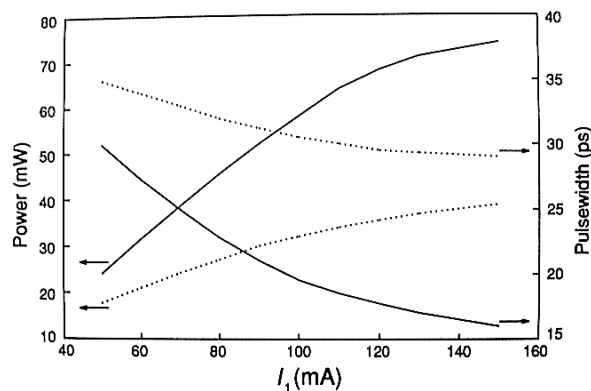


Figure 4.3: Dependence of the peak power and pulsewidth on the amplitude of current pulses. DC bias current is 15 mA. The nonlinear gain coefficient is 0 (solid lines) and  $1.5 \cdot 10^{-17} \text{ cm}^3$

pulse repetition rate is again 1GHz. For a given drive pulse, there is an optimum dc bias level for which the FWHM is minimized. This level is below the threshold current. Thus, the difference between the threshold and the optimum bias decreases as the pulsewidth of electrical pulses and becomes zero for extremely short driving pulses. This fact is consistent

with the experiments. When the laser is biased below this optimum level, the pulses broaden and the peak power decreases with the dc bias. At the same time optical pulses are emitted with progressively longer delay times. It is important to note that both the peak power and

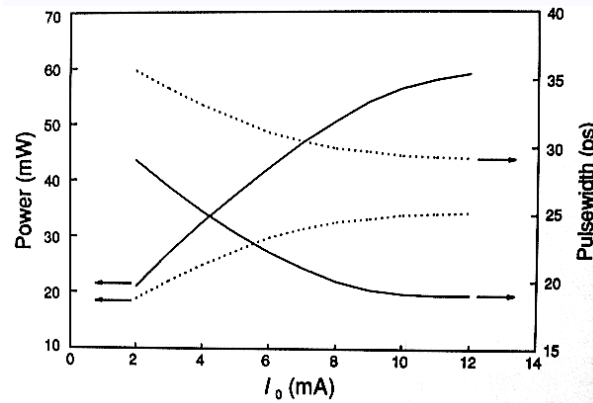


Figure 4.4: Calculated peak power and pulsewidth versus the DC bias.  $I_1$  is 100 mA. The nonlinear gain coefficient is 0 (solid lines) and  $1.5 \cdot 10^{-17} \text{ cm}^3$

the pulsewidth exhibit strong influences of the gain compression. To illustrate this, the peak power and the pulsewidth are plotted in figure 4.5 versus the non-linear gain coefficient. The DC bias is 10 mA, the driving current amplitude is 150 mA, and the repetition rate is 1 GHz. The peak power decreases and the pulsewidth increases with the increase of the nonlinear gain coefficient. This fact is very important because the nonlinear gain sets the limit for the minimum achievable pulsewidth and the maximum achievable peak power of gain-switched pulses. Gain-switched pulses can also be improved with the increase of the differential gain coefficient. Increasing  $g_0$  has a twofold effect on the device: first, the pulsewidth decreases gradually for higher  $g_0$ ; secondly, the peak power increases at the same time. This originated from the fact that initial inversion  $N_i$  is higher for higher  $g_0$ . As a result, QW lasers are more promising for gain-switching because of their enhanced differential gain as compared to bulk lasers.

### 4.1.3 Optical Spectra and Frequency Chirping

The optical bandwidth of picosecond pulses is a key-parameter for gain-switched lasers. The analysis of the generation of the gain-switched lasers was presented via the rate equations for a single-mode laser. However, for gain-switched lasers, many longitudinal modes of the laser cavity may be excited as a consequence of the dynamic overshoot of electron concentration. This can occur even if the laser emission is single-mode under CW operating conditions. In Fabry-Perot gain-switched lasers, the optical spectra consists of several (typically 5 to 10)

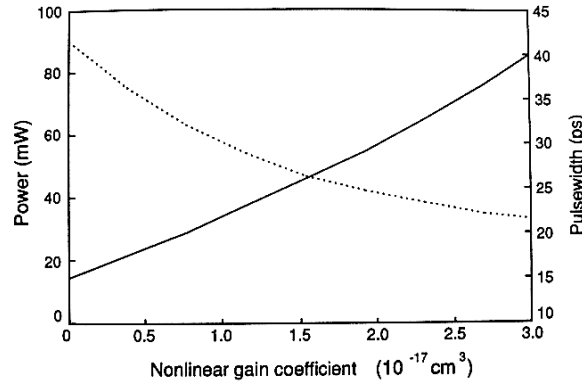


Figure 4.5: Dependence of peak power (dashed line) and pulsewidth (solid line) on the nonlinear gain coefficient

longitudinal modes. A typical optical spectrum is shown in figure 4.6: the number of excited modes depends on the device structure (index- or gain-guided), the spontaneous emission factor, pumping conditions (current amplitudes  $I_0$  and  $I_1$ ), and modulation frequency. When several modes oscillate in the laser, the rate equations (4.1) and (4.2) have to be replaced by:

$$\frac{dN}{dt} = \frac{I(t)}{eV} - \frac{N(t)}{\tau_e} - \sum_m g_m S_m \quad (4.5)$$

$$\frac{dS_m}{dt} = \Gamma g_m S_m - \frac{S_m}{\tau_p} + \frac{\beta \Gamma N D_m}{\tau_e} \quad (4.6)$$

where  $g_m = g_0(D_m N - N_t)$ ;  $S_m$  is the photon density in the  $m$ th laser mode and  $D_m$  is the lineshape factor which is defined such as,

$$D_m = \frac{\delta\lambda/(\pi\Delta\lambda_g)}{1 + [(\lambda_m - \lambda_0)/\Delta\lambda_g]^2} \quad (4.7)$$

where  $\delta\lambda$  is the longitudinal mode spacing,  $\Delta\lambda_g$  is the gain bandwidth, and  $\lambda_0$  and  $\lambda_m$  are the wavelengths of the central and  $m$ th laser mode. The net photon density equals  $S(t) = \sum_m S_m$ . In addition to multimode operation, the spectral line of each mode is broadened. If a single-frequency laser diode is used for gain-switching, the multimode operation can be avoided. However the bandwidth under gain-switching usually exceeds the bandwidth under CW operating conditions as shown in figure 4.6. The time dependence of the laser wavelength is related to the time dependence of the carrier concentration due to the effects of free-carriers on the refractive index of the semiconductor material. The instantaneous wavelength is related to the refractive index as:

$$\lambda(t) = \frac{n(t)}{n_0} \lambda_0 \quad (4.8)$$

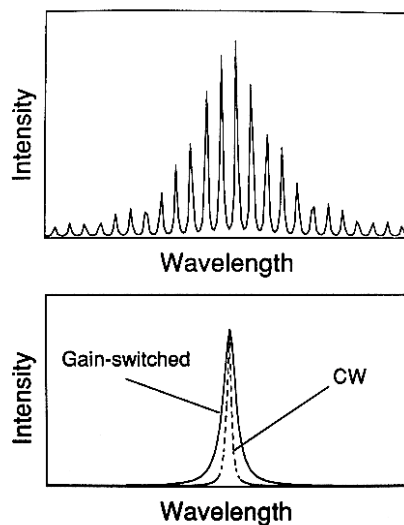


Figure 4.6: Typical spectra of (a) a FP gain-switched laser and (b) a single-mode laser under gain switching (solid line) and under CW operating conditions

where  $n(t)$  and  $n_0$  are the refractive indices at times  $t$  and 0. Free-carrier plasma refraction, band-gap shrinkage and the dynamic Burstein-Moss shift (modification of the interband absorption from free carriers at high doping levels) are the principal mechanisms by which the carrier concentration affects the refractive index. Although carrier-induced refractive index changes depend on a number of factors, and the exact expression of  $n$  as a function of carrier density is very complicated, one can write for simplicity,

$$n(t) \approx \frac{dn}{dN} N(t) \quad (4.9)$$

A typical value of  $dn/dN$  is  $-2.3 \cdot 10^{-20} \text{ cm}^3$  for InGaAsP lasers. Combining (4.8) and (4.9) one obtains for the wavelength chirp  $\Delta\lambda$  during the gain-switched pulse,

$$\Delta\lambda \approx \frac{dn}{dN} \frac{\lambda_0}{n_0} \Delta N(t) \quad (4.10)$$

with  $\Delta N = N_i - N_f$ . Because  $dn/dN < 0$ , the wavelength shifts towards longer wavelengths (red-shift). In accordant with (4.10), the estimated linewidth broadening for gain-switched pulses is typically 0.2-0.3 nm.

Due to the wavelength chirp, gain-switched pulses have a time-bandwidth product  $\Delta\tau\Delta\nu$  that is normally far from the theoretical limit for bandwidth-limited pulses. Thus, the time-bandwidth product of optical pulses is given by,

$$\Delta\tau\Delta\nu = K(1 + \alpha_H^2)^{1/2} \quad (4.11)$$

with  $\alpha_H$  the linewidth enhancement factor (see chapter 2) and  $K$  the constant that is different for different pulse shapes. The wavelength chirp has been found to increase when the optical

pulsewidth decreases in gain-switched lasers. Computer simulations of the laser dynamics indicate that there is an optimum electrical pulse duration ( $\approx 150$  ps) for which the product  $\Delta\tau\Delta\nu$  has a minimum value. Since the frequency chirp results from variations of the carrier density, it is observed both in single-frequency and multimodes lasers. The chirping depending on the modulation of the carrier density spatially averaged over the optical mode, it is expected that the chirp varies significantly in different laser structures (gain- or index-guided for instance). A good spatial overlap of the optical mode and the carrier density is expected to reduce the frequency chirping.

## 4.2 Q-Switching in Laser Diodes

### 4.2.1 Active Q-Switching

Actively Q-switched is not widely used as both gain-switched and mode-locked lasers. The intracavity loss is modulated electrically or optically in a laser under active Q-switching. A typical actively Q-switched laser diode is a multiple contact laser, and it often consists of two or three sections (a gain section, a modulator section, and a passive waveguide section in-between). Since the modulator section and the gain section are fabricated monolithically and have exactly the same material composition, the band-gap in the gain section must be shifted to lower energies to prevent band-to-band absorption and to increase the modulation effectiveness. The time evolution of loss, inversion and optical pulses in an actively Q-switched laser is depicted in figure 4.7. The modulation of loss is realized by shifting the band edge in the modulator section using the Franz-Keldysh effect or the quantum confined Stark effect in MQW lasers that is caused by the applied electric field.

**Note:** When an electric field is applied, the electron and hole wavefunctions become Airy functions rather than plane waves. The Airy function includes a tail which extends into the classically-forbidden band gap. According to Fermi's Golden Rule, the more overlap there is between the wavefunctions of a free electron and a hole, the stronger the optical absorption will be. The Airy tails slightly overlap even if the electron and hole are at slightly different potentials (slightly different physical locations along the field). The absorption spectrum now includes a tail at energies below the band gap and some oscillations above it. This explanation does, however, omit the effects of excitons, which may dominate optical properties near the band gap. The Franz-Keldysh effect occurs in uniform, bulk semiconductors, unlike the quantum confined Stark effect, which requires a quantum well.

The absorption spectrum of MQW exhibits an enhanced absorption at the band edge. This is caused by excitons whose binding energy is enhanced by the carrier confinement. The exciton

absorption peak shifts to lower energies when an electric field is applied to the quantum wells. This effect is much larger than the Franz-Keldysh effect in bulk materials. It can

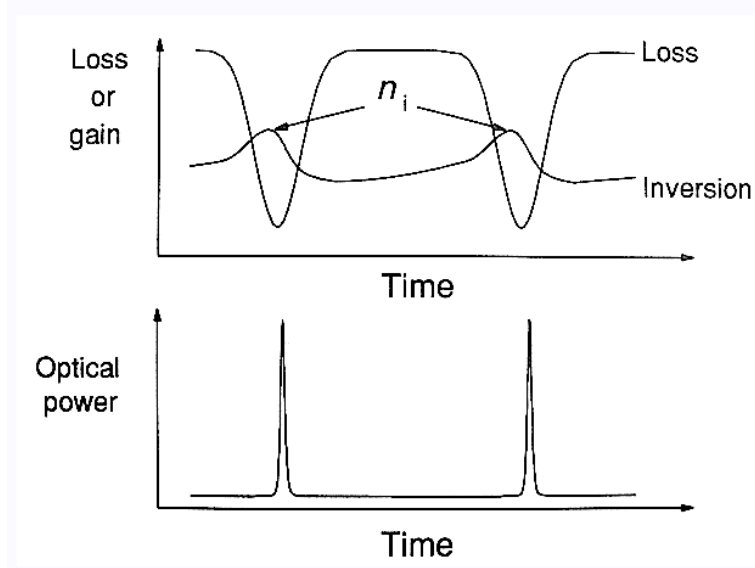


Figure 4.7: Active Q-switching: evolution of loss/gain, carrier density, and optical power.  $N_i$  is the initial carrier density just before the pulse emission

be shown that the Q-switched pulse parameters are drastically dependent on the photon lifetime  $\tau_p$  and on the initial inversion level  $N_i$ . One can deduce this by considering the rate equations (4.1) and (4.2). When the ultrashort pulse is emitted, stimulated emission is the dominant mechanism and the contribution of all other processes, including spontaneous emission, carrier pumping and recombination are negligible. Thus, based on rate equations the relation between carrier and photon densities in the laser cavity can be written such as:

$$S(t) = N_i - N(t) - [1/(g_0\tau_p)] - \ln[(N_i - N_t)/(N(t) - N_t)] \quad (4.12)$$

Introducing the inversion  $r$  and the energy extraction efficiency  $\eta$ , the peak power of the Q-switched pulse is given by,

$$S_0 = \left( \frac{1}{g_0\tau_p} \right) (r - 1 - \ln r) \quad (4.13)$$

The pulsewidth of the pulse is,

$$\tau_Q = \frac{r\eta\tau_p}{(r - 1 - \ln r)} \quad (4.14)$$

Equations (4.13) and (4.14) show that to get shorter pulses, the initial inversion should be higher whereas the photon lifetime should be lower. For instance for  $r = 1.1$ , the pulsewidth  $\tau_Q$  is about  $50\tau_p$  and  $\tau_Q \approx 5\tau_p$  for  $r = 2.0$ . Also, it is important to stress that high-power actively Q-switched laser diode can suffer from gain compression via an asymmetry in the pulse shape. Values of  $\tau_Q$  in the range of 20 to 60 ps can be obtained.

### 4.2.2 Passive Q-Switching

Passive Q-switching is one of the simplest techniques for generating picosecond pulses in laser diodes. Similar to actively Q-switched, passively Q-switched lasers are always multi-contact diodes. A saturable absorber located in the laser cavity is responsible for the generation of ultrashort pulses in such devices. The fundamental difference between the two techniques is that as compared to active Q-switching no external electrical or optical modulation is required to produce ultrashort optical pulses. In the case of active Q-switching, the pulse repetition frequency is set by an external RF or optical signal, whereas for passive Q-switching, the frequency is governed by the laser parameters and pumping conditions. The action of a saturable absorber is depicted in figure 4.8. As a result of the nonlinear transmission characteristics of the absorber, the initial amplitude distribution of the light is distorted when a light beam is passed through it. The passage of a light pulse leads to a pulse shaping, as shown in figure 4.8. The absorption of the leading edge of the pulse is increased as compared with the trailing one. This results in the pulse shortening and leads to generation of asymmetric pulses. The unpumped segments of a laser diode or sections with a low pumping rate

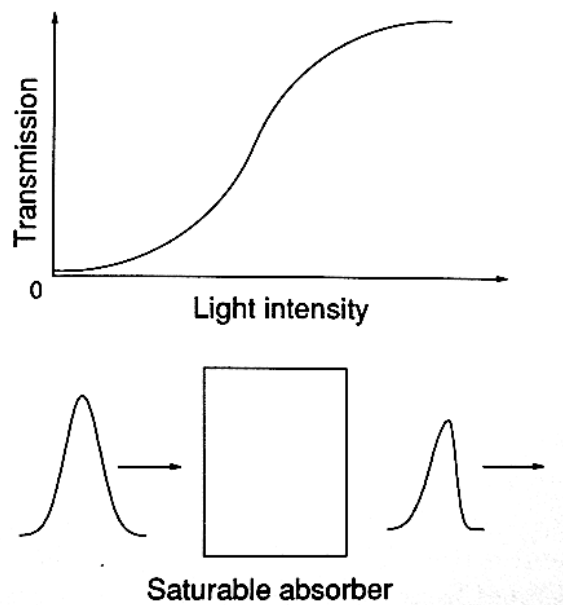


Figure 4.8: Typical transmission characteristic of a saturable absorber and an illustration of the pulse shaping by the absorber

in a multiple-contact laser act as a saturable absorber. To generate self-sustained pulsations or self-Q-switched pulses, the saturable absorber in the laser cavity must satisfy a number of conditions. The most important parameters that affect the dynamic behavior of the laser are the ratio of the differential loss  $da/dN$  of the absorber to the differential gain  $dg/dN$  of

the amplifier section and the ratio of the carrier lifetime in the gain  $\tau_g$  and the absorber  $\tau_a$  sections. It can be shown that the following conditions are required for the generation of Q-switched ultrashort optical pulses:

$$\frac{da/dN}{dg/dN} > 1 \quad (4.15)$$

and,

$$\frac{\tau_a}{\tau_g} > 1 \quad (4.16)$$

Owing to specific dependence of gain/absorption on the carrier concentration, the values of  $da/dN$  and  $dg/dN$  can be controlled by using different current input applied to different sections of the laser. As a result, the pulsewidth, the peak power and the repetition rate are dependent on the driving current. Ranges of parameters  $da/dN$ ,  $dg/dN$ ,  $\tau_g$  and  $\tau_a$  can be calculated using the simple rate equations. In early experimental studies, relatively long 30- to 100 ps pulses at repetition rate up to 3 to 5 GHz were generated with passively Q-switched lasers. Typical values of pulse peak power are in the range from 0.1 to 1W. The pulse parameters are dependent on the photon lifetime  $\tau_p$  and the absorber recovery rate on carrier lifetime  $\tau_a$ . The recovery of the absorber is due to spontaneous recombination of excited electron-hole pairs. Let us note that the location of the absorber section at the middle between the gain regions and the application of the reverse bias on the absorber allows to improve the pulse parameters that are generated by three-section lasers as compared to the two-section ones. This improvement can be explained by a significant decrease in the absorber recovery time.

### 4.2.3 Optical Spectra

Similar to gain-switched lasers, many longitudinal modes of a laser diode cavity may be excited in Q-Switched lasers as a consequence of the dynamic overshoot of electron concentration and the variation of carrier density during the emission of optical pulses. In Fabry-Perot self-Q-switched lasers, typical optical spectra consist of several longitudinal modes. A typical optical spectrum of a Q-switched Fabry-Perot laser is very similar to that of a gain-switched laser. Self-Q-switched lasers normally have a spectral bandwidth as wide as 3 to 5 nm and generate picosecond pulses with a time-bandwidth product  $\Delta\tau\Delta\nu$  that exceeds by several times that for bandwidth limited pulses.

To reduce the spectral bandwidth of Q-switched pulses, single-frequency lasers (including DFB and DBR) should be used. The generation of bandwidth-limited high-power Q-switched pulses was reported using a multi-sections DFB InGaAsP lasers. The optical spectrum of Q-switched pulses is shown in figure 4.9. The lasing wavelength is 1503 nm and the bandwidth

is roughly 0.18 nm (FWHM). The wavelength of Q-switched pulses was shifted by approximately 2 nm to achieve a shorter wavelength as compared to the wavelength under the CW operation of the same device. The spectrum exhibits an asymmetric shape with a residual tail to shorter wavelengths. Both temporal and spectral shapes of Q-switched pulses are very similar to those of gain-switched pulses generated with multi-sections DFB lasers. The time bandwidth product was measured to be 0.24. Taking into account the experimental error, this value agrees with the time-bandwidth product for Fourier-limited asymmetric pulses.

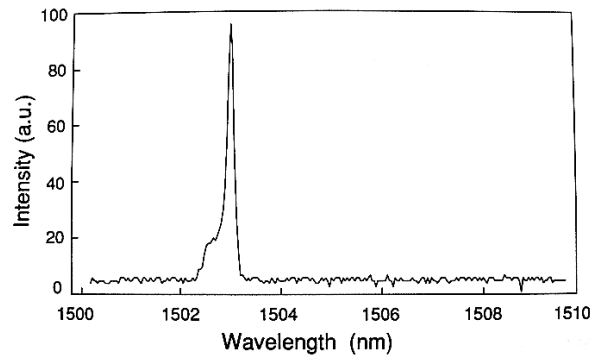


Figure 4.9: Typical optical spectrum of a Q-switched multi-section DFB laser

# Chapter 5

## Mode-Locked Semiconductor Lasers

The basic advantage of mode locking is that it generates much shorter pulses as compared to gain or Q-switching. Mode-locking can be realized using a number of techniques mostly including active, passive and hybrid methods. A laser runs at wavelengths dictated by two major factors. The first is the bandwidth of the gain medium, and the second is the wavelength range dictated by the cavity is not continuous, it is divided up into cavity modes where the spacing between each mode is determined by the cavity length. A single-mode laser will lase on only one of these longitudinal cavity modes while a multimode laser operates on multiple cavity modes. If the phase between each cavity mode is not well-defined, then the output of the laser will be continuous and noisy. If it lases on an enormous number of modes, then through averaging it becomes quiet again. The process of mode-locking defines the phase between each mode. Mode-locking is achieved by changing the Q-factor of the cavity periodically at a harmonic of the frequency determined by the roundtrip time of the cavity (mode-spacing). This periodic change of the cavity Q can be accomplished either by passive or active means and causes the laser output to be pulsed at the roundtrip time of the cavity. In the case of active mode-locking, an optical device is placed in the cavity whose transmission can be rapidly modulated through external electronics. Passive mode-locking schemes are accomplished by placing a material with non-linear response in the cavity. This material can be a saturable absorber, or it can exhibit a nonlinearity that changes the intracavity propagation properties of the beam (Kerr Lens mode-locking). Thus, the laser will naturally begin to output pulses when all of the modes are in phase and constructively interfere to produce pulses.

## 5.1 Principle of Operation

The generation of ultrashort pulses is based on the confinement of the energy in a laser cavity into a small spatial region. The laser emission consists of a set of resonator modes  $\omega_m$  (with  $m=1,2,3,\dots$ ) separated by  $\delta\omega$ . The number of modes that oscillate is limited by the spectral bandwidth  $\Delta\omega_g$  over which the gain exceeds the cavity loss. The output can be seen as a sum of frequency components that correspond to oscillating modes. The electric field can be written such as:

$$E(t) = \sum_m A_m \exp j[(\omega_0 + m\delta\omega)t + \Phi_m] \quad (5.1)$$

Equation (5.1) does not consider the spatial distribution of the electrical field. The amplitude and the phase of the  $m$ th mode are denoted  $A_m$  and  $\Phi_m$  respectively. In general, relative phases between the modes are randomly fluctuating. If nothing fixes the phase  $\Phi_m$ , the laser output will vary randomly in time, the average power being approximatively equal to the simultaneous one. However, if the modes are forced to maintain a fixed phase and amplitude relationship

$$\Phi_m - \Phi_{m-1} = \delta\Phi \quad (5.2)$$

$$A_m e^{j\Phi_m} = A_0 e^{j(\Phi_0 + m\delta\Phi)} \quad (5.3)$$

then the output of the laser will be a periodic function of time:

$$E(t) = A_0 \left( \frac{\sin[(k+1)\delta\omega t_1/2]}{\sin[\delta\omega t_1/2]} \right) e^{i\omega_0 t} \quad (5.4)$$

where  $k$  is the number of locked modes and  $t_1 = t + \delta\Phi/\delta\omega$ . Figure 5.1 illustrates the envelope  $E^2(t)$  for  $k=10$ . The operating conditions given in the equations written above result in the generation of a train of regularly spaced optical pulses. This dynamic regime is named mode-locking. The pulses have a width  $\Delta\tau$  which is proportional to  $1/\Delta\omega_g$ . The pulse train has a periodicity of  $T = 2nL/c$ . The ratio of the period  $T$  to the pulsewidth  $\Delta\tau$  is equal to the number of locked modes  $k$ .

## 5.2 Active Mode-Locking

Active-mode locking is achieved by modulating the loss or gain of a laser diode at a frequency that is equal to the inter-modal spacing  $\delta\nu$ . In this case, each spectral mode is driven by the modulation sidebands of its neighbors. Thus, phases of modes are locked by the external modulation. Active mode-locking is schematically illustrated in figure 5.2. The modulation of the gain in the laser at the intermodal spacing frequency results either from modulating the driving current or using an external modulator. Sine wave oscillators are normally used for the current modulation. Alternatively ultrashort electrical pulses from a comb generator can be

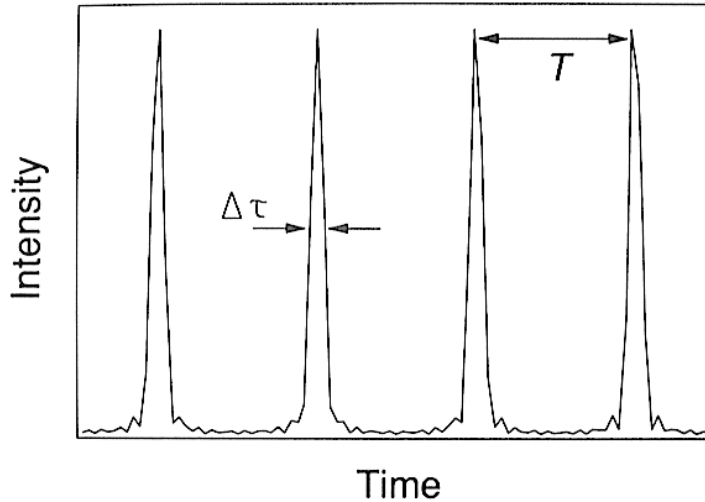


Figure 5.1: Ideal mode-locking: the output of a laser with 10 completely locked modes

used. The modulation is often superimposed on a dc bias  $I_0$ . The current modulation causes the modulation of the carrier density around the threshold value  $n_{th}$ . Both the amplitude  $I_1$  of the current modulation and  $I_0$  are chosen to create a very short time window of net gain in the laser. This implied that the carrier density  $n(t)$  exceeds  $n_{th}$  for a very short period of time during each modulation period. Due to the finite carrier lifetime there exists a phase difference between the electron response and the applied current modulation. The carrier density is a periodical function of time but it consists of a set of harmonics of the modulation frequency  $2\pi/T$ . The most strongly excited Fourier component of the carrier density is the fundamental at  $2\pi/T$ , the harmonics of order  $m$  being reduced by approximately a factor of  $1/m$ . Mode-locking is ultimate provided the period of modulation  $T$  is exactly equal to the roundtrip time of the laser cavity,

$$T = \frac{1}{\delta\nu} \quad (5.5)$$

Generally this will result with an intermodal spacing in the range of 0.3 and 20 GHz. This distinguishes active mode-locking from gain-switched lasers where the pulse frequency is not related to the cavity length of the laser. Fundamentally when the loss is less than the gain it creates an optical window that allows the optical pulse to exit the system and emit from the laser. An example of an actively mode-locked laser is shown in figure 5.3 where the laser feeds into an Acousto-Optic-Modulator (AOM), which behaves as the optical window for the pulses. Active mode-locking is difficult to control because of all of the variables involved. These variables include the placement of a standing wave acousto-optic modulator inside the laser cavity, the placement of a modulation device inside the laser cavity to induce a frequency shift based upon electro-optic effects, and/or the modulation of the energy source pumping

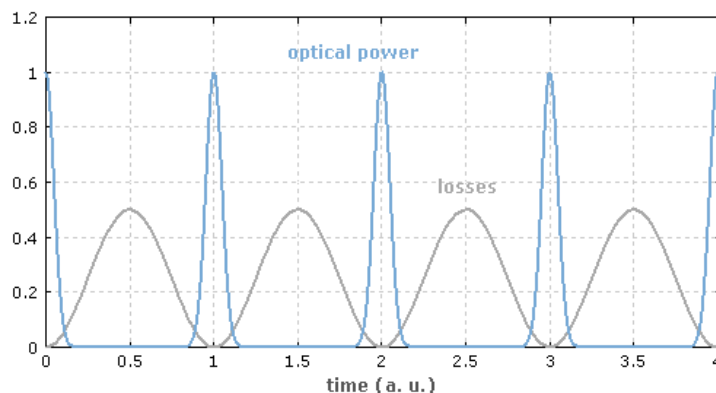


Figure 5.2: Generation of optical pulses by active mode-locking of a laser diode

the laser itself. When using external optical sources, free space optics makes coupling into the laser difficult and optical modulators also reduce efficiency. Loss make it difficult to control the mode-locking due to the presence of such a weak signal. Another major disadvantage of the active mode-locking technique is its dependence on the external modulation rate. The pulse rate is limited to the speed of the signal generator and cannot surpass it. In order to create pulses faster than the electronic signal generator, the laser needs to be configured in such a way that it can generate the desired pulses on its own. A design that creates a self-pulsating laser within a self-contained system without the use of external optics is the passive mode-locking configuration of a laser diode.

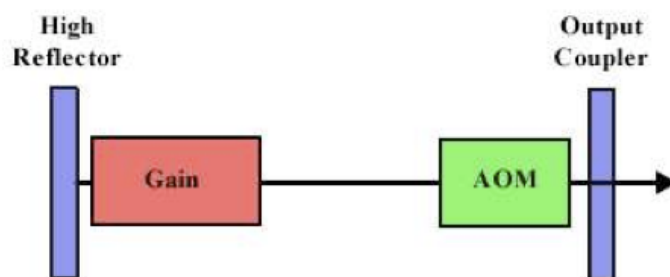


Figure 5.3: An example of an actively mode-locked laser employing an acousto-optic-modulator (AOM)

### 5.3 Passive-Mode Locking

Passive mode-locking harnesses the time dependences of the gain and loss saturation energies to create the desired pulses. By creating very small regions where the gain of the laser is

greater than its losses, ultra-fast pulses can be produced. When the losses in a laser are greater than the gain, it would appear as if the laser is off. This is because there is not enough energy to create the stimulated emission required for lasing. It is said that the net gain is zero because there is no positive gain. It is very important that as the loss and gain approach their steady-state values, that the loss remains larger than the gain in the regions where pulse generation is not desired. Once the gain is slightly greater than the losses, resulting in net gain, there will be enough energy to cause the laser to turn on and emit light. The key to creating pulses in the passive mode-locked laser is to control the region in which there is net gain. Implementing a saturable absorber into the system can control the amount of loss as a function of power such that the peak of the pulse that has spontaneously formed will see very little loss relative to the wings of the pulse. The saturable absorber is a region in the laser diode where the amount of loss can be controlled by controlling the reverse bias applied. The main purpose of the saturable absorber is to create a region in which the pulse will be shaped. This region will be able to pull in the wings of the broad pulse and create a thinner pulse while maintaining the same average power. If the recovery time of the saturable absorber is much longer with respect to the duration of the pulses then it is called a slow absorber. Otherwise, the absorber is commonly referred to as a fast absorber. Figures 5.4 and 5.5 show the generation of an optical pulse while displaying the gain and loss saturation energies for a fast and slow absorber, respectively. The action of the saturable absorber can

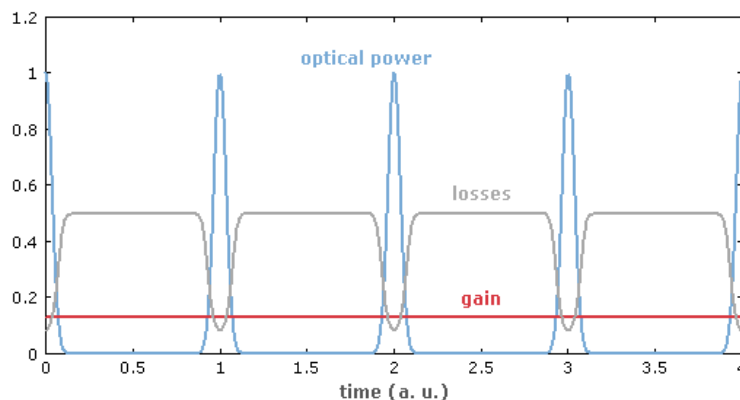


Figure 5.4: An example of a passively mode-locked laser with a fast saturable absorber

be described by the rate equation for absorber carrier density:

$$\frac{\partial n}{\partial t} = -\frac{n - n_e}{\tau_a} - \frac{1}{E_s^a} n |v(t)|^2 \quad (5.6)$$

where  $n_e$  is the equilibrium carrier density,  $E_s^a$  is the saturation energy of the absorber and  $v(t)$  is the pulse envelope. For a slow saturable absorber, the first term on the right-hand

side can be neglected and one obtains:

$$\frac{\partial n}{\partial t} = -\frac{1}{E_s^a} n |v(t)|^2 \quad (5.7)$$

A saturable absorber is called a slow saturable absorber if its recovery time is much longer as compared with duration of pulses produced in the laser that is  $\Delta\tau \ll \tau_a$ . If  $\Delta\tau \gg \tau_a$ , the absorber is a fast saturable absorber. The solution of (5.7) can be written such as:

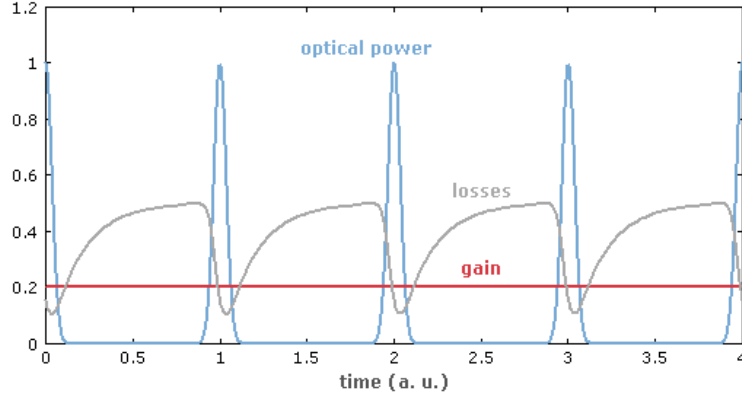


Figure 5.5: An example of a passively mode-locked laser with a slow saturable absorber

$$n(t) = n_i \exp -(E(t)/E_s^a) \quad (5.8)$$

where  $E(t) = \int_{-\infty}^t |v(t')|^2 dt'$  and  $n_i$  the initial carrier density. For a fast saturable absorber the population difference is an instantaneous a function of intensity following the relation:

$$n(t) = n_i [1 - |v(t)|^2 / I_s^a] \quad (5.9)$$

with  $I_s^a = E_s^a / \tau_a$

The Master equation for mode-locking is given by the Haus's equation:

$$\left( g(t) - \alpha(t) + \delta T_R \frac{d}{dt} + \frac{1}{\Delta\omega_g^2} \frac{d^2}{dt^2} \right) v(t) = 0 \quad (5.10)$$

with  $\delta T_R$  the possible time-shift of the travel time and  $\Delta\omega_g$  the gain bandwidth. If loss is self-modulated through the saturation of a slow saturable absorber, the normalized loss  $\alpha(t)$  can be written as follows:

$$\alpha(t) = 1 + \alpha_i \exp -(E(t)/E_s^a) \quad (5.11)$$

where  $\alpha_i$  is the initial value of the saturable absorber loss. The laser gain as a function of time is given by:

$$g(t) = g_i \exp -(E(t)/E_s^a) \quad (5.12)$$

where  $g_i$  is the initial gain just before the pulse arrival. By introducing (5.11) and (5.12) into (5.10), one obtains:

$$\left( g_i e^{-(E(t)/E_s^a)} - 1 - \alpha_i e^{-(E(t)/E_s^a)} + \delta T_R \frac{d}{dt} + \frac{1}{\Delta\omega_g^2} \frac{d^2}{dt^2} \right) v(t) = 0 \quad (5.13)$$

This is a nonlinear integro-differential equation. A simple solution of the equation is obtained if one expands the exponentials into power series and break them off with second order terms (weak saturation). For  $E_s^a \ll E_g^a$ , the solution of resulting equation is,

$$v(t) = \frac{v_0}{\cosh t/\tau_p} \quad (5.14)$$

Substituting (5.14) into (5.13) and equating terms of equal powers of  $\tanh(t/\tau_p)$ , one obtains three characteristics equations for the determination of the pulsewidth, detuning and pulse energy. Also, it is important to stress that the conditions

$$g_i \left( \frac{E_p}{E_s^g} \right)^2 < \alpha_i \left( \frac{E_p}{E_s^a} \right)^2 \quad (5.15)$$

and,

$$g_i < 1 + \alpha_i \quad (5.16)$$

must be met if the pulsewidth is to be real. Inequality (5.15) implies that the saturable absorber must be more easily bleached as compared to the gain medium. Condition (5.16) means that for stable mode-locking, the initial gain should be less than the initial loss. The solution of the characteristic equations shows that the pulsewidth  $\tau_p$  varies inversely with the pulse energy  $E_p$ .

This conclusion is also valid for mode-locking with a fast saturable absorber. Let us consider this type of mode-locking by following the approach developed by Haus for a ring laser cavity configuration as shown in figure 5.6. In this case the pulse envelope denoted  $A(z, t)$  is a function of time and a spatial coordinate  $z$ . The mode-locking equation can be written such as:

$$\frac{\partial A}{\partial t} + \frac{1}{v_g} \frac{\partial A}{\partial t} = g \left( 1 + \frac{1}{\Delta\omega_g^2} \frac{\partial^2}{\partial t^2} \right) A - \frac{\alpha_0}{1 + \frac{|A|^2}{I_s^a}} A \quad (5.17)$$

In order to solve this equation, one can approximate,

$$\frac{1}{1 + \frac{|A|^2}{I_s^a}} \approx 1 - |A|^2/I_s^a \quad (5.18)$$

This approximation and a transformation of the independent variables  $\xi = z$ ,  $\eta = t - z/v_g$  allows to re-write (5.17) into the form:

$$-\frac{\partial A}{\partial \xi} + (g - \alpha_0)A + g \frac{1}{\Delta\omega_g^2} \frac{\partial^2 A}{\partial \eta^2} + \alpha_0 \frac{|A|^2}{I_s^a} A = 0 \quad (5.19)$$

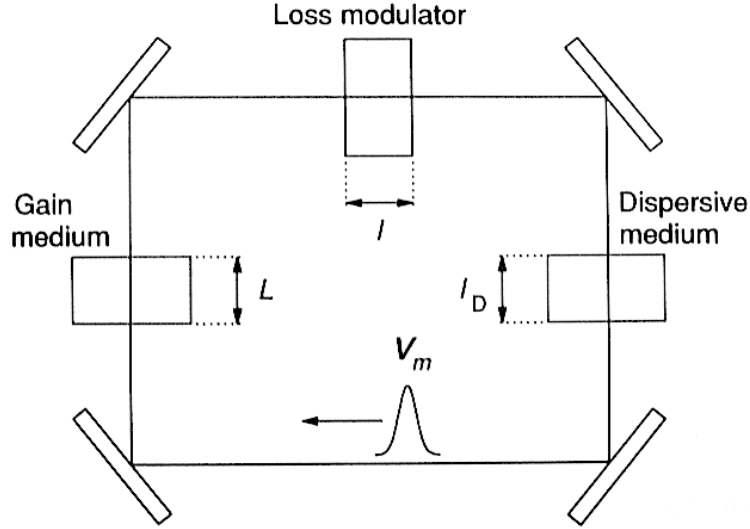


Figure 5.6: Schematic of a ring cavity used for mode-locking

When a steady-state pulse forms

$$\frac{\partial}{\partial \xi} = \frac{\partial}{\partial z} + \frac{1}{v_g} \frac{\partial}{\partial t} = 0 \quad (5.20)$$

and (5.19) can be reduced to,

$$(g - \alpha_0)A + g \frac{1}{\Delta\omega_g^2} \frac{\partial^2 A}{\partial \eta^2} + \alpha_0 \frac{|A|^2}{I_s^a} A = 0 \quad (5.21)$$

The finite bandwidth of the gain causes spreading of the pulse in time as described by the temporal diffusion operator  $\partial^2/\partial\eta^2$ . This diffusion time is balanced by the saturable loss term proportional to  $|A|^2$ . Equation (5.21) has a solution which can be written as follows,

$$A(z, t) = \frac{A_0}{\cosh \gamma(z - v_g t)} \quad (5.22)$$

with

$$v_g \gamma = \left( \frac{\alpha_0 \Delta\omega_g^2 |A_0|^2}{2g I_s^a} \right)^{1/2} \quad (5.23)$$

and

$$\alpha_0 - g = \frac{g}{\Delta\omega_g^2} (v_g \gamma)^2 \quad (5.24)$$

Expression (5.23) expresses the pulsewidth, which for the secant hyperbolic pulse is:

$$FWHM = \frac{2 \ln 2(1 + \sqrt{2})}{v_g \gamma} \approx 1.76 \left( \frac{2g I_s^a}{\alpha_0 \Delta\omega_g^2 |A_0|^2} \right)^{1/2} \quad (5.25)$$

which shows that more powerful power pulses should be shorter. It also implied that shorter pulses can be obtained with an absorber that can be more easily saturated that is with lower  $I_s^a$ . A secant hyperbolic pulse shape in passively mode-locked lasers with a low saturation level ( $E_p \ll E_s^a, E_s^g$ ) is consistent with experimental results. However, it should be stressed that for more powerful pulses, the pulse shape may be distorted by gain and loss saturation and the asymmetric pulses may be generated in the laser.

## 5.4 Colliding Pulse Mode-Locking

The colliding pulse mode-locking technique (CPM) has been shown to be very effective in creating optical pulses that are in the femtosecond range. CPM utilizes the forward and backwards traveling light inside the laser cavity to build up a transient standing wave. An example of a monolithic CPM laser is shown in figure 5.7. The ultra-short pulses are achieved by having these forward- and backward-traveling waves collide inside the absorber section and saturating (bleaching) the section. This collision creates a spike in optical intensity creating an associated pulse. The collision creates a much stronger saturation of the absorber than would be possible with just a single pulse traveling through at one time. The length of the absorber section can control the ease and quality of mode locking. The absorber introduces

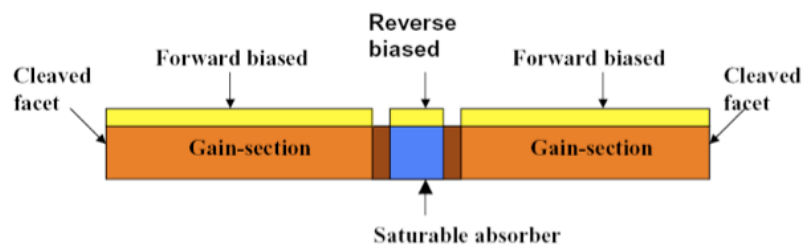


Figure 5.7: Schematic view of a monolithic colliding pulse mode-locked laser (CPM)

a nonlinearity that leads to a change in pulse shape, which causes the pulse to compress. If the colliding pulses traveling into the absorber section are relatively large compared to the absorber, the resultant pulse will undergo significant compression due to the short length of the absorber section. This pulse will not only have significant compression, but it will be near the saturation energy of the gain section. The energy associated with the wide pulse is conserved, but is now confined into a smaller pulse width, which results in a greater intensity. This is a very important aspect to CPM because it allows passively mode-locked laser to operate at low pulse energy for maximum compression while still providing adequate optical power. It is also possible to apply this technique in order to generate higher order harmonics of the laser's fundamental frequency.

## Double-Interval Mode-Locking Technique

Double-interval mode-locking takes advantage of a semiconductor laser's ease of reconfigurability and harmonic mode-locking. The double-interval technique (see also section 5.6) refers to using two saturable absorbers that independently stimulate harmonics of the device in order to achieve the multiplicative value of the two harmonics. The double interval technique is similar to CPM in that it utilizes saturable absorbers to create a pulse. The unique aspect of the double-interval technique is that by creating two saturable absorber sections within the laser cavity, it is possible to create a condition where the pulses created can collide together and affect each other. By using this knowledge, it is possible to place the absorbers in specific locations in order to create the desired optical pulse. For example, to stimulate the laser's tenth harmonic a saturable absorber can be placed in the midpoint of the laser diode and another at a point corresponding to a fifth of the laser diode. Individually they would stimulate the second and fifth harmonics, but with the double-interval technique they are stimulated simultaneously and result in the stimulation of the tenth harmonic. A harmonically mode-locked laser produces an optical pulse train at a multiple of the fundamental round-trip frequency. This is very advantageous for semiconductor lasers because they already have a high fundamental frequency due to their short cavity length. Combined with the double interval technique it is possible to get very high repetition rates from semiconductor laser diodes. Photolithography techniques and mask designs can create a segmented semiconductor laser diode, but as more and more divisions are desired it becomes difficult to achieve good results. Double interval harmonic mode-locking is beneficial because it overcomes the limitations introduced by standard processing. By utilizing this technique it is possible to lock to higher order harmonics that would correspond to repetition rates that would be very difficult to achieve by just mode-locking alone. As seen in figure 5.8 it is possible to segment the device for the double-interval technique or into divisions that will allow for the simulation of the desired harmonic. In the case for figure 5.8, it is desired to stimulate the 10th harmonic of the device. Traditionally this would require the device to be segmented in order to isolate a section that would correspond to a tenth of the device. As discussed earlier this may be limited to photolithography techniques and as dimensions get smaller it becomes difficult to wire-bond and probe the device. With the double-interval technique it is possible to maintain larger segments and stimulate the 10th harmonic.

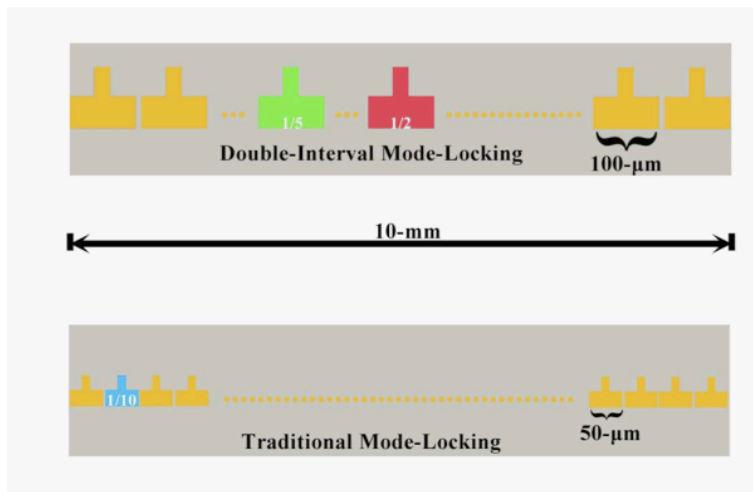


Figure 5.8: Comparison between device segmentation for double-interval mode-locking and traditional mode-locking for the 10th harmonic of a laser diode

## 5.5 Monolithic Quantum Dot Passively Mode-Locked Lasers

In the early 1990's there was considerable interest in mode-locked semiconductor lasers and their potential use in high-speed optical systems, which require a compact, low jitter source that could produce picosecond pulses. This work culminated in the demonstration by Bell Labs of the 350 GHz colliding pulse modulated laser. What ultimately discouraged further efforts was the complexity and expense of the electronics for the active and hybrid mode-locking that were necessary to stabilize the pulse train. Passively mode-locked semiconductor laser sources, which require no synchronization by external drivers circuits were greatly preferred for their simplicity, but were plagued with large timing jitter ( $>10$  ps), because of the significant amplified spontaneous emission noise generated by the quantum well (QW) active region. This large timing jitter limited the usefulness of short pulse devices. The QW devices also had limited power output in the pulses due to mode competition above threshold and non-linear gain effects.

Recently, these issues with power and jitter have been significantly improved upon using quantum dot active regions. The typical device configuration of these next-generation QD MLLs is shown in figure 5.9. Two of the advantages of QDs that are exploited are the lower saturation intensity that is needed to bleach the absorber section and the ability to run the gain section under strong inversion for high peak pulsed powers. These two features that make QD MLLs easier to lock and operate can be summarized in an important figure of merit for mode-locked lasers, the ratio of the saturation energy of the gain section to the

saturation energy of the absorber:

$$\frac{E_{sat,g}}{E_{sat,a}} = \frac{\frac{h\nu A_m}{\Gamma \frac{dg}{dN}}}{N_t h\nu A_m} = \frac{1}{\Gamma N_t \frac{dg}{dN}} \quad (5.26)$$

where  $A_m$  is the cross-sectional area of the optical mode,  $\Gamma dg/dN$  is the differential modal gain (or optical cross-section), and  $N_t$  is the optical transparency density. These three parameters all have units of  $\text{cm}^{-2}$ . The transparency density is directly controlled by the dot density, the lower limit of which is essentially limited only by the internal loss of the optical cavity. The differential gain in a quantum dot ensemble can also be made very small because the gain saturation of quantum dots with volumetric carrier density,  $N$  ( $\text{cm}^{-3}$ ), is so strong. This effect has been used to great advantage in designing reconfigurable quantum dot mode-locked lasers. QW gain regions also have 2-3 times larger transparency densities which is undesirable as seen in the figure of merit equation above. Mode-locking is not a guarantee

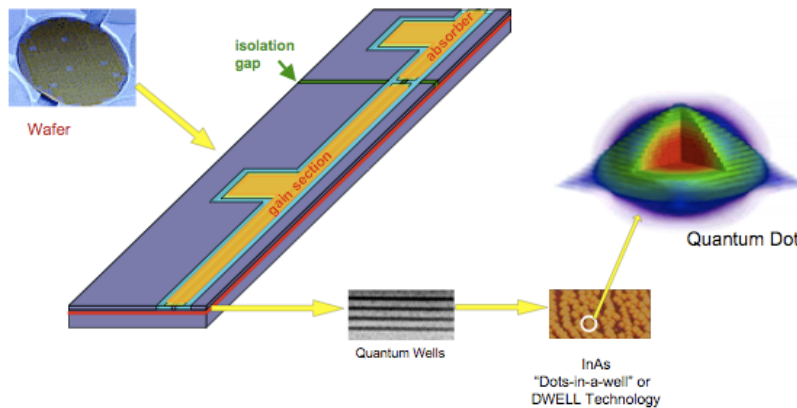


Figure 5.9: Schematic diagram of a 2-section monolithic MLL with QD gain and absorber regions. The facet at the absorber end of the device is HR coated to produce the quasi-colliding pulse mode-locking effect and narrow the pulse width

that there is no jitter in the output pulses. Even when the laser is mode-locked, there can be phase instabilities between the frequencies that make up the pulse. Indeed, to generate stable optical combs for metrology, great lengths must be placed on both carrier envelop phase stabilization and frequency locking of the comb. Such systems would have very low jitter and noise. Unfortunately, they are large, fragile, and complex. The compact size, low power consumption, direct electrical pumping of semiconductor MLLs make them well-suited for optical clocking in applications such as analog-to-digital conversion as well as high bit-rate optical time division multiplexing, electro-optic sampling, and impulse response

measurement of optical components. For these applications, low timing jitter of the ultra-short optical pulses is required since the fluctuation of the pulse arrival time degrades bit-error rate and time resolution. Among the different MLL configurations, the monolithic 2-section passively mode-locked semiconductor laser is the most desirable option for low-cost high-volume production due to device compactness and system simplicity. However, previous QW monolithic, passive MLLs have suffered from much larger timing jitter compared to active or hybrid MLLs. The timing jitter in passive MLLs arises from the fluctuations in carrier density, photon density, and index of refraction caused by the amplified spontaneous emission (ASE). Due to the discrete energy levels and low transparency current in a QD gain medium, the portion of carriers involved in the non-stimulated emission is significantly reduced. Therefore, low ASE is expected in QD devices, suggesting that a lower timing jitter can be achieved with QD passive MLLs compared to QW passive MLLs. Detailed measurements of the jitter as a function of injected current in the gain section and constant voltage on the saturable absorber showed that the jitter initially decreases with current, reaches a minimum, and then increases again at higher bias. This phenomenon is shown in figure 5.10 for various absorber voltages. That is, near threshold, spontaneous emission and stimulated emission compete, causing incomplete mode-locking, which, in turn makes the jitter higher. As the output

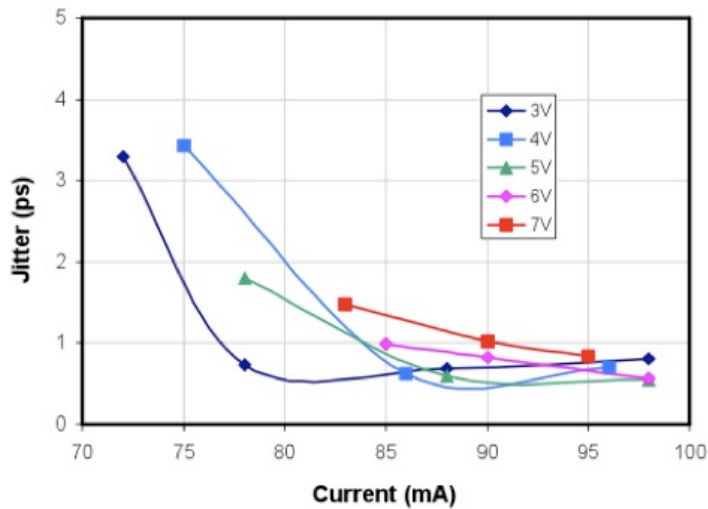


Figure 5.10: The measured jitter of a QD MLL as a function of gain section current for various absorber voltages. 500 fs jitter is routinely achieved in this device

power increases (with increasing bias current) in these quantum dot lasers, the linewidth enhancement factor begins to increase causing an increase in the coupling between the phase and the amplitude. Thus, intensity noise couples more strongly into phase noise, increasing the jitter. The same trend occurs in the pulse width of the device meaning that in QD

MLLs the jitter behavior seems to be closely correlated with the pulse width one. Further improvement in the jitter can be realized using optical injection. It is anticipated that optical injection will improve the jitter by roughly a factor of 5.

## 5.6 Colliding Pulse Technique for Higher Order Harmonic Generation

The double-interval technique utilizes colliding pulses to generate higher order harmonics of a semiconductor laser diode. Using the colliding pulse technique, higher order harmonics of the repetition rate can be excited. Analogous to the method used by a violinist to create high order harmonic sounds, the colliding pulse technique can create higher order harmonics of a laser's fundamental frequency. The difference is with the mode-locked laser, anti-nodes are created rather than nodes. When a violinist places his finger upon a string he creates a node that changes the tune of the violin as it is strummed. The strumming of the violin without the violinist placing a finger upon the fingerboard creates the first harmonic also known as the fundamental harmonic. If the location of the node were in the center of the fingerboard, this would result in the creation of the second harmonic. Placing the finger at a location at a third, fourth, or fifth of the fingerboard will result with the third, fourth, and fifth harmonics, respectively. For instance, figure 5.11 shows the locations of nodes and the corresponding harmonics. By stimulating multiple nodes simultaneously, it is possible to create higher order harmonics that are equivalent to the product of the nodes' harmonics. Since it is possible to create the second and fifth harmonics separately, applying both nodes concurrently will create the tenth harmonic. This technique can be extended to a device to create the higher order harmonics of the laser's fundamental repetition rate. When applied to a mode-locked laser technique, applying a reverse bias to the corresponding location creates an absorber section. If this absorber is saturable, not strong enough to absorb all of the excess carriers present, then it behaves as an anti-node. This saturable absorber is an anti-node because it creates a location where a maximum can occur rather than a fixed minimum as with a node. It is these anti-nodes that are needed to provide the generation of the higher order harmonics. Also, obtaining high order harmonics would be difficult to achieve by simply creating a single anti-node. This would require placing the anti-node at a division of the laser that might be impractical to achieve. Thus multiple anti-nodes can be used to generate the desired harmonic using the double-interval technique. Figures 5.12 and 5.13 show an example of a laser diode with anti-nodes corresponding to the second and fifth harmonics which are used to create the tenth harmonic. This allows for the generation of harmonics that would not be possible to create with just one anti-node. With this device in particular, when the saturable

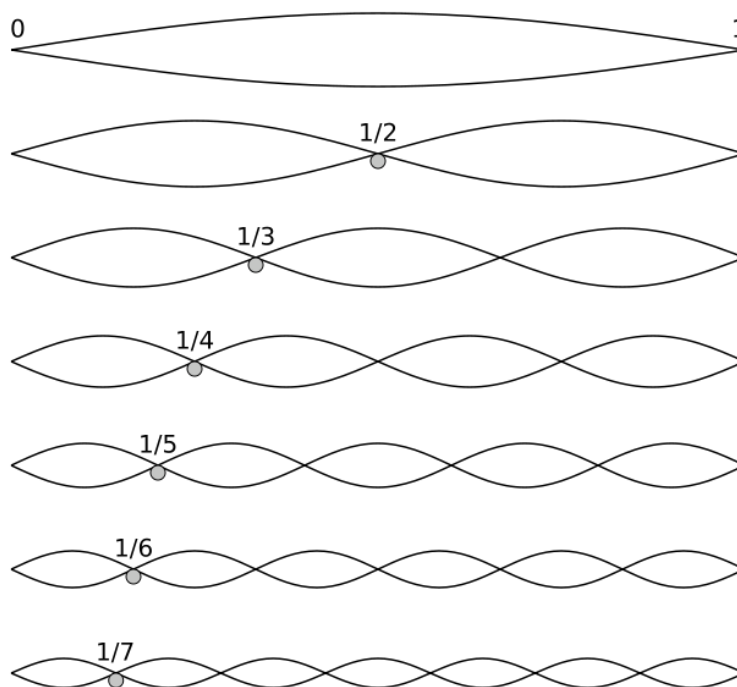


Figure 5.11: Location of nodes and corresponding harmonic generated

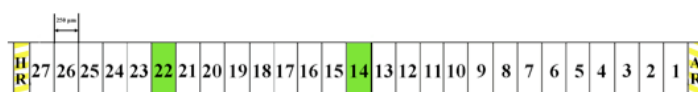


Figure 5.12: Laser anti-nodes for creation of tenth harmonic

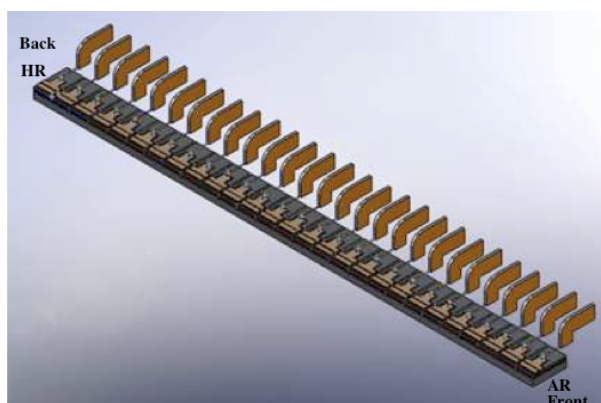


Figure 5.13: Segmented device for higher harmonic generation

absorber was placed close to the sections corresponding to the fundamental repetition rate, the fundamental repetition rate was excited. So to stimulate the tenth harmonic with just one saturable absorber at the location corresponding to 25 was not possible because it stimulated the fundamental harmonic. Figure 5.14 shows the Radio Frequency (RF) spectrum for the fundamental, 2nd, 3rd, 5th, and 6th harmonics of the QD mode-locked laser depicted in figure 5.13. Since it is desired to have the pulses collide inside the saturable absorber, the forward and backwards traveling waves must be of enough combined intensity in order to saturate the absorber. As stated earlier, in order to generate optical pulses for a passive mode-locked laser the loss must saturate faster than the gain. This introduces the stability condition  $s$  of a passively mode-locked laser described by (5.26). The stability condition gauges the quality of the laser's mode-locking and is used as a guideline for getting into the locking regime.

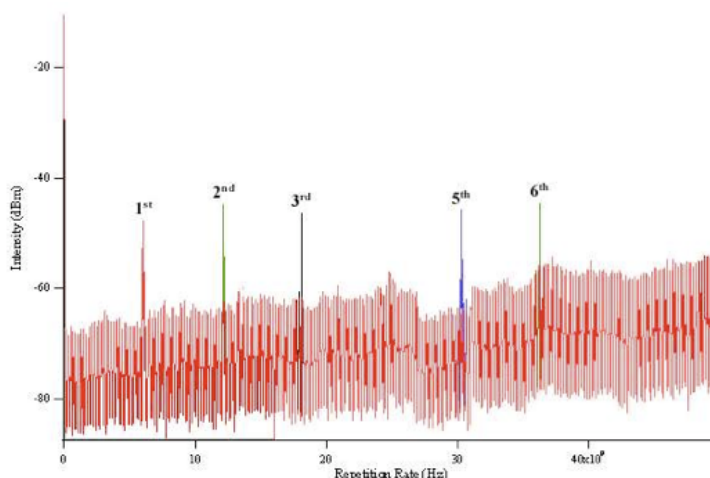


Figure 5.14: 50 GHz span of the mode-locked laser's fundamental harmonic (6.0 GHz), 2nd harmonic (12.0 GHz), 3rd harmonic (18.0 GHz), 5th harmonic (30.0 GHz), and 6th harmonic (36.0 GHz)

# Chapter 6

## Injection-Locking of Semiconductor Diode Lasers

### 6.1 Introduction

Optical-injection of semiconductor lasers involves two optical sources referred to as the master and slave lasers as seen in figure 6.1. The master laser, typically a high- power single-mode narrow-linewidth tunable laser, is injected into the slave laser, thereby affecting the operation and inherent free-running characteristic parameters of the slave laser. An isolator is placed between master and slave lasers to eliminate reflected light coupling back to the master laser. Under stable injection-locking of semiconductor lasers, which occurs when the strength of the injected master laser light and frequency difference between the master and slave fall within a certain range, the slave's lasing wavelength is pulled/locked to the injected master laser's wavelength. Stable injection- locking provides several improvements to directly-modulated lasers. These improvements include increasing the modulation bandwidth, suppressing non-linear distortion, and reducing relative intensity noise, mode hopping, and chirp. A ba-

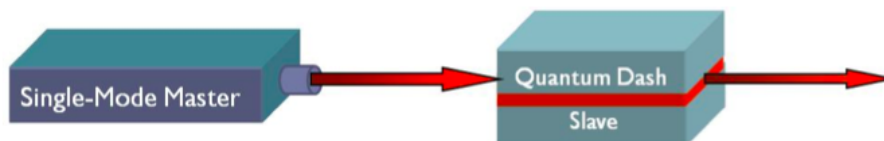


Figure 6.1: Principle of an Injection-Locked Semiconductor Laser Diode

sic example of the spectral improvements under stable injection-locking for a multi- mode Fabry-Perot quantum-dash slave laser was already shown in figure 1.14. An example of

the modulation bandwidth enhancement for the injection-locked Fabry-Perot quantum-dash semiconductor laser is shown in figure 6.2. The characteristics of the modulation response curves in figure 6.2 are observed to vary as a function of the detuning frequency between the master and slave lasers for a fixed injection strength. Besides the stable injection-locking

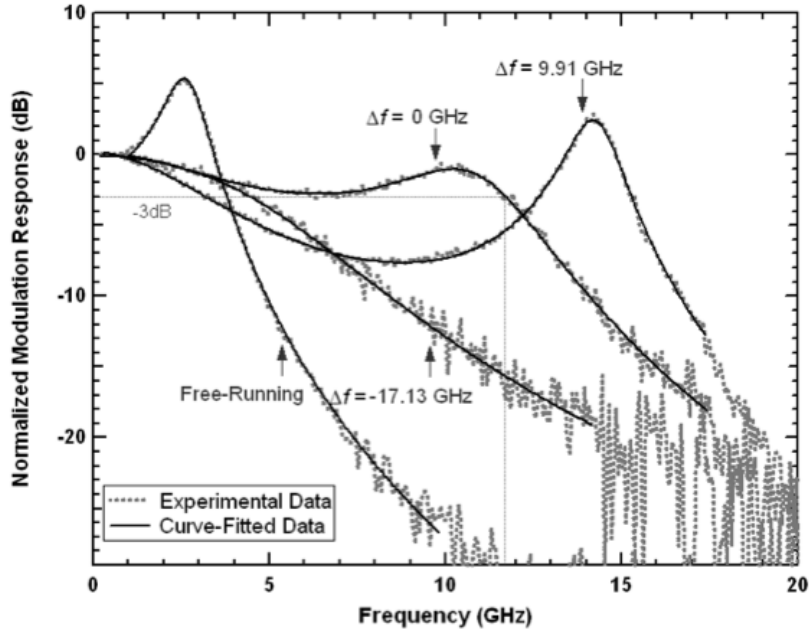


Figure 6.2: Modulation response of the injection-locked quantum-dash laser for varied frequency detuning ( $\Delta f$ ) conditions.

regime, the optically-injected system demonstrates a dynamic behavior whereby the optical spectra are characterized by the appearance of relaxation oscillation sidebands and coherence collapse. The optical power spectra associated with the dynamic states exhibited by a diode laser under optical-injection are referred to as period-one, period-doubling, four-wave mixing, and coherence-collapse, and are illustrated in figure 6.3. The optical spectra shown in figure 6.3 are unique in nature due to the high resolution of the spectrometer used in data collection (maximum resolution = 1 MHz), which allowed extreme detail of the optically-injected quantum-dash laser's behavior to be observed. In figure 6.4 and throughout this work, the detuning frequency is defined as:

$$\Delta f = f_{master} - f_{slave} \quad (6.1)$$

An unlocked system, where either the injected signal strength is weak and/or the frequency difference is too large resulting in the master laser field having no impact on the slave laser, is shown in figure 6.3(a). The period-one state, illustrated in figure 6.3(b), is characterized by

the presence of undamped relaxation oscillation sidebands. Figure 6.3(c) shows the period-doubling state which is similar to the period-one state, but with additional relaxation oscillation side-bands associated with a second periodic-oscillator at roughly half the slave laser's characteristic relaxation oscillation frequency. Stable locking is shown in figure 6.3(d) and is characterized by single mode operation with a significant degree of side mode suppression (defined here as  $> 30$ - dB), where the single locked-mode has a narrow linewidth, reduced chirp and noise compared to the slave laser's free running characteristics. The small side modes (side mode suppression  $> 40$  dB) in figure 6.3(d) are attributed to residual feedback in the experimental setup. The coherence-collapse state pictured in figure 6.3(e) is characterized by a large broadening of the coupled system's linewidth. Four-wave-mixing is shown in figure 6.3(f) and is described as a pseudo-unlocked state where two additional frequencies are generated due to optical non-linearities in the device. Under four-wave mixing, the slave laser's operating frequency is unaffected by the injected power. For a fixed injected master power, the coupled system will progress from the period-one state to four-wave-mixing for increased detuning frequencies and a clear boundary is typically difficult to quantitatively determine. The microwave modulation response under period-one, period-doubling, and coherence collapse are normally considered undesirable for use in high-speed coherent optical communication systems where the slave laser is directly-modulated. With the optical power spectral descriptions describing the operational states (stable-locking, period-one, period-doubling, coherence collapse, four-wave-mixing), stability maps characterizing the dynamic state as a function of the maximum injection strength and detuning frequency can be constructed for a given slave laser. An example is illustrated in figure 6.4 for a quantum-dash Fabry-Perot slave laser. The relatively stable operation under zero frequency-detuning conditions and the large period-one oscillation state parameter space open the quantum-dash laser to possible applications as a tunable photonic oscillator or directly-modulated slave laser in a coherent optical communication system.

## 6.2 Applications of Optically-Injected Lasers

Communication applications of optically-injected semiconductor lasers have predominantly focused on the stable locking state achieved under strong injection where desirable high frequency modulation characteristics have been exhibited. Recently, however, the complex nonlinear dynamical states resulting from the optical-injection of semiconductor lasers have generated increased interest for many novel applications. Potential applications based on their rich nonlinear dynamics include: chaotic communications, chaotic lidar, chaotic radar, photonic microwave generation, dual-frequency precision radar/lidar, all-optical AM-to-FM conversion, and single-sideband radio-over-fiber transmission. In this section, the applications

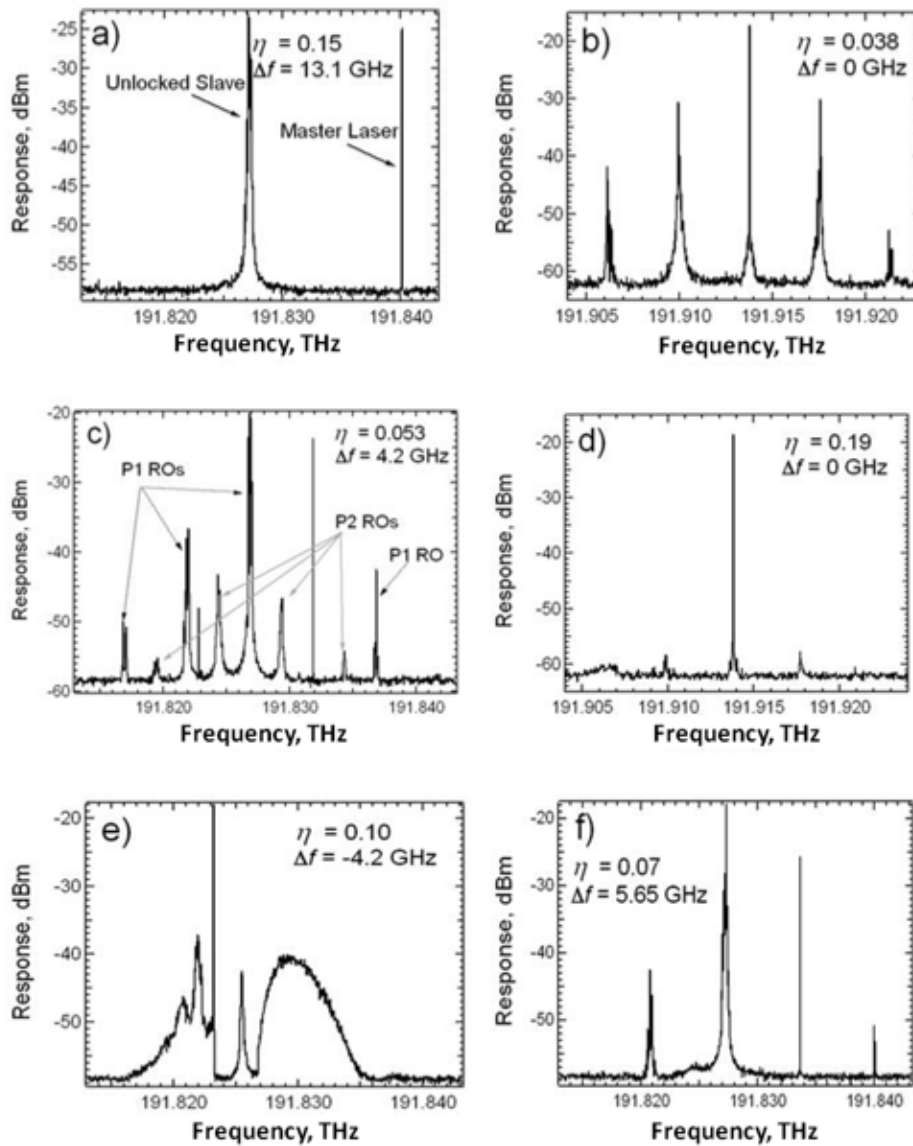


Figure 6.3: Behavioral states of a quantum-dash laser subject to optical-injection. The injection strength and detuning frequency are indicated on the individual figures. (a) Illustrates the unlocked case; (b) the period-one oscillation state; (c) period-doubling; (d) stable-locking; (e) coherence collapse; and (f) four-wave-mixing.

of the period-one operational state are discussed.

The period-one state is described as the condition where the slave laser is locked to the injected field and the coupled system oscillates at the injected frequency ( $f_{inj}$ ) with sidebands at frequencies of  $f_{inj} - f_r$ , where  $f_r$  is the resonance frequency of the optically-injected laser as illustrated in figure 6.5. The resultant electric field of the optically-injected slave laser oscillates without being damped towards a steady-state value as in a free-running or stable-locked semiconductor laser. The period-one resonance frequency is tunable based on the injection strength and/or detuning frequency between the master and slave laser, generating a microwave modulation on the laser output in an all-optical manner. Compared with

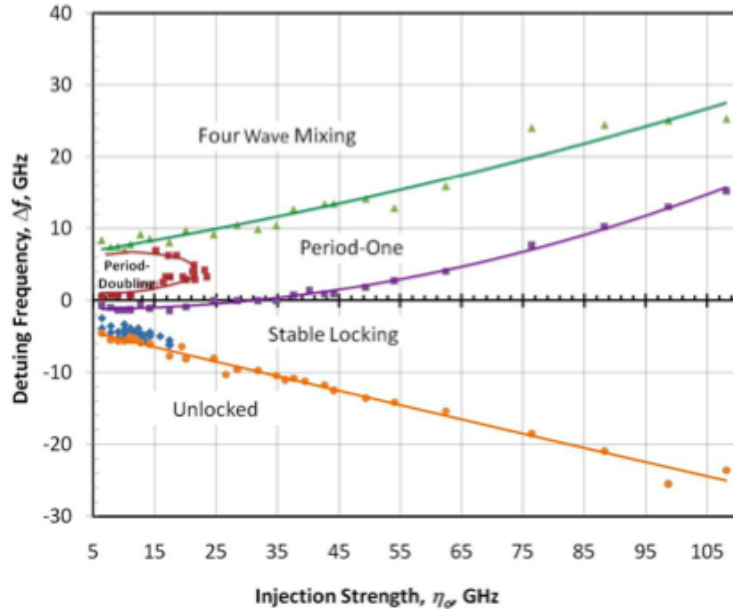


Figure 6.4: Stability map for an optically-injected quantum-dash slave laser at a bias current of 65 mA showing only stable and period-one operation at zero-detuning and a large period-one parameter space as the injection strength and/or detuning frequency are varied. The blue diamonds at negative detuning indicate chaotic (coherence collapse) operation. The trendlines have been added as a visual aid only.

direct modulation, external modulation, mode-locking, self pulsation, and optical phase-lock loops, the period-one approach presents several advantages in microwave generation. The primary advantage identified is that the all-optical approach of optical-injection avoids the limitations of microwave electronics and electrical parasitics. In this regard, the system is controlled using the DC injection current of the master laser to modulate its output power resulting in a tunable resonance frequency varying from the free-running laser's natural relaxation oscillation frequency to up to six times this value. Generation of period-one microwave frequencies up to 60 GHz have even already been reported, making the period-one

optical-injection system an ideal radio-over-fiber source. Radio over Fiber (RoF) refers to a

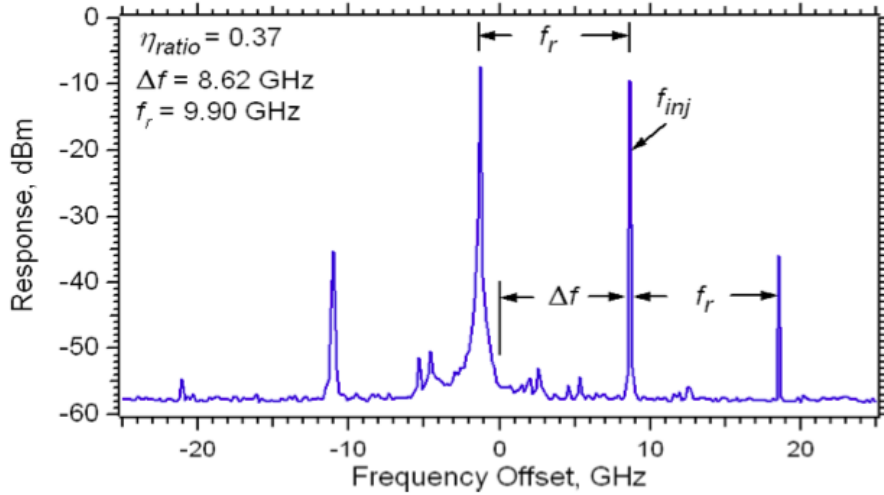


Figure 6.5: Optical power spectra of an optically-injected quantum-dash laser under a bias of 65 mA in the period-one oscillation state. The injected field ratio and detuning frequency are indicated on each plot.  $f_r$  is the measured resonance frequency.  $\Delta f$  is the detuning frequency.

technology whereby light is modulated by a radio signal and transmitted over an optical fiber link to facilitate wireless access. Although radio transmission over fiber is used for multiple purposes, such as in cable television (CATV) networks and in satellite base stations, the term RoF is usually applied when this is done for wireless access. In RoF systems, wireless signals are transported in optical form between a central station and a set of base stations before being radiated through the air. Each base station is adapted to communicate over a radio link with at least one user's mobile station located within the radio range of said base station. RoF transmission systems are usually classified into two main categories (RF-over-Fiber ; IF-over-Fiber) depending on the frequency range of the radio signal to be transported.

a) In RF-over-Fiber architecture, a data-carrying RF (Radio Frequency) signal with a high frequency (usually greater than 10 GHz) is imposed on a lightwave signal before being transported over the optical link. Therefore, wireless signals are optically distributed to base stations directly at high frequencies and converted to from optical to electrical domain at the base stations before being amplified and radiated by an antenna. As a result, no frequency up/down conversion is required at the various base station, thereby resulting in simple and rather cost-effective implementation is enabled at the base stations.

b) In IF-over-Fiber architecture, an IF (Intermediate Frequency) radio signal with a lower

frequency (less than 10 GHz) is used for modulating light before being transported over the optical link. Therefore, wireless signals are transported at intermediate frequency over the optical.

### **Advantages of Radio-over-Fiber**

- **Low Attenuation:** It is a well known fact that signals transmitted on optical fiber attenuate much less than other medium, especially when compared to wireless medium. By using optical fiber, the signal will travel further reducing the need of repeaters.

- **Low Complexity:** RoF makes use of the concept of a Remote Station (RS). This station only consists an optical-to-electrical (O/E) (and an optional frequency up or down converter), amplifiers, and the antenna. This means that the resource management and signal generation circuitry of the Base Station can be moved to a centralized location and shared between several remote stations, thus simplifying the architecture.

- **Lower Cost:** Simpler structure of remote base station means lower cost of infrastructure, lower power consumption by devices and simpler maintenance all contributed to lowering the overall installation and maintenance cost. Further reduction can also be made by use of low cost Graded Index Polymer Optical Fiber (GIPOF).

- **Future Proof:** Fiber Optics are designed to handle gigabits speeds which means they will be able to handle speeds offered by future generations of networks for years to come. RoF technology is also protocol and bit-rate transparent, hence, can be employed to use any current and future technologies.

### **Applications of Radio-over-fiber**

- **Access to dead zones:** An important application of RoF is its use to provide wireless coverage in the area where wireless backhaul link is not possible. These zones can be areas inside a structure such as a tunnel, areas behind buildings, Mountainous places or secluded areas such a jungle.

- **FTTA (Fiber to the Antenna):** By using an optical connection directly to the antenna, the equipment vendor can gain several advantages like low line losses, immunity to lightning strikes/electric discharges and reduced complexity of base station by attaching light weight Optical-to-Electrical (O/E) converter directly to antenna.

The frequency tunability of the period-one resonance frequency based on the strength of the injected signal opens the possibility of all-optical AM-to-FM conversion, enabling the integration of the optical-injection architecture into radio-over-fiber systems. In the AM-to-FM conversion application, the input amplitude modulated signal is used to drive the master laser injecting the slave laser under a condition that results in the period-one oscillation state; the amplitude modulated signal injecting the slave laser will then be converted to a frequency modulated microwave signal. The optical-injection based AM-to-FM frequency modulation conversion increases bandwidth capabilities, and reduces signal distortion, electronic noise, and power consumption. A depiction of the radio-over-fiber architecture using optical-injection to perform the AM-to-FM conversion is given in figure 6.6.

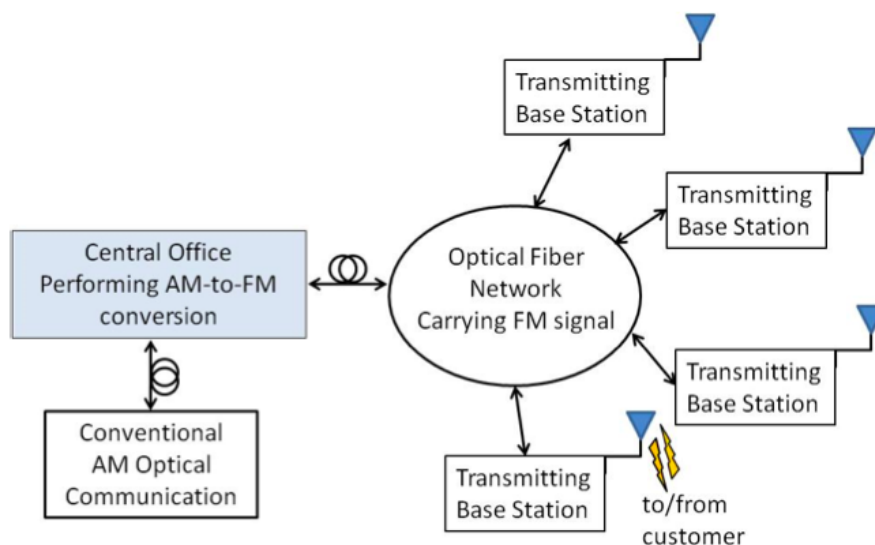


Figure 6.6: Generic depiction of the radio-over-fiber architecture. The AM-to-FM conversion is performed at the central office and the FM modulated optical signal is transmitted to the base stations simplifying base station processing requirements.

### 6.3 Theoretical Description

In order to understand the limiting factors in an injection-locked system it is important to investigate the governing theory that can be obtained by modeling the characteristic parameters using a set of coupled rate equations. Mathematical translation of the injection-locking system operating in the stable locking regime based on three fundamental rate equations. The Lang and Kobayashi model was initially proven to be valid only for weak injection cases; however, with some minor changes it has been shown to be useful in predicting the operating properties of the system regardless of the magnitude of injection strength. This section

capitalizes on improvements to the rate equations governing the dynamic properties of an injection-locked system in order to investigate the modulation properties of such a system under strong injection.

### 6.3.1 Rate Equations

The differential equations describing the dynamics of an injection-locked system have been developed by introducing terms describing the impact of optical injection to the conventional rate equations governing the free-running characteristics of the slave laser. The additional terms include a coupling value,  $k_c$ , the magnitude of the injected master field,  $A_{inj}$ , and the detuning frequency between master and slave,  $\Delta\omega$ . The model assumes the slave laser is being directly modulated such that the small signal approximation can be applied. Additionally, it is assumed that the laser has been exposed to a relatively strong external optical injection, such that the impact of the noise and the spontaneous emission rate coupled to the lasing mode are negligible. The free-running Fabry-Perot slave laser has cleaved facets and is biased well above threshold. As in the free running case, the amplitude and phase equations arise from the fundamental complex field rate equation. The variation of the slave field magnitude, phase offset between the master and slave fields and carrier density with time can be written as :

$$\frac{dA}{dt} = \left(\frac{g}{2}\Delta N\right) A + (k_c \cos(\phi)) A_{inj} \quad (6.2)$$

$$\frac{d\phi}{dt} = \alpha \left(\frac{g}{2}\Delta N\right) A - \Delta\omega - (k_c \sin(\phi)) \frac{A_{inj}}{A} \quad (6.3)$$

$$\frac{dA}{dt} = J_{bias} - \gamma_N N - (\gamma_P + g\Delta N) A^2 \quad (6.4)$$

where  $A$  is the internal slave's amplitude of the electric field,  $g$  is the differential gain,  $N$  is the carrier density and  $\Delta N = N - N_{th}$  is the shift in carrier density from the threshold.  $\phi$  is the phase offset between master and slave laser, which is defined as  $\phi_{slave} - \phi_{master}$ , the amplitude of the electric field square,  $A^2$ , is proportional to photon density  $P$  and  $J_{bias}$ ,  $\gamma_N$ ,  $\gamma_P$  correspond to the applied bias current density, inverse differential carrier lifetime and photon decay rates, respectively. It is important to note that the phase variation in time depends on detuning through  $\Delta\omega = \omega_{slave} - \omega_{master}$ . The linewidth enhancement factor,  $\alpha$ , injection strength which is proportional to  $A_{inj}/A$ , phase offset  $\phi$ , and detuning term  $\Delta\omega_{inj}$  are the key and defining injection parameters that have a significant impact on the coupled oscillator system.

### 6.3.2 Steady-State Solutions

The equations described in the previous section define the temporal and dynamic behavior of the system. The injection-locking phenomenon is investigated through the steady-state solutions arising from these three differential equations. Under steady-state, the right hand side of (6.2) to (6.4) is equal to zero as there will be no time variation in the slave's field amplitude, phase and carrier density. The steady-state parameters of the injection-locked system can be defined as the steady-state phase offset,  $\phi_0$ , steady-state carrier density,  $N_0$ , steady-state locked slave field,  $A_0$ , and the free-running slave field,  $A_{fr}$ . Based on this strategy the first general condition for the system under injection-locking can be clearly found through (6.3) by replacing the steady-state parameters and setting the left hand side equal to zero:

$$\Delta\omega = \alpha \left( \frac{g}{2} \Delta N \right) A - (k_c \sin(\phi)) \frac{A_{inj}}{A} \quad (6.5)$$

where the change in carrier density under steady-state condition is expressed as  $\Delta N_0 = N_0 - N_{th}$ . Note that for stability it is required that the change in the steady-state carrier density be less than zero,  $\Delta N_0 < 0$ . Equation (6.5) describes the correlation between frequency detuning, threshold condition and the strength of the injected field. It can be clearly seen that depending on the detuning condition and the phase offset, the injected field can result in a threshold gain shift through  $g\Delta N_0$ . Note that the group velocity is implicit in the differential gain term,  $g$ . Using this method and solving the steady-state parameters of the coupled system, the relationship between the free-running and locked fields and also the expression for the steady-state phase offset can be expressed as:

$$A_0^2 = \frac{A_{fr}^2 - \frac{\gamma_N}{\gamma_P} \Delta N_0}{1 + \frac{g\Delta N_0}{\gamma_P}} \quad (6.6)$$

$$\phi_0 = \sin^{-1} \left( -\frac{\Delta\omega}{k_c \sqrt{1 + \alpha^2}} \frac{A_0}{A_{inj}} \right) - \tan^{-1} \alpha \quad (6.7)$$

The steady-state slave field and the phase offset between the slave and master laser and its boundary can be further used to derive an expression for detuning,  $\Delta\omega_{inj}$ . However, computing the detuning value for a specific case is not possible unless the key parameters such as phase offset, linewidth enhancement factor, and injection strength can be extracted for that case.

### 6.3.3 Small-Signal Analysis

A detailed approach to find the small-signal solution of the rate equations expressed in (6.2) through (6.4) has been demonstrated in the literature. Based on this method the absolute

modulation frequency response function can be expressed as:

$$|H(\omega)|^2 = \left| \frac{\Delta A}{\Delta J} \right|^2 = \frac{|M|^2(\omega^2 + Z^2)}{(C - A\omega^2)^2 + (B\omega - \omega^3)^2} \quad (6.8)$$

where the parametric terms  $A$ ,  $B$ ,  $C$ ,  $Z$  and  $M$  can be defined and simplified as:

$$A = 2\eta \cos \phi_0 + \gamma_N + gA_0^2 \quad (6.9)$$

$$B = \eta^2 + 2\eta \cos \phi_0(gA_0^2 + \gamma_N) + gA_0^2(\gamma_P - 2\eta \cos \phi_0) \quad (6.10)$$

$$C = \eta^2(\gamma_N + gA_0^2) - gA_0^2(\gamma_P - 2\eta \cos \phi_0)Z \quad (6.11)$$

$$Z = \eta(\alpha \sin \phi_0 - \cos \phi_0) \quad (6.12)$$

$$M = \frac{g}{2}A_0 \quad (6.13)$$

The injection strength is proportional to the coupling term and the field ratio as:

$$\eta = k_c \frac{A_{inj}}{A_0} = \frac{\eta_0}{R_{FE}} \quad (6.14)$$

where  $\eta_0$  is the maximum injection ratio and  $R_{FE} = A_0/A_{fr}$  is the slave field enhancement factor due to injection.  $\eta_0$  incorporates the external master to slave power ratio, the coupling efficiency between the slave and master laser, and efficiency of injected field entering the slave laser cavity due to facet reflectivity. At this point, the enhancement of the slave field is introduced as an additional term denoted as the field enhancement factor,  $R_{FE}$ , which takes into account the deviation of the slave steady-state field magnitude compared to its free-running value at high injection ratios and specific frequency detuning.

### 6.3.4 Modulation Response Model

The modulation response model expressed in (6.8) can be used to simulate the modulation characteristics of an injection-locking system in microwave domain. However, since there are as many as 8 fitting parameters involved in this model, such a large number of potentially unconstrained parameters allows for many possible solutions that would reduce the confidence in extracted results. Thereby, one of the goals is to reduce the number of fitting parameters through known free-running slave terms along with additional constraints on remaining injection-locking fitting terms. Doing so, the parametric terms  $A$ ,  $B$ ,  $C$ , and  $Z$  defined in (6.8) can be translated in terms of known free-running and injection-locked parameters. This reduces the fitting parameters while the remaining terms are expressed with respect

to the injection-locking operating parameters of the system which then will be projected in the targeted relative modulation response function. Since the  $M^2$  term defined in (6.13) is independent of frequency, it can be cancelled in the relative modulation response form. The  $A$  term in (6.8), is effectively a damping rate of the coupled oscillator as follows:

$$A = \gamma_{slave} + \gamma_{th} \quad (6.15)$$

The slave damping rate,  $\gamma_{slave}$ , is related to the free running damping rate and scales with the field enhancement factor as:

$$\gamma_{slave} = gA_0^2 + \gamma_N = (\gamma_{fr} - \gamma(N))R_{FE}^2 + \gamma_N \quad (6.16)$$

where  $\gamma_{fr} = gA_{fr}^2 + \gamma_N$  is the free-running slave damping rate and  $\gamma_N$  is assumed to be independent of optical injection. The explicit relationship between the locked and free-running damping rates is a key feature of the current model and allows us to implicitly include non-linear gain effects as explained below.  $\gamma_{th}$  is the threshold gain shift and appears as a damping component resulting from moving the slave from its free-running condition. It is also related to the phase offset and injection strength such that:

$$\gamma_{th} = 2\eta \cos(\phi_0) = 2 \frac{\eta_0}{R_{FE}} \cos(\phi_0) = -g\Delta N_0 \quad (6.17)$$

Again it is necessary to note that the group velocity is implicit in the differential gain term,  $g$ , everywhere in this derivation. Using (6.16) to substitute for the slave damping rate in (6.15) and re-writing the expression for  $A$ , we have:

$$A = (\gamma_{fr} - \gamma_N)R_{FE}^2 + \gamma_N + \gamma_{th} \quad (6.18)$$

The second and most important term located in the denominator of the response function is  $B$ , which corresponds to the overall resonance frequency of the system. Substituting for the threshold gain shift,  $\gamma_{th}$ , in the  $B$  term defined in (6.10) and rearranging yields:

$$B = \eta^2 + \gamma_{th} (gA_0^2 + \gamma_N) + gA_0^2 (\gamma_P - \gamma_{th}) \quad (6.19)$$

The second term in (6.19), which is related to the steady-state slave locked field and carrier lifetime as  $(gA_0^2 + \gamma_N)$ , effectively appears as a damping rate which can be directly linked to the slave damping rate,  $\gamma_{slave}$ . Using the definition in (6.16) this term can be replaced as following:

$$B = \eta^2 + \gamma_{th}\gamma_{slave} + gA_0^2 (\gamma_P - \gamma_{th}) \quad (6.20)$$

By multiplying both sides of the steady state solution of the locked field found in (6.6) by the differential gain,  $g$ , and rearranging  $\gamma_P$  on the right hand side, yields:

$$gA_0^2 = \frac{gA_{fr}^2\gamma_P - \gamma_N g\Delta N_0}{\gamma_P + g\Delta N_0} \quad (6.21)$$

The first term in the numerator,  $gA_{fr}^2\gamma_P$ , corresponds to the free-running relaxation frequency squared,  $\omega_r^2$ . Substituting the threshold gain shift defined in (6.17) allows (6.21) to be rewritten as:

$$gA_0^2 = \frac{\omega_{fr}^2 + \gamma_{th}\gamma_N}{\gamma_P - \gamma_{th}} \quad (6.22)$$

Substituting (6.14), (6.16) and (6.22) into (6.20) and rearranging will give the following expression for the  $B$  term:

$$B = (\omega_r^2 + \gamma_N\gamma_{th}) + \left(\frac{\eta_0}{R_{FE}}\right)^2 + \gamma_{th} [(\gamma_{fr} - \gamma_N) R_{FE}^2 + \gamma_N] \quad (6.23)$$

For the case of zero injection,  $\eta$  is zero and (6.23) is equal to the relaxation frequency squared of the slave laser,  $B = \omega_r^2$ , which simply represents the slave's free-running operating condition. Similarly, rearranging (6.14), (6.16), (6.17) and (6.22),  $C$  is simplified and expressed as:

$$C = \left(\frac{\eta_0}{R_{FE}}\right)^2 [(\gamma_{fr} - \gamma_N) R_{FE}^2 + \gamma_N] - (\omega_r^2 + \gamma_N\gamma_{th}) Z \quad (6.24)$$

The  $Z$  term corresponds to the correlation between the detuning phase offset and linewidth enhancement factor as defined in (6.12).

$$Z = \frac{\eta_0}{R_{FE}} (\alpha \sin(\phi_0) - \cos(\phi_0)) \quad (6.25)$$

By manipulating (6.8) and applying the parametric terms expressed in (6.18) and (6.23)-(6.25), the relative modulation response function of a stably-locked system can be expressed as:

$$|H_R|^2 = \frac{|H(\omega)|^2}{|H(0)|^2} = \frac{\left(\frac{C}{Z}\right)^2 (\omega^2 + Z^2)}{(C - A\omega^2)^2 + (B\omega - \omega^3)^2} \frac{1}{1 + \left(\frac{\omega}{\gamma_c}\right)^2} \quad (6.26)$$

It is important to note that the response function expressed in (21) has a cubic frequency dependence. Also, depending on the detuning condition, either the  $B$ -containing or  $C/A$ -containing terms in the denominator may have a dominant impact on the overall resonance frequency. The second term in the denominator accounts for the parasitic  $RC$  and carrier transport effects where  $\gamma_c$  is considered as a free-running characteristic constant that can be extracted along with other free-running parameters.

### 6.3.5 Identifying the Known Free-Running Operating Parameters

By taking into the account all the terms in (6.26) one finds that eight fitting parameters including  $\omega_r$ ,  $\gamma_{fr}$ ,  $\gamma_N$ ,  $\gamma_{th}$ ,  $\eta_0$ ,  $R_{FE}$ ,  $Z$  and  $\gamma_c$  are needed for the simulation. All of the terms are expressed as angular frequencies except  $R_{FE}$ , and, compared to previous research, represent a different experimental approach that allows an easy comparison of their relative magnitudes. Since the model is comprised of multiple fitting parameters, there will be many

solutions available that can fit the experimental data. Most of these possible solutions can be eliminated by introducing proper restrictions to the operating parameters during least-squares-fitting, such that they can vary only in an acceptable physical range. However, restrictions are not enough to reach a reasonable level of accuracy of the model unless it is combined with a reduction of the freely varying fitting parameters. Fortunately, some of these parameters can be extracted from the intrinsic free-running parameters which can be determined from the slave laser operating characteristics. The operating parameters of an uncoupled system (free-running slave) can be extracted from the standard and conventional modulation response model:

$$|H_R|^2 = \frac{\omega_r^4}{(\omega_r^2 - \omega^2)^2 + \gamma_{fr}^2 \omega^2} \frac{1}{1 + \left(\frac{\omega}{\gamma_c}\right)^2} \quad (6.27)$$

This expression is used to fit the free-running modulation response and extract three of the fitting parameters: the free-running relaxation oscillation frequency,  $\omega_r$ , the free-running damping rate,  $\gamma_{fr}$ , and the parasitic roll-off induced by  $\gamma_c$ . These parameters are intrinsic characteristics of the slave laser and remain unchanged when the system is injection-locked. The other fitting parameter found in the free-running characteristics is the inverse differential carrier lifetime,  $\gamma_N$ . This term can be directly extracted by plotting the known free-running damping rates as a function of the corresponding relaxation frequencies through the conventional expression  $\gamma_{fr} = K f_r^2 + \gamma_N$ . Knowing the value of  $\gamma_N$  is beneficial since it may have a significant impact on the high frequency behavior of the system under modulation. Consequently, the number of fitting parameters can be reduced from 8 to 4 by keeping the free-running terms constant during the simulation. Further constraints on the remaining fitting parameters have to be found by considering the theoretical limits of semiconductor physics.

## 6.4 Experimental Data and Curve-Fitting Results

### 6.4.1 Experimental Setup and Data

Fig. 6.7 shows a schematic view of the injection-locking setup used in the experiment. The slave laser was a multi-mode QDash FP grown on an n+-InP substrate. The laser under study has a 4- $\mu\text{m}$  wide ridge waveguide and 500- $\mu\text{m}$  cleaved cavity length. The nominal emission wavelength of this FP device is around 1560 nm and the threshold current was measured to be 45 mA at room temperature. The output power of the slave laser was carefully coupled into a single-mode polarization maintaining (PM) lensed fiber using a piezo-electric stage controller with submicron accuracy. The coupling efficiency of the slave laser into the PM lensed fiber was >40%. The PM lensed fiber was connected port 1 of a 3-port PM circulator.

The master laser used in this experiment was a tunable external cavity laser (New Focus 6200) with a single-mode PM fiber pigtail connected to the second arm of the circulator, port 2. A high resolution (0.01 nm) optical spectrum analyzer (Ando AQ6317B) was connected to port 3 of the circulator to measure the detuning between the master and slave lasers, as well as determine stably locked conditions. Port 3 of the circulator was connected to a high-

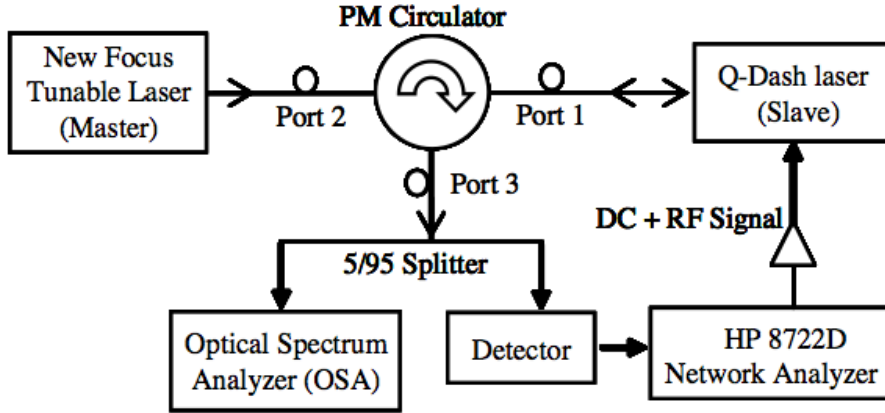


Figure 6.7: Schematic view of the injection-locking QDash experimental setup

speed detector through which the relative modulation response  $S_{21}$  was also measured using an HP 8722D network analyzer. The 5/95 beam splitter at port 3 of the circulator allowed us to measure the modulation response of the injection locked laser while simultaneously monitoring the detuning. This ensured that the desired detuning was stable throughout the experiment. The modulation responses for various frequency detuning scenarios are provided in Fig. 6.8. The injected power provided by the master laser at the slave arm (port 1 of the circulator) and the total slave power at both facets, was measured to be 3.5 dBm and 4.7 dBm, respectively. The side mode suppression ratio (SMSR) for stable locking was taken to be 30 dB; using this criterion, stable locking was observed for detuning frequencies from 13.5 GHz to -17.1 GHz. At the zero frequency detuning condition, a 3-dB modulation bandwidth of 11.7 GHz was observed, which corresponds to a three-fold improvement relative to the free-running case. At the positive frequency detuning edge, the measured modulation response exhibits a large sag as well as a high resonance peak. Due to significant damping, only a slight improvement in the modulation bandwidth is observed for the negative frequency cases.

### 6.4.2 Model Based Analysis

With the validity of the modulation response model verified based on experimental data, it can be used to predict injection-locking behaviors for any FP slave laser once its free running

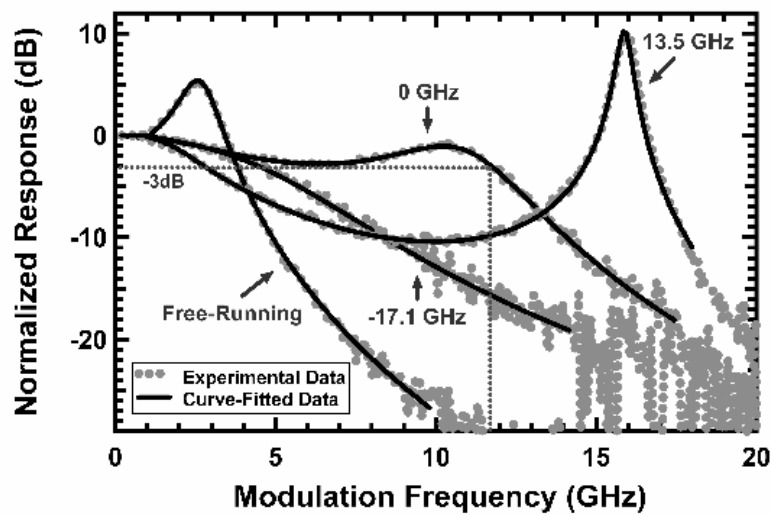


Figure 6.8: Modulation responses of the free-running and the injection-locked laser under zero and extreme frequency detuning conditions

parameters are known. By knowing the operating parameters of the system it is then possible to predict the optimum operating limits of the device such as particular detuning frequencies and the maximum possible bandwidth. One key parameter having a prominent effect on the modulation response is the linewidth enhancement factor. The undesirable sag observed in the

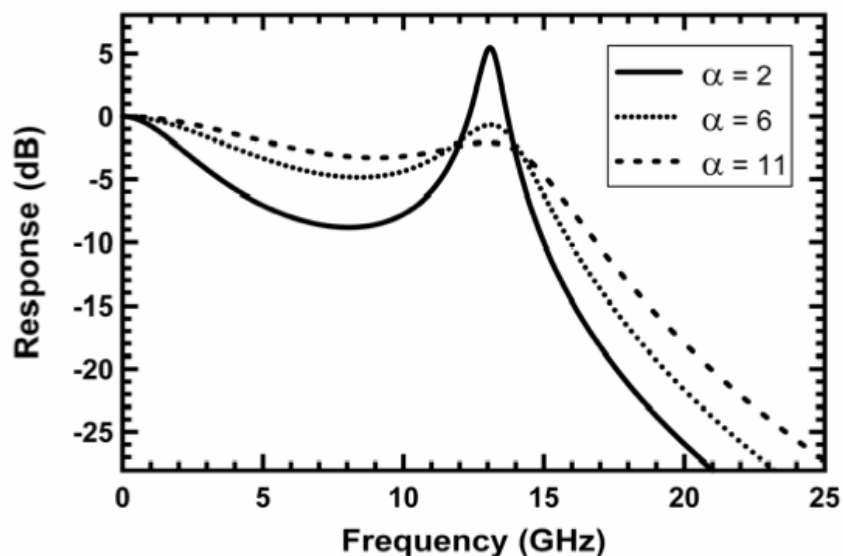


Figure 6.9: Simulation of the modulation response function for various values of the linewidth enhancement factor

modulation response for the extreme positive frequency detuning, as shown experimentally

in Fig. 6.8, can be removed by increasing the linewidth enhancement factor and keeping the same injection ratio. In Fig. 6.9 the change in the modulation response under extreme positive frequency detuning due to a change in the linewidth enhancement factor is illustrated theoretically. At the positive frequency detuning edge, the phase offset is roughly  $\pi/2$  causing the threshold gain shift to approach zero,  $\gamma_{th} \rightarrow 0$ , and the field enhancement becomes unity,  $R_{FE}=1$ . The injection strength and the free-running fitting parameters are kept constant for all three cases.

As shown in Fig. 6.10, the linewidth enhancement factor varies significantly in this device (1.0 to 11) with the bias current. As a consequence of that, the sag in the modulation response should be removable assuming a high enough injection power is available to maintain a constant injection ratio. The significance of this observation is that because the highest relaxation oscillation frequency and hence the highest possible modulation bandwidth occur at the positive frequency detuning edge, removing the sag will achieve the highest possible modulation bandwidth for the injection-locked system. Fig. 6.11 experimentally demonstrates this

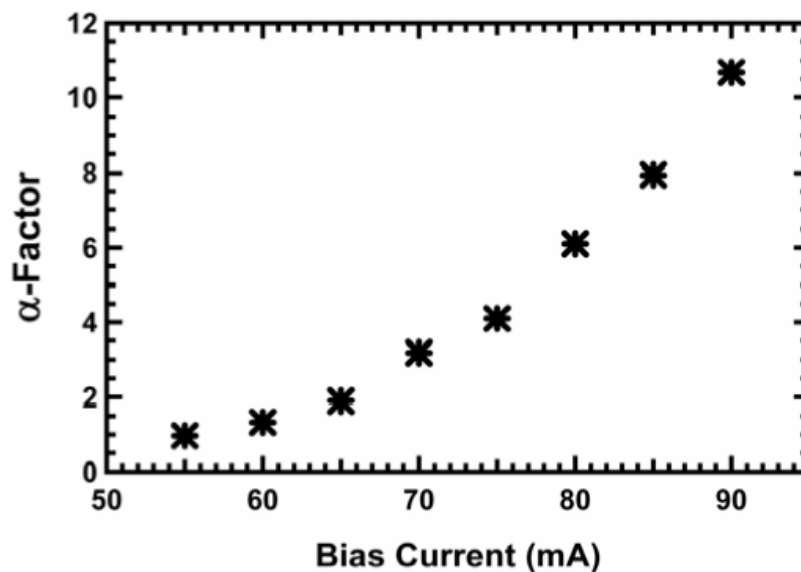


Figure 6.10: Variation of the linewidth enhancement factor as a function of applied bias current in the QDash FP laser

trend, showing modulation response curves at the extreme positive frequency detuning edge for bias currents of 60 mA, 70 mA, and 80 mA and linewidth enhancement factor of 1.3, 3.2, 6.1, respectively, as shown in Fig. 6.10. The sag is shown to be reduced as the bias current, and correspondingly the linewidth enhancement factor, is increased. Based on the theoretical model expressed in (6.26) and depending on how the  $B$ -containing and  $C/A$ -containing terms in the denominator interact, the sag reduces as their resonances detune from each other due

to the change in the linewidth enhancement factor at different bias levels. The maximum injection ratio for the 60 mA, 70 mA, and 80 mA cases was calculated to be 103 GHz, 116 GHz, and 107 GHz, respectively. Note that although the peak frequency decreases as the bias current is increased, the magnitude of the peak remains relatively constant. The decrease in the observed relaxation modulation frequency is likely due to increased device heating as the bias current is increased, along with an increased cavity mode shift which is driven by the linewidth enhancement factor as expressed in (6.5).

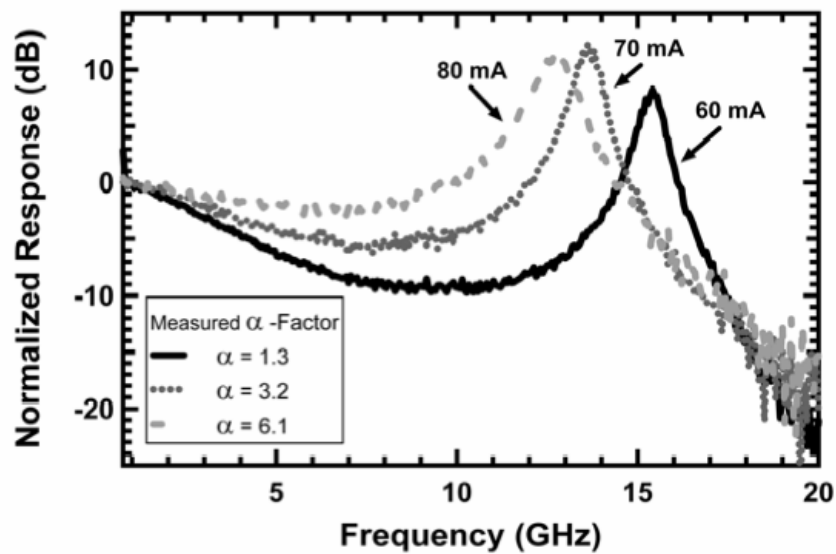


Figure 6.11: Experimental observation of the varied sag as the linewidth enhancement factor is increased